JOURNAL OF GEOPHYSICAL RESEARCH, VOL. 100, NO. D8, PAGES 16,445–16,490, AUGUST 20, 1995

IMAGES: A three-dimensional chemical transport model of the global troposphere

Jean-François Müller

Belgian Institute for Space Aeronomy, Brussels, Belgium

Guy Brasseur

National Center for Atmospheric Research, Boulder, Colorado

Abstract. A new three-dimensional chemical transport model of the troposphere is presented. This model, named intermediate model of global evolution of species, has been developed to study the global distributions, budgets, and trends of 41 chemical compounds, including the most important species that determine the oxidation capacity of the atmosphere. The chemical mechanism is made of approximately 125 chemical reactions and 26 photodissociations. The model accounts for surface emissions, chemical transformations, dry and wet deposition, and aerosol reactions of trace constituents. The model is formulated in σ coordinates and includes 25 layers in the vertical. Its horizontal resolution is 5° in longitude and 5° in latitude. To keep the requirements in computer time limited, a simplified representation of the transport is adopted: the advection, solved by a semi-Lagrangian scheme, is driven by monthly mean climatological winds provided by an European Center for Medium-Range Weather Forecasts analysis. The effect of wind variability at timescales smaller than a month is taken into account by an eddy diffusion parameterization. Convection in cumulonimbus clouds is also represented. All input field, such as the distribution of winds, clouds, eddy diffusion coefficients, and the boundary conditions, are monthly means constrained by observational data. The modeled global distributions of species such as methane, carbon monoxide, nitrogen oxides, and ozone are generally in good agreement with observations. The lifetime of methane, which can be regarded as a measure of the oxidizing capacity of the atmosphere, is found to be equal to 11 years, in agreement with recent estimates. The model also shows that the deposition of ozone at the Earth's surface (1100 Tg/yr) balances the sum of the net photochemical production (550 Tg/yr) and the flux from the stratosphere (550 Tg/yr). In the case of carbon monoxide, surface emissions (1400 Tg/yr) are approximately 50% larger than in situ production by hydrocarbon oxidation (900 Tg/yr).

1. Introduction

Perturbations in the chemical composition of the atmosphere are believed to be potential causes for global changes in the Earth system. The radiative forcing on climate is directly affected by the presence of trace gases such as water vapor, carbon dioxide, methane, nitrous oxide, chlorofluorocarbons, and ozone. The production and fate of these gases result from complex exchange processes at the surface as well as chemical transformations and dynamical transport in the atmosphere. Since the agricultural and industrial revolutions, the surface emission of several chemical constituents has increased substantially, leading to enhanced concentrations of these gases with increased greenhouse forcing and perhaps a significant modification in the oxidizing capacity of the atmosphere. For example, the mixing ratio of carbon dioxide, which was approximately 280 parts per million by volume (ppmv) in year 1800, has currently reached nearly 360 ppmv; in the case of methane it has increased from 700 to 1730 parts per billion by volume (ppbv) over the same period of time.

Paper number 94JD03254.
0148-0227/95/94JD-03254 $05.00

More reactive species such as ozone, carbon monoxide, and nitrogen oxides have also been affected by human activities, especially in urbanized and industrialized areas of Europe, the eastern United States, and the Far East. Biomass burning, resulting from deforestation as well as agricultural practices in the tropics, has been producing additional perturbations in the chemical composition of the troposphere. A major uncertainty in our understanding of tropospheric chemistry is to what extent relatively localized perturbations related, for example, to industrialization affect the global troposphere and hence could be a driving mechanism for global changes.

Numerical models are now commonly used to help quantify chemical and transport processes in the atmosphere. The formulation of these models varies according to the type of problems to be addressed. For example, chemistry-intensive models [e.g., *Madronich and Calvert*, 1989; *Lurmann et al.*, 1986] simulate reactions between several hundreds of chemical constituents at one point of the atmosphere (0-dimensional models). In one-dimensional models, mass exchanges within a single column of air are taken into account by crude parameterizations [*Chameides and Cicerone*, 1978; *Kasting and Singh*, 1986]. At the other extreme, transport-intensive models describe the fate of quasi-conservative tracers in the three-dimensional space but usually ignore or parameterize very simply

the chemical transformations affecting these tracers [*Mahlman and Moxim*, 1978; *Levy et al.*, 1982; *Prather et al.*, 1987; *Fung et al.*, 1991]. Two-dimensional models have been developed as a compromise between these two extreme approaches but are mostly used for stratospheric studies [e.g., *Garcia et al.*, 1992; *Brasseur et al.*, 1990; *Ko et al.*, 1993]. Several attempts, however, have been made to use these models for tropospheric studies [*Logan et al.*, 1981; *Crutzen and Gidel*, 1983; *Isaksen et al.*, 1985; *Isaksen and Hov*, 1987; *Hough*, 1989, 1991; *Law and Pyle*, 1993a, b]. A wide range of studies and sensitivity tests can be carried out using two-dimensional models with reasonable computer requirements. However, these models have important limitations: for example, they tend to overestimate the ozone and hydroxyl radical concentrations [*Lin et al.*, 1988; *Liu et al.*, 1988].

Regional three-dimensional chemical models, developed to study air pollution problems in industrialized regions [e.g., *Liu et al.*, 1984; *Carmichael et al.*, 1986; *Chang et al.*, 1987; *McKeen et al.*, 1991] incorporate detailed photochemical mechanisms as well as accurate representation of transport at high spatial resolution. These models, however, are limited by their spatial extent, the length of the simulation that can be performed (a few days), and the difficulty in specifying boundary conditions at the borders of the domain.

Several attempts with global three-dimensional transport models have been made to study the fate of quasi-inert tracers such as CO_2 [*Fung et al.*, 1983; *Tans et al.*, 1990], nitrous oxide [*Levy et al.*, 1982], halocarbons [*Prather et al.*, 1987; *Zimmerman*, 1988; *Spivakovsky et al.*, 1990], methane [*Taylor et al.*, 1991; *Fung et al.*, 1991], or even relatively short-lived species such as radio-isotopes [*Jacob and Prather*, 1990; *Brost et al.*, 1991; *Feichter et al.*, 1991; *Feichter and Crutzen*, 1990], nitrogen oxides [*Levy and Moxim*, 1989a, b; *Penner et al.*, 1991], sulfur oxides [*Erickson et al.*, 1991; *Langner and Rodhe*, 1991; *Luecken et al.*, 1991], and ozone [*Levy et al.*, 1985]. Very recently, first attempts have been made to incorporate relatively detailed chemical schemes in such tropospheric three-dimensional models [e.g., *Zimmermann*, 1988], while *Spivakovsky et al.* [1990] have provided polynomial approximations (function of tracer concentrations, temperature, and radiation conditions) for the concentration of fast-reacting species (such as OH) in three-dimensional models. The spatial resolution of these global models being limited (typically, 500 km in the horizontal), several important processes cannot be resolved and need to be parameterized in terms of large-scale variables.

In this paper we present a new three-dimensional chemical transport model (CTM) for the global troposphere which can be regarded as intermediate between models in which the transport is driven by the dynamics provided at each time step by a general circulation model, and models in which the transport is highly parameterized, such as in two-dimensional formulations. The motivation for such an approach, also used by *Crutzen and Zimmermann* [1991] in their MOGUNTIA model, is to simulate the three-dimensional behavior and seasonal evolution of a relatively large number of trace constituents, and to estimate their global budgets without prohibitive computer costs. In the present model, named the Intermediate Model of Global Evolution of Species (IMAGES), the advection of trace constituents is simulated on the basis of monthly mean winds provided by the European Center for Medium-Range Weather Forecasts (ECMWF); the effects of dynamical variations on timescales smaller than a month are parameterized by eddy diffusivities determined from the observed wind variability. Thus the model is not expected to reproduce the high-frequency signals observed in the atmosphere but should provide slow-varying concentrations to be compared with climatological averages.

The paper is organized as follows: An extensive description of the model structure is given in section 2; the formulation used for advective, diffusive, and convective transport as well as the adopted chemical scheme and the distribution of surface emissions and deposition velocities are successively presented. The results provided by the model are discussed and compared to available observations in section 3. A summary of the major findings is given in section 4.

2. Model Description

IMAGES is a global three-dimensional chemical transport model which extends from the surface to the lower stratosphere (pressure level of 50 mbar or approximately 20 km altitude). The model provides the distribution of 41 species, including ozone (O_3), hydrogen compounds (OH, HO_2, H_2O_2), nitrogen compounds (NO, NO_2, HNO_3), CO, several hydrocarbons (CH_4, C_2H_6, C_3H_6, isoprene) and oxygenated organic species. A list of the species considered in the model is given in Table 1. Although transport is not considered in the calculation of the most reactive species such as $O(^1D)$, OH, or HO_2, the behavior of trace constituents is generally represented by the continuity/transport equation

$$\frac{\partial \mu}{\partial t}=\left(\frac{\partial \mu}{\partial t}\right)_{\text{advection}}+\left(\frac{\partial \mu}{\partial t}\right)_{\text{diffusion}}+\left(\frac{\partial \mu}{\partial t}\right)_{\text{convection}}+\left(\frac{\partial \mu}{\partial t}\right)_{\text{chemistry}} \quad (1)$$

where μ represents the volume mixing ratio and t is time. The right-hand side of this equation includes (1) the contribution of transport by the large-scale circulation (expressed by the wind field $\mathbf{v}$), (2) the contribution of unresolved motions represented by a diffusion term, (3) the contribution of deep convection in cloud systems, and (4) the tendency due to chemistry. The continuity equations of the chemical species are solved numerically on a $5° \times 5°$ grid. The equations are discretized with height on 25 σ levels (see Table 2). Here σ is defined [*Phillips*, 1957] as

$$\sigma=\frac{p-p_t}{p_s-p_t} \quad (2)$$

where p is pressure, p_s is the pressure at the surface, and p_t = 50 mbar. Thus the model accounts implicitly for the surface orography in the limits of its horizontal resolution. Note from Table 2 that the levels are not equally spaced. To accurately represent vertical exchanges of chemical species within the boundary layer, the vertical resolution is highest near the surface. Only two-three levels are located in the stratosphere. The formulation of boundary layer exchanges is kept simple and does not represent the diurnal variation of its height and eddy diffusivities. Equation (1) is solved numerically by a time-splitting technique. Advection is addressed separately from the other components. Although vertical diffusion, deep convection, and the chemistry terms are treated in a single step in the model, their resolution will be presented separately for clarity. The time step used for all processes is 1 day, except during the first 3 days of each month, during which a full diurnal calculation is performed with a time step of 1 hour (half an hour during day 3).

Table 1. Chemical Species Included in the Model

Chemical Formula	Name
Fixed species	
O_2: 20.95%	
N_2: 79.05%	
H_2O: climatological distribution from ECMWF	
H_2: 550 ppbv	
N_2O: 305 ppbv	
Inorganic Species	
Long-lived species (transport considered)	
O_3	ozone
H_2O_2	hydrogen peroxide
HNO_3	nitric acid
$NO_x \int NO + NO_2 + HNO_4 + NO_3 + 2N_2O_5$	nitrogen oxides (family)
Organic Species (NonOxygenated)	
CH_4	methane
C_2H_6	ethane
C_2H_4	ethylene
C_3H_6	propylene
C_5H_8	isoprene
$C_{10}H_{16}$	α-pinene
OTHC	other hydrocarbons
Organic Species (Oxygenated)	
CO	carbon monoxide
CH_2O	formaldehyde
PAN ($CH_3CO_3NO_2$)	peroxy-acetyl nitrate
MPAN ($CH_2CCH_3CO_3NO_2$)	peroxymethacrylic nitrate
CH_3OOH	methyl peroxide
C_2H_5OOH	ethyl peroxide
C_3H_6OHOOH	peroxide from propylene
CH_3COOOH	peracetic acid
Inorganic Species	
Short-lived species (transport not considered)	
$O(^1D)$	oxygen atom (excited state)
O or $O(^3P)$	oxygen atom (fundamental state)
OH	hydroxyl radical
HO_2	hydroperoxyl radical
NO	nitrogen monoxide
NO_2	nitrogen dioxide
HNO_4	pernitric acid
NO_3	nitrogen trioxide
N_2O_5	nitrogen hemipentoxide
Carbonyls	
CH_3CHO	acetaldehyde
CH_2OHCHO	glycolaldehyde
CHOCHO	glyoxal
CH_3COCHO	methylglyoxal
MVK ($CH_2CHCOCH_3$)	methylvinylketone
MACR (CH_2CCH_3CHO)	methylacrolein
Peroxy Radicals	
CH_3O_2	methylperoxy radical
$C_2H_5O_2$	ethylperoxy radical
$C_3H_6OHO_2$	peroxy radical from propylene
$C_5H_8OHO_2$	peroxy radical from isoprene
$MOHO_2$	peroxy radical from MVK and MACR
CH_3CO_3	acetylperoxy radical
MCO_3 ($CH_2CCH_3CO_3$)	peroxymethacrylic radical

ECMWF, European Centre for Medium Range Weather Forecasts; MVK, methylvinylketone; MACR, methylacrolein .

Table 2. Sigma Levels of the Model

	σ	*p*, mbars	*z*, km
1	0.995	995	0.04
2	0.99	991	0.07
3	0.98	981	0.14
4	0.97	972	0.22
5	0.95	953	0.35
6	0.93	934	0.52
7	0.90	905	0.75
8	0.85	858	1.15
9	0.80	810	1.6
10	0.75	763	2.0
11	0.70	715	2.5
12	0.65	668	3.0
13	0.60	620	3.6
14	0.55	573	4.2
15	0.50	525	4.8
16	0.45	478	5.5
17	0.40	430	6.9
18	0.35	383	7.2
19	0.30	335	8.2
20	0.25	288	9.4
21	0.20	240	10.7
22	0.15	193	12.4
23	0.10	145	14.5
24	0.05	98	17.5
25	0.00	50	22.5

Value of p is pressure and z is approximate altitude of the levels; σ is defined in text.

2.1. Transport

Transport is explicitly taken into account for species whose lifetime is larger than a few hours (see Table 1). To be able to use a relatively large time step in the model, the transport scheme required to solve equation (1) is developed as follows: The wind components used for advection calculation are monthly mean climatological values derived from objective analyses by ECMWF of the observed winds. The effect of temporal wind variability (on time-scales shorter than 1 month) is therefore not taken into account in the advection term of the transport equation. However, large-scale mixing associated with wind variability is represented by the diffusion term in equation (1). The additional transport components (subgrid processes) which are included in the model are turbulent mixing in the planetary boundary layer (contributing to the diffusion term) and vertical transport associated with convective cloud formation (convection term).

2.1.1 Advection. The choice of the numerical technique to solve the advection equation,

$$\frac{\partial \mu}{\partial t} = -\mathbf{v}\cdot\nabla\mu \tag{3}$$

(where **v** is the wind vector) is constrained by the need to circumvent stability criterions such as the Courant-Friedrich-Lewy (CFL) condition. The CFL condition applied to the IMAGES model would require a time step of less than 1 hour. Furthermore, advection schemes producing artificial oscillations of the advected field (undershoots and overshoots) are inappropriate, as these oscillations may lead to negative mixing ratios of the chemical species. A semi-Lagrangian scheme is used in the model, allowing for the use of large time steps. It is based on an original approach by *Smolarkiewicz and Rasch* [1991] (see also *Smolarkiewicz and Grell* [1991]). The method makes use of the theoretical equivalence between the semi-Lagrangian interpolation and the advection problem [e.g., *Ritchie*, 1986; *Smolarkiewicz and Rasch*, 1991]. The latter may be solved using any Eulerian scheme, since the analog of the CFL condition for this problem is proved to be always satisfied. The interpolation scheme derived from an advection scheme following this procedure has the same order of accuracy and other properties (e.g., monotonicity conservation) as the advection scheme. The operational version of our interpolation scheme uses the second-order version of the Eulerian advection algorithm developed by *Tremback et al.* [1987], to which an flux-corrected-transport (FCT) correction is applied to ensure monotonicity preservation [*Zalesak*, 1979; *Smolarkiewicz and Grell*, 1992]. The semi-Lagrangian scheme is thus second-order accurate in space and time and preserves the monotonicity of the solution; that is, no artificial extremum of the solution is produced. The calculation of the air parcel trajectories (i.e., the departure points) requires that the wind components be interpolated at the midpoint between the departure and the arrival points. As the winds and therefore the departure points are constant during each month, trajectory calculations are performed only once per month of simulation. The method is based on *Smolarkiewicz and Grell* [1992], with some differences. The model time step Δt (1 day) is subdivided into N time intervals ($\Delta t/N$). Defining x_0 (at time t_0) and x_i (at time $t = t_0 + \Delta t$) as the departure and arrival points, respectively, and

$$t_k = t_0 + \frac{k\Delta t}{N} \qquad k = 1, \ldots, N \tag{4}$$

the departure point (x_0) is obtained by successively calculating the positions x_k ($k = N - 1, \ldots, 0$) of the air parcel at time t_k with

$$x_{k+1} - x_k = v\left(\left(x_{k+1} + x_k\right)/2, \left(t_{k+1} + t_k\right)/2\right)\frac{\Delta t}{N} \tag{5}$$

Here the wind at midpoint $(x_{k+1} + x_k)/2$ is computed iteratively and interpolated from the grid values using the sixth-order version of the Tremback et al. scheme, again with FCT correction. Four iterations are performed, although only two iterations would be necessary to achieve second-order accuracy. N is set to a value as large as 48, so that the convergence criterion for trajectory calculation using equation (5) [see *Smolarkiewicz and Grell*, 1991],

$$\left|\frac{\partial v}{\partial x}\right|\frac{\Delta t}{N} \le 1 \tag{6}$$

is always satisfied. Departure points which are found to lie outside the model domain (in the vertical) are moved to the nearest model level.

This semi-Lagrangian scheme was tested in a way similar to the procedure described by *Smolarkiewicz and Rasch* [1991]. The initial condition for the test is a cone of unit height and radius equal to $5\Delta x$ or 25°, centered at the equator and 90°E. The background value of the tracer is equal to zero. The wind field is a horizontal nondivergent stationary flow, parameterized by equation (A3) of *Smolarkiewicz and Rasch*, with the U value chosen so that one revolution around the Earth requires 180 time steps, and $\beta = 0.5$, so that the axis of rotation makes an angle of 45° with the equatorial plane. The trajectories are computed using the sixth-order, monotonic version of the Tremback et al.

scheme. The test was repeated to compare six different versions of this numerical scheme. The results are very similar to those obtained by *Smolarkiewicz and Rasch* [1991]. Computer time per revolution on the National Center for Atmospheric Research (NCAR) Cray-YMP computer varies from 0.089 s (order 2, no FCT correction) to 2.695 s (order 6, FCT correction). The error on the global tracer mass decreases with the order of accuracy (−0.13% and −0.02% per revolution with order 2 and order 4, respectively, without FCT) and increases when the FCT correction is applied (6.89% with order 2). Figures 1a–1d show the solution after one revolution around the Earth, using different versions of the Tremback et al. scheme. As can be seen from the figures, non-FCT versions of the scheme are less diffusive than their monotonic counterparts but create artificial oscillations and negative concentrations of the advected field.

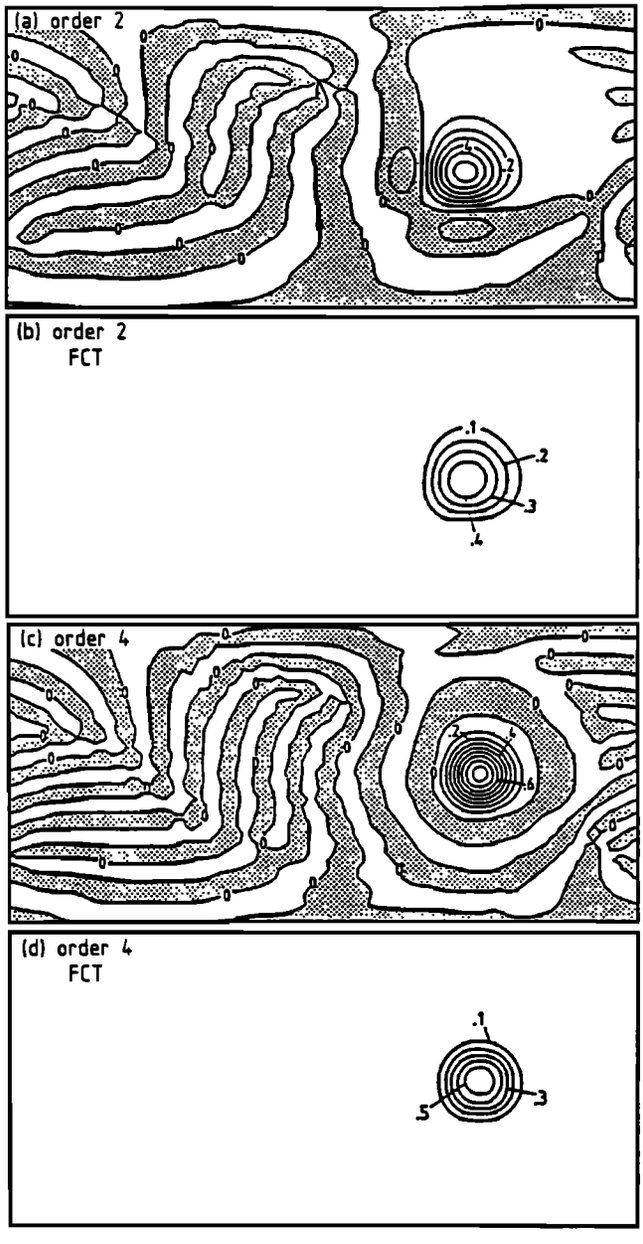

Figure 1. Solution of a cone test after one revolution around the globe, using four different versions of the semi-Lagrangian scheme: (a) second order, nonmonotonic, (b) second order, monotonic, (3) fourth order, nonmonotonic, and (d) fourth order, monotonic.

The winds used in the IMAGES model as well as the surface pressure, the temperature, and humidity fields are climatological (1985–1989) averages derived from a global analysis of ECMWF fields [*Trenberth and Olson*, 1988a, b; K. Trenberth, personal communication, 1992]. The data provided by the analysis are distributed on a T42 grid and 14 pressure levels (in millibar: 1000, 850, 700, 500, 400, 300, 250, 200, 150, 100, 70, 50, 30, 10). The monthly mean ECMWF data were first averaged over the 1985–1989 period and were then interpolated on the σ levels and horizontal grid of the model. The vertical velocity in σ coordinates is computed using

$$\dot{\sigma}=-\sigma\frac{\partial \ln p_{st}}{\partial t}-\sigma\frac{\partial \ln p_{st}}{\partial x}u-\sigma\frac{\partial \ln p_{st}}{\partial y}v+\frac{g\omega}{p_{st}} \tag{7}$$

where $p_{st} \equiv p_s - p_t$, g is gravitational acceleration, $\varpi = dp/dt$, and u and v are the usual horizontal wind components [see *Müller*, 1993] for further details about the formulation of transport equations in σ coordinates).

2.1.2. Diffusion. The three-dimensional diffusion equation of a tracer in σ coordinates is written as

$$\frac{\partial \mu}{\partial t}=\frac{1}{p_{st}}\frac{\partial}{\partial x}\left(p_{st}K^{xx}\frac{\partial \mu}{\partial x}\right)$$
$$+\frac{1}{p_{st}\cos\phi}\frac{\partial}{\partial y}\left(p_{st}\cos\phi K^{yy}\frac{\partial \mu}{\partial y}\right)+\frac{\partial}{\partial \sigma}\left(K^{\sigma}\frac{\partial \mu}{\partial \sigma}\right) \tag{8}$$

where ϕ is latitude,

$$K^{\sigma}\equiv\left(\frac{\rho g}{p_{st}}\right)^2 K^{zz}, \tag{9}$$

and K^{xx}, K^{yy}, K^{zz} are the diffusion coefficients in the zonal, meridional, and vertical direction, respectively. In this equation, the nondiagonal components of the diffusion tensor (e.g., K^{xy}) are neglected. This equation is solved by an alternate direction technique and an implicit Eulerian scheme in each direction. This scheme is mass conservative, second-order accurate in space but first order in time (see *Müller* [1993] for further details about the scheme). The boundary conditions at the surface are specified either with a fixed mixing ratio (μ_s) or by a flux and/or a deposition velocity at the surface. In the latter case, μ_s is related to the mixing ratio at the first level (μ_1) by equating the fluxes between the surface and the first level:

$$\frac{p_{st}}{g}K^{\sigma}_{1/2}\frac{\mu_1-\mu_s}{\sigma_1-1}=-\rho_s v_d \mu_s+\frac{m_{air}}{N_{AV}}\Phi_S \tag{10}$$

where Φ_S is the emission flux (molecule/cm^2/s), v_d is the deposition velocity (cm/s), ρ_s is the air density at the surface, m_{air} is the average molecular mass of the air, and N_{AV} is the Avogadro number. $K^{\sigma}_{1/2}$ is computed using equation (9) at the midpoint between the surface and the first level. The boundary conditions at the top of the model are set using a relationship similar to equation (10), without the deposition velocity.

The diffusion introduced in the model represents the mixing of

tracers resulting from the variability of the winds. Following *Murgatroyd* [1969], the diffusion coefficients in the horizontal (K^{xx} and K^{yy}) are assumed proportional to the deviations of the monthly mean winds, which are taken from the ECMWF winds analysis:

$$K^{xx} = \langle u'^2 \rangle T_u \tag{11}$$

$$K^{yy} = \langle v'^2 \rangle T_v \tag{12}$$

u' denotes here the deviation of u from its monthly average and $\langle u'^2 \rangle$ is the monthly average of u'^2. The timescales T_u and T_v were estimated by *Murgatroyd* [1969] from Lagrangian trajectory analyses; their large variability may be partly represented with a simple dependence on altitude (Figure 5 of *Murgatroyd* [1969]). The vertical diffusion coefficient (K^{zz}) is also calculated from the ECMWF analysis, using

$$K^{zz} = -(\rho g)^2 \frac{\langle \omega' \theta' \rangle}{\partial \theta / \partial p} \tag{13}$$

where θ is the potential temperature and ω is the pressure velocity. The derivation of the diffusion coefficients is thus consistent with the winds provided by the ECMWF. Typical values of K^{xx} are 10^6–10^7 m^2/s at midlatitudes, with much smaller values in the tropics. K^{yy} is generally a factor of 2 lower than K^{xx}. The largest values of K^{zz} (>10 m^2/s) are also found in the middle troposphere at midlatitudes.

Rapid turbulent exchanges of air may take place in the planetary boundary layer (PBL), resulting occasionally in strong vertical mixing of the chemical constituents. These subgrid-scale processes are extremely variable in space and time and are therefore difficult to represent accurately. A thin, stable surface layer is generally noted just above the surface. A mixed layer of variable height (up to 1–2 km), where turbulent mixing is generally 2 or 3 orders of magnitude larger, extends above the surface layer. Depending on meteorological conditions, the PBL may be stable (e.g., during a temperature inversion), neutral, or unstable [*Pasquill*, 1974]. A simple dependence of the K^{zz} coefficients on the vertical gradient (γ) of potential temperature is assumed in the model:

$$K^{zz} = K_5 \left(\frac{K_{15}}{K_5} \right)^{\frac{\gamma - 5}{10}} \quad \text{if } 5 \le \gamma \le 10$$

$$K^{zz} = K_{-5} \left(\frac{K_5}{K_{-5}} \right)^{\frac{\gamma + 5}{10}} \quad \text{if } \gamma < 5 \tag{14}$$

where γ is expressed in Kelvin per kilometer. The values of parameters K_{-5}, K_5, and K_{15} vary with σ in the PBL, as shown in Table 3. These altitude profiles are based on the study of *Pasquill* [1974] and the vertical profiles of K^{zz} above the ocean given by *Bonsang et al.* [1991]. Monthly mean temperature data are used to compute the coefficients. The calculated γ values are never negative, so that on the average the boundary layer is never unstable. The values of K^{zz} are, however, sufficiently high to allow for rapid exchanges of mass between the surface and the free troposphere. The K^{zz} values are found to be highest (up to 20 m^2/s) above subtropical deserts in summer. The PBL is very stable over ice and snow-covered regions.

2.1.3. Deep convection. Several modeling studies [e.g., *Chatfield and Crutzen*, 1984; *Gidel*, 1983; *Feichter and Crutzen*, 1990; *Jacob and Prather*, 1990] have emphasized the importance of deep convection, in particular for tropospheric trace gases whose lifetime is of the order of hours to months. The scheme used in IMAGES is similar to the probabilistic parameterization of *Costen et al.* [1988], itself based on the study by *Chatfield and Crutzen* [1984]. Although convection is fundamentally complex and three dimensional, it is approached as a one-dimensional process, described by the equation

$$\frac{\partial \mu}{\partial t} = \int \tilde{\Pi}(\sigma, \sigma') \mu(\sigma') d\sigma' \tag{15}$$

where the $\tilde{\Pi}(\sigma, \sigma')$ are constrained by

$$\int \tilde{\Pi}(\sigma, \sigma') d\sigma = 0 \tag{16}$$

$$\int \tilde{\Pi}(\sigma, \sigma') d\sigma' = 0 \tag{17}$$

The $\tilde{\Pi}(\sigma, \sigma')$ are related to the z-coordinates $\Pi(z,z')$ of Costen et al. by

$$\tilde{\Pi}(\sigma, \sigma') = \left[\Pi(z(\sigma')) - \frac{1}{\tau} \delta(z(\sigma) - z(\sigma')) \right] \frac{p_{st}}{\rho(z(\sigma)) g} \tag{18}$$

where τ is chosen to be equal to 1 s, and δ denotes the Dirac distribution. The integrals are taken over the whole vertical domain, from model top to the surface. Note that a homogeneous μ is not affected by the convection scheme (see equation (16)) and that the vertically integrated mass is unchanged by convection (see equation (17)). Following Costen et al., we assume that ascending motions transport air from the boundary layer (the five bottom layers in the IMAGES model) to the free troposphere (sixth level and above), while subsidence transports

Table 3. Vertical Diffusion Coefficients (m^2/s) in the Planetary Boundary Layer, for Different Stability Conditions (γ = 15, 5, -5 K/km)

		Stable,	Neutral		Unstable	
σ	z, m	K_{15}	Continental	Ocean	Continental	Ocean
0.995	35	0.2	2.5	1	8	4
0.99	70	0.25	5	3	17	15
0.98	150	0.2	7	8	55	30
0.97	220	0.1	8	7	80	60
0.95	370	0.05	8	3	95	90
0.93	520	0.01	7	2	100	40
0.90	750	0.01	4	1.5	90	20
0.85	1150	0.01	3	1	60	10
0.80	1580	0.01	2	0.5	30	5

air from each level to the adjacent lower level only. With these assumptions, all Π values can be derived from the updraft densities

$$a_j \equiv \bar{\Pi}_{j,j'} \quad j' \leq 5, j > 5 \tag{19}$$

using relationships similar to those derived by Costen et al. The updraft densities are parameterized by

$$a_j = C_{Cb} \times p_j \tag{20}$$

where j is the altitude index and C_{Cb} is the cumulonimbus fraction in the 5° × 5° IMAGES cell. The latitude dependence of the parameters p_j (Figure 2) accounts for the variation in the cloud top altitude which is highest in tropical regions [e.g., *Feichter and Crutzen*, 1990]. The distribution of the cumulonimbus fractional cover is taken from the International Satellite Cloud Climatology Project (ISCCP) [*Rossow et al.*, 1987; *Rossow and Schiffer*, 1991]. Monthly mean data are used, averaged over the period 1984–1987. The ISCCP data are described in full detail and compared with other cloud climatologies (e.g., the cloud atlases of *Warren et al.* [1986, 1987]) in the work of *Pham* [1993]. The calculation of p_j is based on the tropical values by *Costen et al.* [1988] and adjusted on the basis of observed distributions of radon 222 concentrations (see below). As mentioned above, tracer convection and diffusion are solved in the same step, and stability is ensured through an implicit method. The matrix involved is tridiagonal with in addition nonzero elements in the first five columns.

2.1.4. Validation of the transport scheme. Radon 222 is an ideal tracer to validate vertical transport parameterizations. Its lifetime is short and well established (radioactive of half-life 3.824 days) and a large number of observations of its atmospheric concentrations are available [e.g., *Brost and Chatfield*, 1989; *Feichter and Crutzen*, 1990; *Jacob and Prather*, 1990]. Radon 222 is emitted by soils, at a rate which is assumed to be constant and equal to 1 molecule/cm^2/s. Snow cover is assumed to reduce by 50%. Ice and water emit only negligible amounts of radon. Typical concentrations are between 50 and 250 pCi/m^3 STP in the continental boundary layer (1 picocurie per standard cubic meter, or pCi/m^3 STP, corresponds to a volume mixing ratio of 6.6×10^{-22}). *Liu et al.* [1984] presented altitude profiles of radon at about 10 continental midlatitudes sites. Only the average profile for summer is statistically significant, due to the variability in the observed values and the small number of profiles for the other seasons. The average concentration of radon 222 observed in summer in the continental northern midlatitudes is shown in Figure 3. The summer profile (June to August) calculated by the model for the continental midlatitudes (35°–55°N) is also presented. In both cases the concentrations of radon decreases by 2 orders of magnitude between the surface and 12 km. Note that the gradient would have been much steeper, had deep convection been omitted from the transport scheme. The model values displayed in Figure 3 fall generally within the error bars for the measurements.

Mixing of long-lived tracers between the two hemispheres is a much slower process than transport along the zonal and vertical directions. Long-lived tracers such as the chlorofluorocarbons and the krypton 85 radioisotope are appropriate to validate or possibly to adjust the representation of meridional transport in atmospheric models. Krypton 85 has a half-life of 10.76 years and is produced exclusively by pressurized water reactors (PWRs), a class of nuclear reactors, in the northern hemisphere. It is therefore well suited to test interhemispheric transport in atmospheric models [e.g., *Weiss et al.*, 1983; *Jacob et al.*, 1987; *Zimmermann et al.*, 1989]. *Jacob et al.* [1987] estimated the annual emissions of krypton 85 between 1978 and 1983. The largest uncertainty is the exact location of the former Soviet sources; we assumed that these are concentrated in Kyshtym (55°N, 60°E). The interhemispheric transfer time can be defined as

$$\tau_{tr} = \frac{B_N - B_S}{\Phi_{eq}} \tag{21}$$

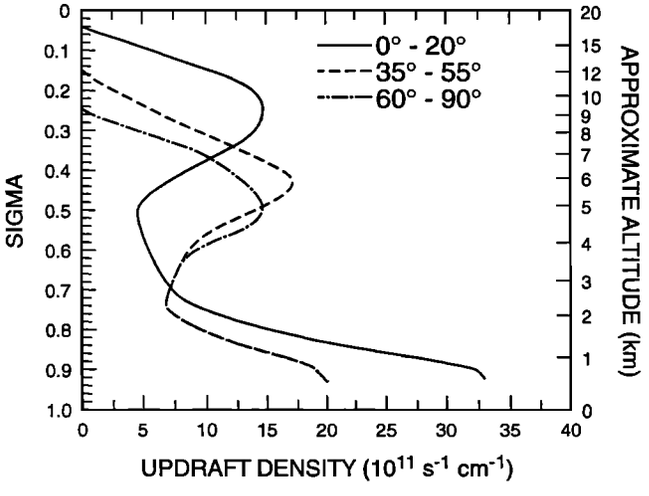

Figure 2. Updraft densities (p_j) used in the model to represent deep convection, in tropical, temperate, and boreal regions (10^{11} s^{-1} cm^{-1}). The p_j values at other latitudes are calculated by linear interpolation.

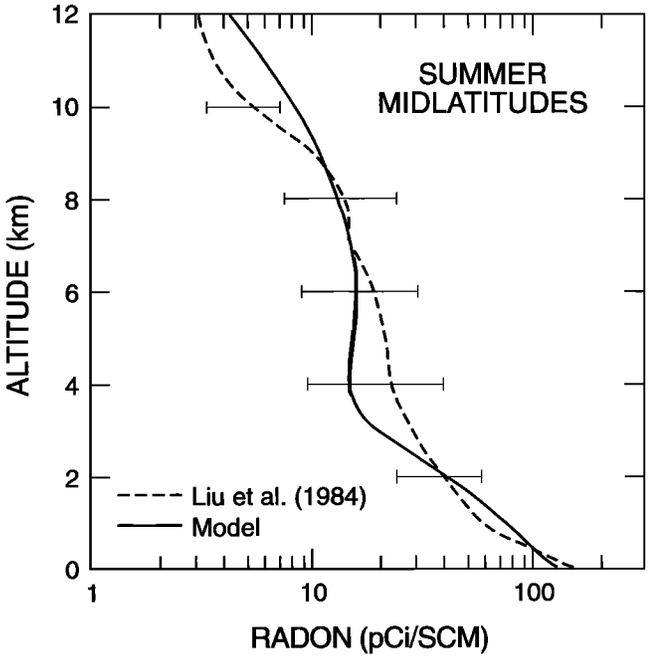

Figure 3. Observed and calculated concentration profile of radon 222 (in picocurie per standard cubic meter) during summer (June–August) at continental northern midlatitudes.

where B_N and B_S are the integrated amounts of krypton in the northern and southern hemisphere, respectively, and Φ_{eq} is the flux through the equator. As the emission flux is entirely situated in the northern hemisphere, Φ_{eq} is given by the relationship expressing the overall balance in the southern hemisphere

$$\Phi_{eq} = \frac{dB_S}{dt} + \frac{B_S}{\tau_d} \tag{22}$$

where τ_d is the exponential lifetime of krypton 85 (15.52 years). The transport of krypton 85 simulated in the model over the 1978–1983 period was tested using the initial conditions and annual emissions adopted earlier by *Jacob et al.* [1987]. Note that the dynamical fields used in IMAGES (the 1985–1989 average from ECMWF) cannot account for year-to-year variability of the winds. When the meridional diffusion coefficients (K^{yy}) are reduced uniformly by a factor of 1.5, the interhemispheric transfer time (calculated using equations (20) and (21)) is found to be 1.1 year, in agreement with Jacob et al. This uniform reduction of the K^{yy} values (which is justified in view of the crudeness of the diffusion parameterization) has been applied to all subsequent calculations presented in this paper. The latitude profiles of krypton concentration at the surface measured by W. Weiss over the Atlantic (reported by *Jacob et al.* [1987]) are displayed in Figure 4 and compared with model results at 30°W (middle of the Atlantic). The nearly constant concentration in the southern hemisphere is well reproduced by the model. Note the steep gradient in the Intertropical Convergence Zone (ITCZ), although the latitude of the concentration jump is shifted equatorward in October 1980 and

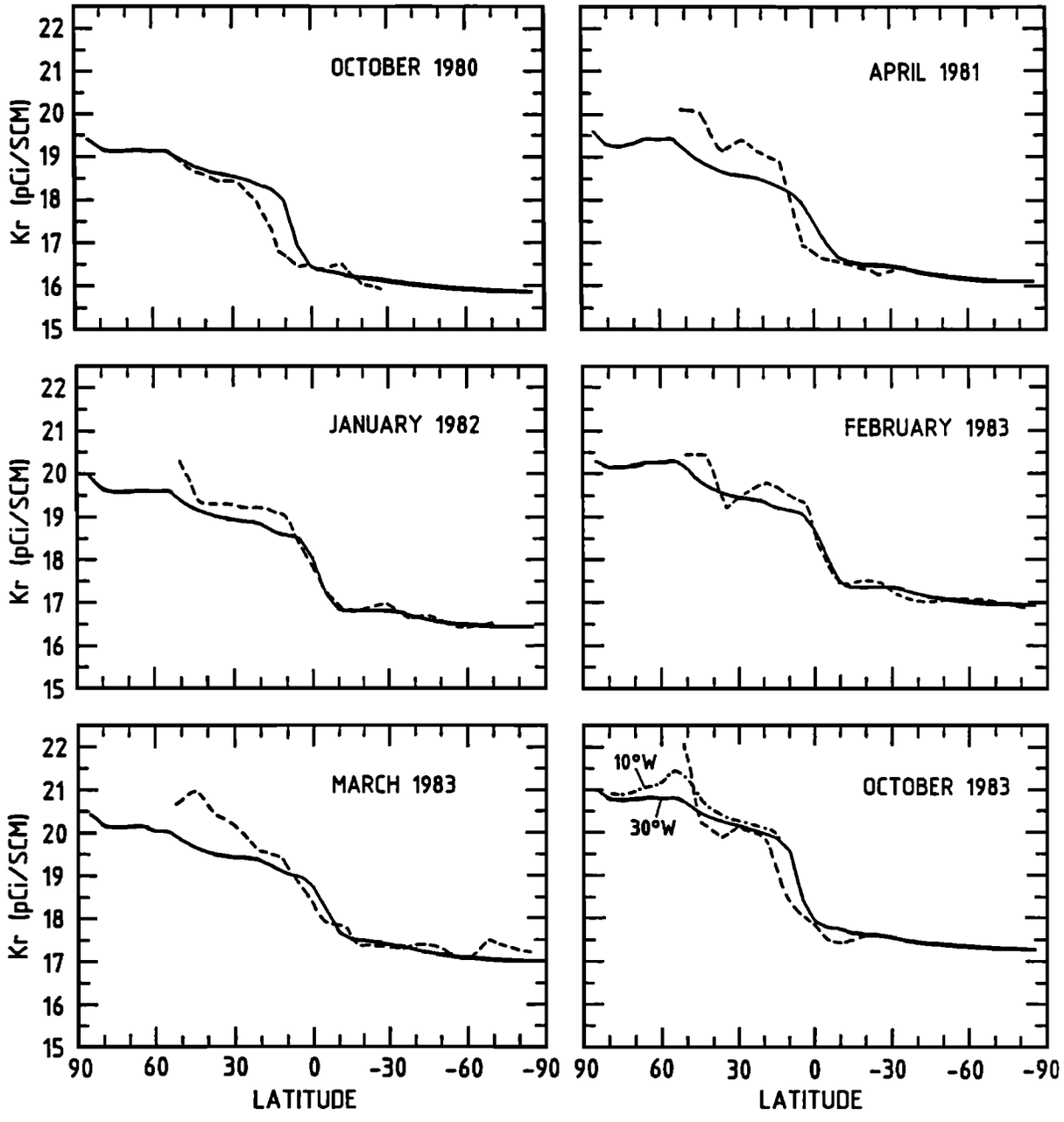

Figure 4. Observed (dashedcurve) and calculated (solidcurve) concentration of krypton 85 (in picocurie per standard cubic meter) at the surface of the Atlantic. Model curve is at 30°W, except when indicated.

1983. The amplitude of this "discontinuity" is correctly predicted, except in April 1981. North of the ITCZ, the concentration increases slowly with latitude, with a gradient predicted by the model which is too weak in March and October 1983.

2.2. Chemistry

2.2.1. Numerical resolution. The continuity equation of a trace gas affected by chemistry is

$$\frac{\partial \mu}{\partial t} = P - \beta\mu \tag{23}$$

where P and β are the photochemical production and first-order loss rate, respectively. As mentioned earlier, the concentrations of short-lived species are calculated without considering the effect of transport. Among these species, the shortest-lived species (e.g., O, $O(^1D)$, OH, HO_2...) are calculated assuming photochemical equilibrium conditions, i.e.,

$$\mu = \frac{P}{\beta} \tag{24}$$

For the other nontransported species the semianalytic method proposed by *Hesstvedt et al.* [1978] (also called quasi-steady-state-approximation (QSSA)) is used:

$$\mu^{t+\Delta t} = \frac{P}{\beta} + \left(\mu^t - \frac{P}{\beta}\right) e^{-\beta\Delta t} \tag{25}$$

This expression provides the exact solution of equation (23) when P and β are constant during time step Δt. When the lifetime is much larger than the time step, the QSSA approximation is replaced by the forward Euler (explicit) formula

$$\mu^{t+\Delta t} = \mu^t + \left(P - \beta\mu^t\right)\Delta t \tag{26}$$

in order to avoid numerical problems using equation (25) when β is close to zero.

In the general case, P and β depend on the concentration of the other chemical species. An iterative procedure is therefore required. Intermediate solutions $\mu^{(k)}$ (k = 1, ..., N) for all species are calculated successively, the time step Δt in equations (25) and (26) being replaced by $\Delta t/N$. Note that the iterations are carried out not only within each family but also across the families. Sensitivity tests performed using a box model show that the best results are found when the iteration number (N) is taken to 4. Once the concentrations of the short-lived have been computed, the photochemical production and loss terms for the transported species or families are calculated. Chemistry for these long-lived species is solved during the same step as vertical diffusion and deep convection, using an implicit scheme.

2.2.2. Chemical mechanism. The model chemistry includes 41 species and 125 reactions, including 26 photolytic reactions. The monthly mean distributions of water vapor mixing ratio are specified from the ECMWF analyses. The chemical mechanism and rate constants are given in Table 4, based mainly on the recommendations of *De More et al.* [1992] and *Atkinson et al.* [1989] for inorganic chemistry and on the NCAR master mechanism [see e.g., *Calvert and Madronich*, 1987; *Madronich and Calvert*, 1989, 1990] for organic chemistry. The master mechanism is fully explicit and includes hundreds of chemical species and thousands of reactions. Such an explicit mechanism, however, is too complex to be included in a three-dimensional model. Only a small number of nonmethane hydrocarbons are therefore taken into account in the model. These are ethane, ethylene, propylene, isoprene, terpenes, and a lumped species, OTHC, used as a surrogate for all other hydrocarbons. OTHC has the same carbon number and OH-reaction rate as *n*-butane. Given the major role played by isoprene, due to its large surface emissions, its oxidation chemistry is treated in some detail. Box model calculations showed that the isoprene scheme presented here produce results which are in reasonable agreement with results obtained using the recent, more detailed mechanism of *Paulson et al.* [1992]. The following assumptions were made to simplify the hydrocarbon oxidation mechanism:

1. A lumping technique is introduced to reduce the number of species [e.g., *Gery et al.*, 1989; *Stockwell*, 1986]. For example, the peroxy radicals formed by the isoprene reaction with OH are lumped into one species, noted $C_5H_8OHO_2$. The acetyl radical CH_2OHCO_3 formed by glycolaldehyde reaction with OH is treated as the acetyl-peroxy radical CH_3CO_3.
2. Formic and acetic acid, glyoxal and methylglyoxal, and the organic alcohols produced in the mechanism are assumed to be removed from the atmosphere by nongas phase processes, i.e., wet and dry deposition, and reaction on aerosols [e.g., *Chameides*, 1984; *Jacob*, 1986; *Jacob and Wofsy*, 1988, 1990].
3. The gas phase destruction of alkyl nitrates ($RONO_2$), produced by reactions of peroxy radicals with NO, is neglected when their reaction rate with OH is smaller than 10^{-12} cm^3/molecule s^{-1} (the photochemical lifetime is then larger than about 2 weeks). In this case, deposition and aerosol formation are assumed to be the major loss mechanisms for these species [e.g., *Jacob and Wofsy*, 1988, 1990; *Hough*, 1991]. The chemistry of the alkyl nitrates formed by $C_5H_8OHO_2$ reaction with NO is condensed into only one reaction. A surrogate species, ONIT, lumps all organic nitrates assumed to be lost for gas phase chemistry. ONIT is assumed to be dry or wet deposited.
4. As the photochemical degradation of isoprene primarily takes place in the continental boundary layer in tropical regions, where deposition processes are important, 70% of the $C_{>3}$ peroxides produced by isoprene oxidation are assumed to be lost by wet or dry deposition [cf. *Jacob and Wofsy*, 1990]. It is assumed that the remaining 30% are photodissociated. An exception is the peroxide formed by MCO_3 + HO_2, which is rapidly oxidized by OH.
5. The Criegge biradicals are assumed to react instantaneously with water vapor (the reactions with NO_x or aldehydes are negligible in nonurban atmospheres). The reaction of pyruvic acid with OH and NO_3 are neglected.
6. The oxidation of terpenes ($C_{10}H_{16}$) is believed to produce an important amount of aerosols. The aerosol yield estimates for α- and β-pinene vary from less than 5% (on a carbon basis) to 50% or even more [e.g., *Zhang et al.*, 1992; *Hatakeyama et al.*, 1989, 1991]. The carbon monoxide yield per terpene molecule oxidized is therefore lower than in the case of isoprene. We assume in this study that the reactions of terpenes with OH, O_3, and NO_3 produce the same compounds as the corresponding reactions of isoprene. The yield of gaseous compounds per carbon atom is thus assumed to be 2 times lower for terpene oxidation than for isoprene oxidation. Terpene reaction rates are the same as for α-pinene reactions. The rate of the reaction OTHC + OH is the rate of *n*-butane reaction with OH.

Table 4. Chemical Reaction Mechanism and Kinetic Rates

Reaction	Rate[a]	Reference
	Inorganic Chemistry	
$O_2+h\nu \rightarrow O+O$		1
$O_3+h\nu \rightarrow O_2+O$		1
$O_3+h\nu \rightarrow O_2+O(^1D)$		1
$O(^1D)+N_2 \rightarrow O+N_2$	1.8(-11) exp(110/T)	1
$O(^1D)+O_2 \rightarrow O+O_2$	3.2(-11) exp(-70/T)	1
$O+O_2+M \rightarrow O_3+M$	6.0(-34) [M] $(300/T)^{2.3}$	1
$O+O_3 \rightarrow O_2+O_2$	8.0(-12) exp(-2060/T)	1
$O(^1D)+H_2O \rightarrow OH+OH$	2.2(-10)	1
$O(^1D)+H_2 \rightarrow OH+HO_2$	1.0(-10)	1
$HO_2+O_3 \rightarrow OH+2O_2$	1.1(-14) exp(-500/T)	1
$OH+O_3 \rightarrow HO_2+O_2$	1.6(-12) exp(-940/T)	1
$OH+HO_2 \rightarrow H_2O+O_2$	4.8(-11) exp(250/T)	1
$OH+OH \rightarrow O+H_2O$	4.5(-12) exp(-240/T)	1
$OH+H_2 \rightarrow H_2O+H$	5.5(-12) exp(-2000/T)	1
$HO_2+HO_2 \rightarrow H_2O_2$	2.2(-13) exp(619/T)	2
$HO_2+HO_2+M \rightarrow H_2O_2+M$	1.9(-33) exp(980/T)	2
$HO_2+HO_2+H_2O \rightarrow H_2O_2+H_2O$	3.1(-34) exp(2820/T)	2
$HO_2+HO_2+H_2O+M \rightarrow H_2O_2+H_2O+M$	2.7(-54) exp(3180/T)	2
$H_2O_2+h\nu \rightarrow OH+OH$		1
$OH+H_2O_2 \rightarrow H_2O+HO_2$	2.9(-12) exp(-160/T)	1
$O(^1D)+N_2O \rightarrow N_2+O_2$	4.9(-11)	1
$O(^1D)+N_2O \rightarrow NO+NO$	6.7(-11)	1
$N_2O+h\nu \rightarrow N_2+O(^1D)$		1
$O_3+NO \rightarrow O_2+NO_2$	2.0(-12) exp(-1400/T)	1
$HO_2+NO \rightarrow OH+NO_2$	3.7(-12) exp(240/T)	1
$NO_2 + h\nu \rightarrow NO + O$		
$NO_2+O \rightarrow NO+O_2$	6.5(-12) exp(120/T)	1
$OH+NO_2+M \rightarrow HNO_3+M$	k_0 = 2.5(-30) $(300/T)^{2.9*}$	3
	k_∞ = 5.2(-11)	
	F_c = exp (-T/353)	
$HNO_3+h\nu \rightarrow OH+NO_2$		1
$OH+HNO_3 \rightarrow H_2O+NO_3$	$k = k_0 + k_3[M]/(1 + k_3[M]/k_2$	1
	k_0 = 7.2(-15) exp (785/T)	
	k_2 = 4.1(-16) exp (1440/T)	
	k_3 = 1.9(-33) exp (725/T)	
$HO_2+NO_2+M \rightarrow HNO_4+M$	k_0 = 1.8(-31) $(300/T)^{3.2*}$	1
	k_∞ = 4.7(-12) $(300/T)^{1.4}$	
	F_c = 0.6	
$HNO_4+M \rightarrow HO_2+NO_2+M$	k_{eq} = 2.1(-27) exp (10900/T)**	1
$HNO_4+h\nu \rightarrow HO_2+NO_2$		1
$HNO_4+OH \rightarrow H_2O+NO_2+O_2$	1.3(-12) exp (380/T)	1
$O_3+NO_2 \rightarrow O_2+NO_3$	1.2(-13) exp (-2450/T)	1
$NO_3+h\nu \rightarrow NO_2+O$		1
$NO_3+h\nu \rightarrow NO+O_2$		1
$NO_3+HO_2 \rightarrow 0.4(HNO_3+O_2)+0.6(OH+NO_2)$	2.3(-12) exp (170/T)	5
$NO_3+NO_3 \rightarrow 2NO_2+O_2$	8.5 (-13) exp (-2450/T)	6

Table 4. (continued)

Reaction	Rate[a]	Reference
	Inorganic Chemistry	
$NO_3+NO_2+M\rightarrow N_2O_5+M$	$k_0 = 2.2(-30)\ (300/T)^{4.3*}$ $k_\infty = 1.5(-12)\ (300/T)^{0.5}$ $F_c = 0.6$	1
$N_2O_5+M\rightarrow NO_3+NO_2+M$	$K_{eq} = 4(-27)\ \exp\ (1093/T)^{**}$	1
$N_2O_5+h\nu\rightarrow NO_3+NO_2$		1
$N_2O_5+H_2O\rightarrow 2HNO_3$	2.7(-22)	1
	Methane Oxidation	
$OH+CH_4\rightarrow CH_3O_2+H_2O$	2.95(-12) exp (-1820/T)	1
$O(^1D)+CH_4\rightarrow OH+CH_3O_2$	1.4(-10)	1
$O(^1D)+CH_4\rightarrow H_2+CH_2O$	1.4(-11)	1
$CH_3O_2+NO\rightarrow CH_2O+NO_2+HO_2$	4.2(-12) exp (180/T)	1
$CH_3O_2+HO_2\rightarrow CH_3OOH+O_2$	3.3(-13) exp (800/T)	1
$CH_3O_2+CH_3O_2\rightarrow 0.6(CH_3OH+CH_2O)+0.8(CH_2O+HO_2)$	2.2(-13) exp (220/T)	1, 4
$CH_3OOH+h\nu\rightarrow CH_2O+HO_2+OH$		1
$CH_3OOH+OH\rightarrow 0.58(H_2O+CH_3O_2)+0.42(H_2O+CH_2O+OH)$	3.8(-12) exp (200/T)	1, 4
$CH_3OH+OH\rightarrow CH_2O+HO_2+H_2O$	6.7(-12) exp (-600/T)	1, 4
$CH_2O+h\nu\rightarrow CO+2HO_2$		1
$CH_2O+h\nu\rightarrow CO+H_2$		1
$CH_2O+OH\rightarrow CO+HO_2+H_2O$	1.0(-11)	1
$CH_2O+NO_3\rightarrow CO+HO_2+HNO_3$	6.0(-13) exp (-2058/T)	6
$CO+OH\rightarrow CO+HO_2$	$1.5(-13)\ (1 + 0.6\ P_{atm})$	1
	Ethane, Ethylene, Propylene, and Butane (OTHC) Oxidation	
$C_2H_6+OH\rightarrow C_2H_5O_2+H_2O$	1.1(-11) exp (-1100/T)	1
$OTHC+OH\rightarrow 2C_2H_5O_2$	1.55(-11) exp (540/T)	7
$C_2H_5O_2+NO\rightarrow CH_3CHO+HO_2+NO_2$	8.9(-12)	1, 4
$C_2H_5O_2+HO_2\rightarrow C_2H_5OOH+O_2$	6.5(-13) exp (650/T)	1, 4
$C_2H_5O_2+CH_3O_2\rightarrow 0.7CH_2O+0.8CH_3CHO+HO_2+0.3CH_3OH+0.2C_2H_5OH$	3.75(-13) exp (-40/T)	1, 4
$C_2H_5O_2+C_2H_5O_2\rightarrow 1.6CH_3CHO+1.2HO_2+0.4C_2H_5OH+O_2$	1.6(-13) exp(-300/T)	1, 4
$C_2H_5OOH+OH\rightarrow 0.5(C_2H_5O_2+CH_3CHO+OH)+H_2O$	3.8(-12) exp (200/T)	1, 4
$C_2H_5OOH+h\nu\rightarrow CH_3CHO+HO_2+OH$	$J(CH_3OOH)$	8, 4
$C_2H_4+OH+M\rightarrow 2/3C_3H_6OHO_2+M$	$k_0 = 9.5(-29)\ (300/T)^{3.1*}$ $k_\infty = 9.5(-12)$ $F_c = \exp\ (-T/840)$	3
$C_2H_4+O_3\rightarrow CH_2O+0.4HCOOH+0.52HO_2+0.4OH+0.18CO_2+0.42CO+0.12H_2+0.02H_2O$	1.2 (-14) exp (-2630/T)	1, 4
$C_3H_6+OH+M\rightarrow C_3H_6OHO_2+M$	$k_0 = 8(-27)\ (300/T)^{3.5*}$ $k_\infty = 3(-11)$ $F_c = \exp\ (-T/433)$	3

Table 4. (continued)

Reaction	Rate[a]	Reference
Ethane, Ethylene, Propylene, and Butane (OTHC) Oxidation		
$C_3H_6+O_3 \rightarrow 0.1CH_3COOH+0.08CH_4+0.585HO_2+0.2875CH_3O_2+0.37CO+0.5325CH_2O+0.4575OH+0.06H_2+0.5CH_3CHO+0.2HCOOH+0.33CO_2$	6.5(-15) exp (-1900/T)	1, 4
$C_3H_6+NO_3 \rightarrow C_3H_6NO_3$	4.0(-15)	4
$C_3H_6OHO+NO \rightarrow CH_3CHO+CH_2O$	4.2(-12) exp (180/T)	1, 4
$C_3H_6OHO_2+HO_2 \rightarrow C_3H_6OHOOH+O_2+HO_2+NO_2$	6.5(-13) exp (650/T)	1, 4
$C_3H_6OHOOH+h\nu \rightarrow CH_3CHO+CH_2O+HO_2+OH$	$J(CH_3OOH)$	8, 4
$C_3H_6OHOOH+OH \rightarrow 0.5(C_3H_6OHO_2+CH_3COCH_2OH+OH)+H_2O$	3.8(-12) exp (200/T)	1, 4
$CH_3CHO+h\nu \rightarrow CH_3O_2+CO+HO_2$		9, 4
$CH_3CHO+OH \rightarrow CH_3CO_3+H_2O$	6.0(-12) exp (250/T)	1
$CH_3CHO+NO_3 \rightarrow CH_3CO_3+HNO_3$	1.4(-12) exp (-1900/T)	1, 4
$CH_3CO_3+NO \rightarrow CH_3O_2+NO_2+CO_2$	5.1(-12) exp (200/T)	10
$CH_3CO_3+NO_2 \rightarrow CH_3CO_3NO_2$	2.8(-12) exp (181/T)	11
$CH_3CO_3+HO_2 \rightarrow 2/3(CH_3COOOH+O_2)+1/3(CH_3COOH+O_3)$	4.3(-13) exp (1040/T)	12
$CH_3CO_3+CH_3O_2 \rightarrow CH_3O_2+CH_2O+CO_2+HO_2$	1.8(-9) exp (-1800/T)	13
$CH_3CO_3+CH_3O_2 \rightarrow CH_3COOH+CH_2O+O_2$	4.1(-15) exp (2100/T)	13
$CH_3CO_3+CH_3CO_3 \rightarrow 2CH_3O_2+2CO_2$	2.8(-12) exp (530/T)	13
$CH_3CO_3NO_2+h\nu \rightarrow CH_3CO_3+NO_2$		14
$CH_3CO_3NO_2+M \rightarrow CH_3CO_3+NO_2+M$	$k_0 = 5(-2) \exp(-12875/T)^*$ $k_\infty = 2.2(16) \exp(-13435/T)$ $F_c = 0.27$	3
$CH_3CO_3NO_2+OH \rightarrow$ products	1.23(-12) exp (-651/T)	3
$CH_3COOOH+h\nu \rightarrow CH_3O_2+OH+CO_2$	0.28 $J(H_2O_2)$	8, 4
$CH_3COOOH+OH \rightarrow CH_3CO_3+H_2O$	1.0(-11)	4
Isoprene and Terpenes Oxidation		
$C_5H_8+OH \rightarrow C_5H_8OHO_2$	2.5(-11) exp (409/T)	4
$C_5H_8+O_3 \rightarrow 0.25MVK+0.25MACR+0.6CH_2O+0.22CH_3O_2+0.21HCOOH+0.67HO_2+0.49OH+0.025CH_3COOH+0.51CO+0.34CO_2+0.08CH_3CO_3+0.05CH_3COHOCHOCHCH_2+0.15CHOCHO+0.12CH_3COCHO$	1.2(-14) exp (-2013/T)	4
$C_5H_8+NO_3 \rightarrow C_5H_8NO_3$	3.0(-12) exp (-450/T)	15
$C_{10}H_{16}+OH \rightarrow as(C_5H_8+OH)$	1.2(-11) exp (444/T)	10
$C_{10}H_{16}+O_3 \rightarrow as(C_5H_8+O_3)$	9.9(-16) exp (-730/T)	10

Table 4. (continued)

Reaction	Rate[a]	Reference
Isoprene and Terpenes Oxidation		
$C_5H_8OHO_2 + NO \rightarrow 0.5MVK + 0.5MACR + CH_2O + HO_2 + NO_2$	3.7(-12) exp (180/T)	4
$C_5H_8OHO_2 + NO \rightarrow 0.59(CH_3CO_3 + CH_2O + CH_2OHCHO + NO_2) + 0.41(CH_3COCHONO_2CH_2OH + CH_2O)$	4.5(-13) exp (180/T)	4
$C_5H_8OHO_2 + HO_2 \rightarrow 0.15(MVK + MACR) + 0.3(CH_2O + HO_2)$	6.5(-13) exp (650/T)	1, 4
$C_5H_8OHO_2 + CH_3O_2 \rightarrow MACR + CH_2O + 2HO_2$	1.3(-14)	4
$C_5H_8OHO_2 + CH_3CO_3 \rightarrow MACR + HO_2 + 0.8CH_3O_2 + 0.8CO_2 + 0.2CH_3COOH$	4.9(-14)	4
$MVK + h\nu \rightarrow CH_3CO_3 + HO_2 + 0.25(CH_2O + CO) + 0.75CHOCHO$		4[b]
$MVK + OH \rightarrow MOHO_2$	8.6(-12) exp (500/T)	4
$MVK + O_3 \rightarrow 0.5CH_3COCHO + 1.01CO + 0.46HO_2 + 0.5CH_2O + 0.2HCOOH + 0.19CO_2 + 0.06H_2 + 0.4CH_3O_2 + 0.8OH + 0.1CH_3COOOH$	4.0(-15) exp (-2000/T)	16
$MACR + h\nu \rightarrow MCO_3 + HO_2$		4[a]
$MACR + h\nu \rightarrow 0.4(CH_3CO_3 + CH_2O) + 0.6(CH_3COCHO + HO_2) + CO + HO_2$		4[a]
$MACR + OH \rightarrow 0.4MOHO_2 + 0.6(MCO_3 + H_2O)$	4.9(-12) exp (500/T)	4
$MACR + O_3 \rightarrow 0.6CH_3COCHO + 0.61CO + 0.76HO_2 + 0.4CH_3O_2 + 0.2HCOOH + 0.1OH + 0.59CO_2 + 0.06H_2 + 0.4CH_2O$	4.4(-15) exp (-2500/T)	16
$MOHO_2 + NO \rightarrow CH_2OHCHO + CH_3CO_3 + NO_2$	3.7(-12) exp (180/T)	4
$MOHO_2 + NO \rightarrow MOHNO_3$	4.5(-13) exp (180/T)	4
$MOHO_2 + HO_2 \rightarrow 0.3CH_3CO_3 + 0.3CH_2OHCHO$	6.5(-13) exp (650/T)	1, 4
$CH_2OHCHO + h\nu \rightarrow CH_2O + CO + 2HO_2$	$J(CH_3CHO)$	4
$CH_2OHCHO + OH \rightarrow 0.5CH_3CO_3 + 0.5CHOCHO + 0.5HO_2$	6.0(-12) exp (250/T)	1, 4
$CHOCHO + h\nu \rightarrow 0.13(CH_2O + CO) + 0.87(2CO + H_2)$		17, 4
$CHOCHO + OH \rightarrow 2CO + HO_2 + H_2O$	1.2(-11)	4
$CHOCHO + NO_3 \rightarrow 2CO + HO_2 + HNO_3$	1.1(-11) exp (2700/T)	4
$CH_3COCHO + h\nu \rightarrow CH_3CO_3 + CO + HO_2$		17, 4
$MCO_3 + NO \rightarrow 0.4(CH_3CO_3 + CH_2O) + 0.6(CH_3COCHO + HO_2) + CO_2 + NO_2$	5.1(-12) exp (200/T)	10
$MCO_3 + NO_2 \rightarrow MPAN$	2.8(-12) exp (181/T)	11
$MCO_3 + HO_2 \rightarrow MOHO_2$	4.5(-13) exp (1040/T)	12
$MCO_3 + CH_3O_2 \rightarrow 1.4CH_2O + 1.6HO_2 + 0.4CH_3CO_3 + 0.6CH_3COCHO + CO_2$	2.2(-12) exp (490/T)	18

Table 4. (continued)

Reaction	Rate[a]	Reference
Isoprene and Terpenes Oxidation		
$MCO_3+CH_3CO_3 \rightarrow 0.4(CH_3CO_3+CH_2O)$ $+0.6(CH_3COCHO+HO_2)+2CO_2+CH_3O_2$	2.8(-12) exp(530/T)	13
$MCO_3+MCO_3 \rightarrow 0.8(CH_3CO_3+CH_2O)$ $+1.2(CH_3COCHO+HO_2)+2CO_2$	2.8(-12) exp(530/T)	13
$MPAN+h\nu \rightarrow MCO_3+NO_2$	J(PAN)	4
$MPAN+M \rightarrow MCO_3+NO_2+M$	k_0 = 5(-2) exp (-12875/T)*	3
	k_∞ = 2.2(16) exp(-13435/T)	
	F_c = 0.27	

1, *De More et al.* [1992]; 2, *Sander et al.* [1982]; 3, *Atkinson et al.* [1989]; 4, *Madronich and Calvert* [1989]; 5, *Hall et al.* [1988]; 6, *Cantrell et al.* [1985]; 7, *Atkinson* [1985]; 8, *Giguere and Olmos* [1956]; 9, *Baulch et al.* [1984]; 10, *Carter* [1990]; 11, *Carter et al.* [1986]; 12, *Moortgat et al.* [1989b]; 13, *Moortgat et al.* [1989a]; 14, *Roberts* [1990]; 15, *Dlugokencky et al.* [1989]; 16, *Lurmann et al.* [1986]; 17, *Plum et al.* [1983]; 18, *Hough* [1991]. *Three-body reaction rates calculated with

$$k\left(\text{cm}^3\ \text{molecule}^{-1}\ s^{-1}\right)=\frac{k_0[M]}{1+k_0[M]/k_\infty}\times F_c^{\left\{1+\left[\log_{10}\left(\frac{k_0[M]}{k_\infty}\right)\right]^2\right\}^{-1}}$$

where $[M]$ is the air density (molec cm^{-3}). **Rates for equilibrium reactions calculated as $k(\text{sec}^{-1})=k_f / K_{eq}$, where k_f is the rate of the formation reaction and K_{eq} is the equilibrium constant.

[a]Units of first-, second-, and third-order reactions are sec^{-1}, cm^3 molecule^{-1} s^{-1}, and cm^6 molecule^{-2} s^{-1}, respectively; read 6.0(-34) as 6.0×10^{-34}.

[b]The absorption cross section for MVK and MACR photodissociations are assumed identical to those of acrolein (CH_2CHCHO); their quantum yields are those of acetone (CH_3COCH_3) and acrolein, respectively.

2.2.3. Photodissociation coefficients. The photodissociation coefficients (also called J values) used in the model are interpolated from tabulated values which were calculated beforehand using a one-dimensional radiative model [*Joseph et al.*, 1976; S. Madronich, personal communication, 1992]. The J values depend primarily on altitude, solar zenith angle, overlying ozone column abundance, surface albedo, temperature, and the presence of clouds. The tabulated values corresponds to clear-sky conditions and selected values of these parameters (except cloud presence). There are 12 altitudes (0, 1, 2, 3, 5, 7, 9, 12, 15, 18, 21, 24 km), 7 zenith angles (Chapman function equal to 1, 1.3, 1.6, 2, 3, 6), 3 albedos (0.05, 0.2, 0.5), 5 ozone columns (0.5, 0.75, 1, 1.25, and 1.5 times the standard ozone column), and 6 different temperature profiles (see below). The model calculates the clear-sky J values at each time step and each grid point by linearly interpolating the logarithm of the J from the table. A correction is made afterward to account for the presence of cloud (see below). The radiative model is based on the delta-Eddington approximation [*Joseph et al.*, 1976; *Madronich*, 1987]. It includes 51 levels in the vertical and 130 spectral intervals. The solar flux is taken from *World Meteorological Organization (WMO)* [1986]. The references for absorption cross sections and quantum yields are given in Table 4.

The clear-sky J values are calculated for six temperatures profiles. A bilinear regression analysis was performed to relate the observed temperature and air density profiles to two parameters, namely, the 500-mbar temperature (T_{500}) and the 200-mbar temperature (T_{200}). The input data for this regression analysis are the latitude- and season-dependent temperature data from *Louis* [1974]. The best fit equations give the most representative temperature and density profiles for each value of the parameters T_{500} and T_{200} within their climatological range. The J values are calculated with the radiative model using temperatures obtained using the best fit equations, for selected values of the 200- and 500-mb temperatures: T_{200} = 205 or 225 K, T_{500} = 228, 248 or 268 K. In IMAGES, T_{500} and T_{200} are calculated by a linear interpolation between the climatological temperatures at the nearest σ levels.

The standard ozone profile is taken from *Nicolet et al.* [1982]. The ozone column above a given point is expressed in IMAGES as the sum of the column between this point and the 100-mbar level and a specified stratospheric column (pressure < 100 mbar) provided by the SAGE I/II instruments [*Fishman et al.*, 1990]. The tropospheric column is calculated by integrating vertically the model-predicted ozone densities. A 5° resolution map of the surface albedo (or reflectance) at 320 nm was established, based on the data of *Demerjian et al.* [1980], *Coulson and Reynolds* [1971], *Kondratyev* [1969], and *Kondratyev et al.* [1982]. The adopted albedo is 5% over the ocean, vegetation, and crops, 15% over subtropical deserts, 20% over sea ice, and 50% over snow and land ice. The land ecosystems are taken from the World Ecosystem Database of *Olson et al.* [1983, 1985], and the sea ice (varying with season) from a geographical atlas [*Neue Welt Atlas*, 1977]. Snow over land or sea ice is assumed to cover 100% for

surface temperatures below -5°C, 0% above +5°C, with a linear variation between -5° and +5°C. The reflectance used in the radiation model is wavelength dependent. It increases with wavelength (in the range 200–500 nm) as

$$a=\frac{1+\alpha}{1+\alpha a_{320}}a_{320} \tag{27}$$

with

$$\alpha=2.5\times10^{-3}\times\max(0,\lambda-320\,\text{nm}) \tag{28}$$

where a_{320} is the reflectance at 320 nm.

The clear-sky J values are corrected to account for cloud cover, using the parameterization of *Chang et al.* [1987]. The cloud amount and optical depth are derived from the ISCCP data (see section 2.1.3) [*Rossow et al.*, 1987; *Rossow and Schiffer*, 1991] and are described by *Pham* [1993]. Different cloud types are not considered here, but instead, a global average cloud is used for the calculations.

As an example to illustrate the calculation of a J coefficient, the rate of the $O_3 \rightarrow O(^1D)$ reaction for the month of April is shown in Figure 5.

2.2.4. Washout parameterization. Washout of soluble gases is parameterized as a first-order loss rate, calculated as a function of the precipitation rate. The in-cloud washout rate for species i is expressed as

$$\beta_i^{\text{in}}=w_i\ 6\times10^{-8}\ P \tag{29}$$

where P is the precipitation rate (millimeter/month), taken from the climatology of *Shea* [1986], and w_i is a dimensionless factor, deduced from the study of *Thompson and Cicerone* [1982] (H_2O_2: 1; HNO_3: 2; HNO_4: 0.5; CH_2O: 0.7; CH_3OOH: 0.5; other organic peroxides: 0.7). The ISCCP distributions of cumulonimbus (Cb) and nimbostratus (Ns) clouds are used to determine the distribution of the washout rate, $\beta_i(\sigma)$:

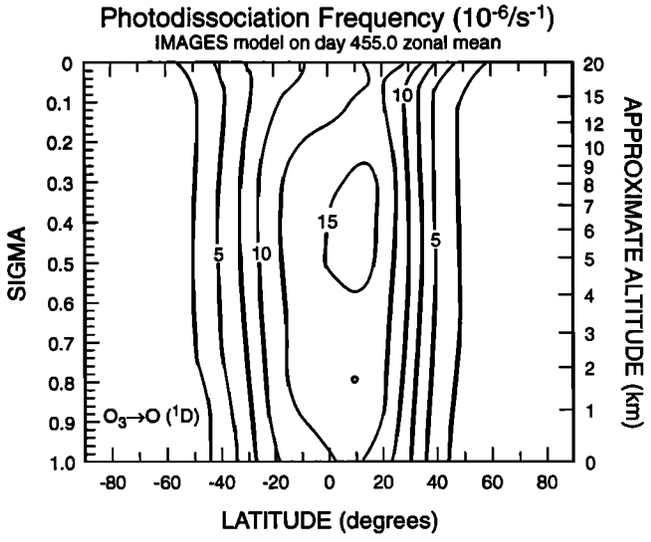

Figure 5. Zonally averaged distribution of the O_3 to $O(^1D)$ photodissociation rate (second^{-1}) calculated by the model for the month of April.

$$\beta_i(\sigma)=\beta_i^{\text{in}}\left(\frac{f_1(\sigma)c_1+f_2(\sigma)c_2}{c_1+c_2}\right) \tag{30}$$

where c_1 and c_2 are the fractional cover of Cb and Ns; $f_i(\sigma)$ is equal to 1 in the cloud layer and decreases smoothly to zero at the cloud top and base. The cloud top pressure is also taken from the ISCCP analysis. The cloud base is situated at 680 and 440 mbar for Ns and Cb clouds, respectively [*Rossow et al.*, 1987].

Note that the use of monthly averages of the precipitation rate in the washout parameterization precludes a realistic representation of the atmospheric variability of rainout. The episodic character of rain is believed to increase the average lifetime of soluble species [e.g., *Georgi and Chameides*, 1986]. However, although our parameterization of washout is crude, the annual wet deposition of HNO_3 and organic nitrates over North America is calculated to be about 2 Tg(N)/yr, in good agreement with earlier estimates (see section 3.2).

2.2.5. Aerosol reaction of N_2O_5 and other species. N_2O_5 and possibly NO_3 are believed to undergo heterogeneous reactions on atmospheric aerosols and cloud/fog droplets, likely producing nitric acid [e.g., *Heikes and Thompson*, 1983; *Platt et al.*, 1984]. The observed nighttime loss rate of the NO_3 radical in clean air as well as in polluted areas and the observed production of HNO_3 and NO_3^- in clouds and plumes are probably due to these processes, although homogeneous NO_3/N_2O_5 reactions have also been invoked as possible explanations [*Johnston et al.*, 1986; *Atkinson et al.*, 1986]. The rate of the gas phase $N_2O_5 + H_2O$ reaction, however, is certainly too slow to account for the observations. The reaction probability (or sticking coefficient) of the heterogeneous reaction of N_2O_5 on typical tropospheric aerosols (NH_4HSO_4) has been measured by *Mozurkewich and Calvert* [1988]. This probability (γ) was found by the authors to lie in the range 0.05–0.1 for relative humidities above the deliquescence point of the aerosol (RH 40% for NH_4HSO_4 aerosols). The deliquescence point is the relative humidity above which the aerosol may pick up water from the air. The liquid phase is believed to be necessary for the reaction to occur, although lower but nonzero γ have been measured for RH below the deliquescence point. The deliquescence RH for other typical sulfur aerosol lies in the range 30–90% [*Charlson et al.*, 1978]. The reaction probability on nonsulfur aerosols may be lower than the γ measured by *Mozurkewich and Calvert*, due to their different physical properties. *Heikes and Thompson* [1983] derived the first-order loss rate for NO_3 and N_2O_5 reactions on particles, for a wide range of reaction probability and particle density, assuming a reasonable particle size distribution. Typical background surface aerosol densities are around 10^3 cm^{-3}, while densities up to 2 orders of magnitude higher may be found in polluted areas, where sulfates are abundant.

On the basis of this information we parameterize the rate of the NO_3 and N_2O_5 heterogeneous reaction as a first-order loss rate calculated with

$$\beta_{\text{het}}=10^{-4}\times\left(1-\exp^{-2\text{RH}}\right)\left(\sigma^2+[SO_4]/[SO_4]^*\right) \tag{31}$$

where σ is the vertical coordinate (as defined in equation (2)), RH is the relative humidity, and $[SO_4]$ is the sulfate concentration (monthly averaged, in molecule/cm^3) calculated by *Pham* [1993] for the present-day conditions (see also M. Pham et al. (A three-dimensional study of the tropospheric sulfur cycle, submitted to *Journal of Geophysical Research*, 1994)). *Pham* [1993] modeled the distribution of the major sulfur species using the IMAGES

model, with a detailed description of the tropospheric sulfur cycle (emissions, homogeneous and heterogeneous chemistry, deposition). The modeled sulfate distributions agree reasonably well with observations, when available [*Pham*, 1993]. $[SO_4]^*=3 \times 10^9$ molecule/cm^3 is a reference sulfate density, typical of moderately polluted surface air. The RH factor in equation (31) increases slowly with RH for relative humidities typical of the troposphere and is equal to zero for RH = 0. The σ^2 term in equation (31) is a tentative parameterization of the background aerosol vertical distribution, while the $[SO_4]$ term represents the sulfate aerosol distribution. Our calculated three-dimensional distribution of β_{het} agrees broadly with the results of *Dentener and Crutzen* [1993], who used another parameterization and the sulfate distributions predicted by the MOGUNTIA model [*Langner and Rodhe*, 1991]. Sensitivity studies with IMAGES show that the global distributions of trace gases are not very sensitive to the details of the parameterization of β_{het}. In particular, higher values of β_{het} have no significant impact on the global budget of nitrogen oxides. The reason is that the sulfate concentration and hence β_{het} are large enough to ensure an almost complete conversion of NO_3 and N_2O_5 to HNO_3 during the night in regions where NO_x levels are high (i.e., in the polluted atmosphere). The tests show also that the (unchecked) assumption of a NO_3 aerosol loss leads to a substantial reduction of nitrate levels but does not affect significantly the global budget of the other species.

Although little information is available about the aerosol reactions on other species, especially organic compounds, we assumed that NO_3 and several oxygenated hydrocarbons (the ketones CHOCHO, CH_3COCHO, MACR, and MVK) also undergo irreversible reaction on aerosols. NO_3 is converted to HNO_3, while the oxygenated hydrocarbons are assumed to be lost for gas phase chemistry. The reaction rate is taken equal to β_{het} of equation (31). Although the nitrate conversion to nitric acid is found to be of only minor importance in tropospheric chemistry, the photochemical production of CO, the reduction of the hydroxyl level, and the production or sink of ozone due to nonmethane hydrocarbon (NMHC) oxidation are significantly reduced when aerosol reactions on organics are taken into account. As our assumptions are largely unchecked, these results emphasize the need for further experimental investigation of the role of aerosol reactions on organic compounds.

2.2.6. Diurnal cycle of concentrations. It is well known that significant errors are associated with diurnal mean concentrations when calculated using fixed, averaged photodissociation coefficients [*Kurzeja*, 1975; *Turco and Whitten*, 1978]. These errors are due to the non linear behavior of chemical systems. However, it would be prohibitively expensive in terms of computer time requirements to account for the diurnal cycle throughout the entire simulation, as a time step much smaller than 1 day would be required to represent diurnal variations. In IMAGES the diurnal cycle is explicitly calculated during 3 days at the beginning of each month. Diurnally averaged concentrations are calculated during the remaining of the month, using diurnally averaged photodissociation coefficients and reaction rates corrected to account for night/day variations of the concentrations, according to *Turco and Whitten* [1978]. The correction factors depend on the ratios of the average nighttime concentrations over the average daytime concentrations of the chemical species. These ratios are estimated using the concentrations of the species calculated for the last day of the 3-day simulation of the diurnal cycle.

2.3. Emissions and Deposition Velocities

The trace gas surface emissions and deposition velocities used in the model are based on the detailed inventory of *Müller* [1992], with a few modifications. The global emissions are summarized in Table 5. Figure 6 displays the zonally averaged emissions of CO, CH_4, NMHC and NO. The geographical distribution of total CO emissions in June and December is shown in Figure 7.

2.3.1. Technological sources. Technological sources include the emissions due to oil, gas and coal burning, industrial activities, and waste disposal. The surface emission estimates by *Müller* [1992] are based on available national emissions statistics from the *Organization for Economic Cooperation and Development (OECD)* [1989] for western Europe, North America, Japan, Australia, and New Zealand; energy and industry statistics from *United Nations (UN)* [1986; 1988a], combined with emission factors taken from the literature, are used to determine the emissions in other countries, or when OECD estimates are lacking. Geographical distributions at a resolution of 5° × 5° are determined from population density and information about the localization of industrial or mining activities. The seasonal variation of technological emissions is determined from the seasonal variation of fossil fuel use and production and from the temperature dependence of vehicle emissions. The individual emissions of C_2H_6, C_2H_4, C_3H_6, and OTHC used in this study are deduced from the estimate for total

Table 5. Global Emissions of Trace Gases, by Category (Tg/yr)

	Technological Sources	Biomass Burning	Biogenic Sources, Continental	Oceans	Total
CO	383	715	165	165	1428
NO_2	72	14	22	0	108
CH_4	132	53	290	10	485
NMHC	97	50	498	138	783
C_5H_8	0	0	250	0	250
$C_{10}H_{16}$	0	0	147	0	147
C_2H_6	8	8	1	1	18
C_2H_4	5	12	5	10	32
C_3H_6	2	6	1	50	59
Other hydrocarbons	82	24	94	77	277

NMHC, nonmethane hydrocarbons.

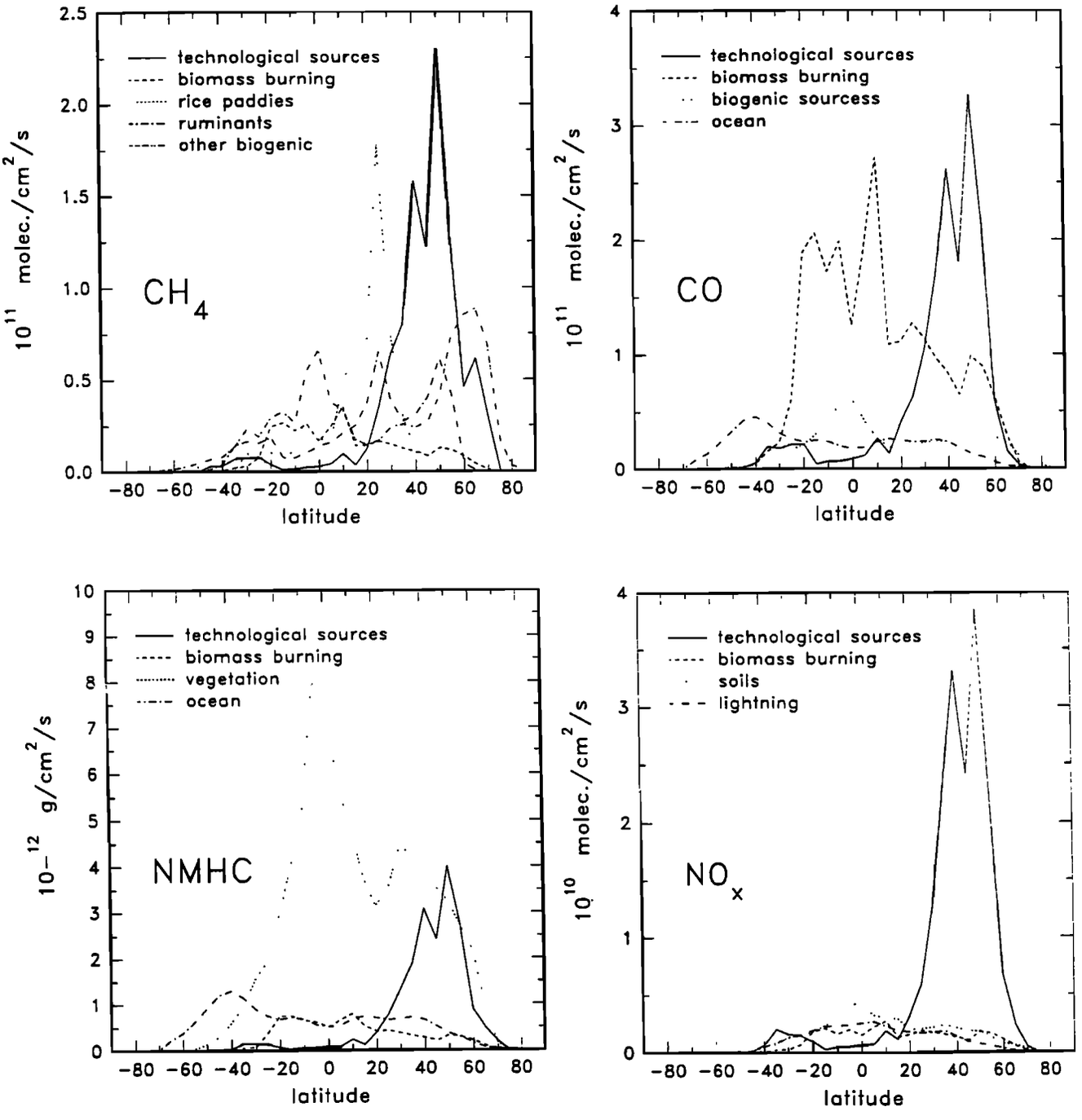

Figure 6. Zonally averaged emissions of CH_4, CO, nonmethane hydrocarbons (NMHC), and NO_x.

NMHC emission by *Müller* [1992] and the data on United States emissions for organic compounds by *Middleton et al.* [1990].

Aircraft emissions might be a significant source of nitrogen oxides in the upper tropospheric midlatitudes, even if the global source is small when compared with the surface emissions [e.g., *Ehhalt et al.*, 1992]. The three-dimensional distribution of aircraft emissions produced by the Boeing Corporation (private communication, 1993) is used in this study. The global source is estimated to be equal to 1.46 $Tg(NO_x)/yr$, or 2% of the technological source of NO_x. It is, however, released in the upper troposphere and lower stratosphere where the lifetime of NO_x is thought to be longer than in the planetary layer. The aircraft emissions of other species (CO, CH_4, NMHC) are ignored, as they represent a much smaller fraction of the surface emissions of these compounds.

2.3.2. Biomass burning. Biomass burning is mainly due to forest and savanna fires, although fuelwood burning and agricultural wastes burning are also significant. CO_2 and various reactive trace gases are emitted as a result of biomass burning. The CO_2 emissions due to tropical fires are taken from the study of *Hao et al.* [1990], with minor modifications. The savanna burning emissions from Hao et al. were reduced in dry areas (where precipitation is much less than 700 mm/yr), as the low biomass density in the dry savanna does not allow important fire development. This reduction affects mainly the emissions estimate in Australia, Sahel, and around the Kalahari Desert.

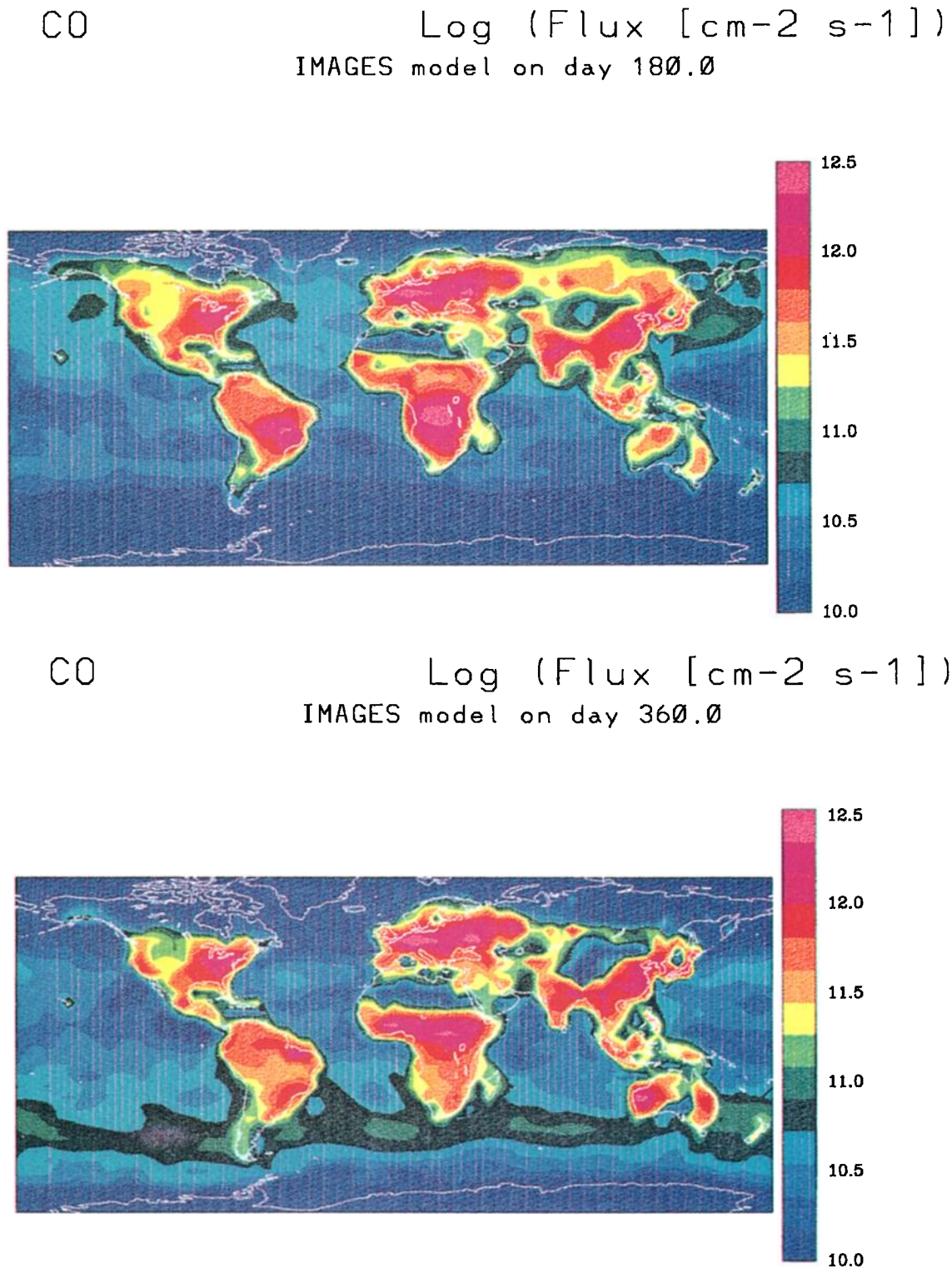

Figure 7. CO emissions (molecule/cm^2/s, expressed in decimal logarithm) (a) in June and (b) in December.

Global annual emissions of CO_2 due to these tropical forest and savanna fires amount to 500 and 1230 Tg(CO_2-C), respectively. Available estimates of the annually burned area of forest in countries of Europe and North America are used to determine the forest fire emissions in nontropical regions. These fires contribute to 320 Tg(CO_2-C)/yr globally. *Müller* [1992] used the fuel wood statistics of the *Food and Agriculture Organization (FAO)* [1987] to estimate the amount of CO_2 emitted as a result of fuelwood burning. These emissions are multiplied by 1.5 in this study to account for nonmarketed wood, omitted in the FAO statistics. The emissions due to the burning of agricultural wastes are assumed to be proportional to the product of population density and fractional cropland coverage. Fuelwood and agricultural waste burning amounts globally to about 660 and 355 Tg(CO_2-C)/yr, respectively. The seasonal variation of forest and savanna fires is parameterized using climatological precipitations

and temperatures. Emissions of gases other than CO_2 resulting from biomass burning are estimated by assuming constant emission ratios to CO_2, except in the case of NO_x. In this study, NO_x emissions are calculated by adopting the N/C ratios estimated by *Hao et al.* [1991] (forests, 1.4%; savanna, 0.7%; fuel wood, 0.4%; agricultural wastes, 1.7%). The conversion efficiency factor (fraction of fixed nitrogen being oxidized to NO_x) is 13% for woods and 10% for shrub [*Galbally*, 1985]. The calculation of NMHC emissions by biomass burning assumes a hydrocarbon mixture composition based on the measurements in Brazil by *Greenberg et al.* [1984]. The volume fractions of total NMHC emissions are 21% C_2H_6, 9% C_3H_8, 2% other alkanes, 35% C_2H_4, 11% C_3H_6, 6% other alkenes, 7% alkynes, 7% C_6H_6, 1% C_7H_8, and 4% other species. The corresponding average carbon number and molecular mass are 2.8 and 39.3, respectively. Global emissions amount to 50 Tg/yr, or 43 TgC/yr. C_2H_6, C_2H_4 and C_3H_6 fluxes account for 26 Tg/yr or 53% of these emissions. Other species are represented by a surrogate, OTHC. OTHC has the same chemical lifetime and carbon number as n-C_4H_{10}. Its biomass burning emission rate is chosen so that global emissions amount to the remaining 47% of total NMHC emissions (24 Tg/yr).

2.3.3. Biogenic sources. The foliage emissions of isoprene and other NMHC calculated by *Müller* [1992] depend on vegetation type, temperature, day length, and net primary productivity (NPP). NPP is used to represent the geographical variation of leaf biomass in each ecosystem. It is calculated for each month of the year as a function of climatic variables (monthly mean temperature and precipitations), using the empirical relationships of the Miami model [*Lieth*, 1975] established for annual mean conditions [*Müller*, 1992; *Taylor et al.*, 1991]. A simple diurnal variation of the isoprene and terpene emissions is assumed in the model when the diurnal cycle of the concentrations is calculated [*Müller*, 1993]. The biogenic emissions of NO and CO are simple functions of temperature, vegetation type, and NPP. All ocean emissions (CO, CH_4, and NMHC) are distributed according to the ocean emission of CO derived by *Erickson* [1989]. The total source of NMHC from the ocean is taken to be 138 Tg/yr. The estimates of Table 5 for biogenic and ocean emissions of C_2H_6, C_2H_4, and C_3H_6 and OTHC are derived from the studies of *Ehhalt and Rudolph* [1984] and *Bonsang et al.* [1988]. The ocean emissions of C_3H_6 and OTHC are larger than estimated by these authors but agree better with the findings of *Donahue and Prinn* [1990].

The biogenic source of methane includes the emissions from ruminants, rice paddies, wetlands, and termites. The ruminant source is distributed as the cattle population (cows and buffaloes), whose distribution is determined from the statistics of *FAO* [1987]. No seasonal variation is assumed for this source. The emissions from paddy fields are proportional to the product of NPP and paddy area. The geographical distribution of paddy fields area is also determined from *FAO* [1987]. The wetland and termite sources are determined from NPP and the fractional cover of wetlands and tundra from the ecosystem database of *Olson et al.* [1983, 1985]. As the resolution of this database is 0.5°, dispersed wetlands smaller than this size (about 50 km) are not included. The emissions due to the large wetlands included in the database are assumed to be proportional to NPP and the wetland coverage. The remaining emissions from wetlands (taken to represent 50% of the total source) as well as the emissions from termites are assumed to be distributed as NPP. The global emissions from these biogenic sources are taken from current estimates [e.g., *Cicerone and Oremland*, 1988; *Khalil et al.*, 1990] and scaled to provide a total of 290 Tg(CH_4)/yr. The adopted global emissions from ruminants, rice paddies, wetlands, and termites are 80, 100, 100, and 10 Tg(CH_4)/yr, respectively; 30% of the wetland emissions is situated north of 50°N, in close agreement with the results of *Aselmann and Crutzen* [1989].

2.3.4. Lightning. The production of NO following nitrogen fixation by lightning flashes is a significant source of atmospheric NO_x. The global source is very uncertain, with estimates ranging from about 1 to 220 Tg(N)/yr [e.g., *Chameides et al.*, 1977; *Borucki and Chameides*, 1984; *Liaw et al.*, 1990]. In our study, the production of NO is distributed according to the number of lightning flashes detected at dusk by a satellite [*Turman and Edgar*, 1982]. It has been shown that the 24-hour average of the flash frequency is close to its instantaneous value at dusk [see *Turman and Edgar*, 1982]. The production of NO from this source is taken to be 8 Tg(N)/yr [*Logan*, 1983]. NO production is set to zero in the two upper levels of the model, and is kept constant with altitude below these levels.

2.3.5. Deposition velocities. Some trace gases undergo irreversible absorption at the Earth's surface (dry deposition), particularly in the presence of vegetation. The so-called deposition velocity (v_d) is determined by the species-independent aerodynamic resistance (r_a) and by the species-dependent surface resistance (r_s) such that

$$v_d = \frac{1}{r_a + r_s} \tag{32}$$

For certain species such as HNO_3, the surface resistance can be neglected and the deposition velocity is determined only by aerodynamic parameters such vertical mixing above the surface (see for example, *Hicks and Liss* [1976], *Warnek* [1987], or *Chang et al.* [1987]). In this model we have adopted a single value of 50 s/m for r_a. In contrast, dry deposition is determined only by the surface resistance r_S for species such as CO and CH_4.

The geographical distribution of surface resistance for ozone, nitrogen oxides, methane, and carbon monoxide has been adopted from the analysis by *Müller* [1992]. For example, in the case of ozone the average deposition velocity is 0.075 cm/s over water, ice, and snow, 0.4 cm/s over bare ground and grass, 0.5 cm/s over savanna, 1 and 0.6 cm/s over tropical and nontropical forests. The observed diurnal variation in the deposition is taken into account [see *Müller*, 1993], using

$$\frac{v_d^{\text{day}}}{v_d^{\text{night}}} 2.7 \times (\bar{v}_d - 0.2)^3 + 4 \times \bar{v}_d + 0.67 \tag{33}$$

The deposition velocity of methane varies with the type of ecosystem and the surface temperature. For CO, v_d is assumed to be proportional to the NPP. The deposition velocities for the other species, given in Table 6, are derived from *Chang et al.* [1987], *Warnek* [1987], and *Hough* [1991]. As suggested by *Isaksen et al.* [1985], an effective deposition velocity at the first model level (at height z above the ground) is determined from its value near the surface, by

$$v_{\text{eff}} = \frac{v_d}{1 + v_d z / K_{zz}} \tag{34}$$

where K^{zz} is the vertical eddy diffusion coefficient at the first model level.

Table 6. Deposition Velocities Used in the Model (cm/s)

	Land	Ocean	Ice/Snow
H_2O_2	$r_s = r_s(O_3)/6$	1	0.05
HNO_3	2	1	0.05
PAN and MPAN	$v_d(O_3)/3$	$v_d(O_3)/3$	$v_d(O_3)/3$
ONIT	$v_d(H_2O_2)$	$v_d(H_2O_2)$	$v_d(H_2O_2)$
CO	NPP/2*	0	0
CH_2O	$v_d(O_3)$	$v_d(O_3)$	$v_d(O_3)$
Organic peroxides	$v_d(H_2O_2)/2$	0.5	0.025

Value of r_S is the surface resistance (cm), as explained in text. *NPP in kg (dry matter)/m^2/month.

2.4. Initial Conditions and Simulation Parameters

Although the initial distributions of short-lived chemical species do not influence the calculated concentrations after a few time steps, it is important to specify realistic distributions for less reactive species. In the case of methane a latitudinal profile of its surface mixing ratio based on the observations reported by *Steele et al.* [1987] for January 1985 have been used as initial concentrations at the surface; the initial mixing ratio decreases linearly with height up to the two uppermost levels, where it is specified to be 1.6 ppmv. Similarly, the initial mixing ratio of ozone varies linearly with σ between the surface (where a 20 ppbv value is adopted) and the $\sigma = 0.10$ level (about 145 mbar). In the three uppermost levels ($\sigma = 0.10$, 0.05, and 0) we used latitudinal profiles based on a compilation of ozonesonde measurements [*Komhyr et al.*, 1992], completed with a tropical profile (Natal) from *Logan and Kirchhoff* [1986]. The ozonesonde data are local measurements, but they are more accurate than, for example, satellite-derived distributions. They were extrapolated to all latitudes and seasons with the help of the global satellite observations of *McPeters et al.* [1984]. Note that the ozonesonde profiles are middle to late 1980s observations and therefore include the Antarctic ozone depletion in spring. The resulting latitude profiles are also used to specify the boundary conditions of ozone at the top of model domain. In the case of HNO_3, the satellite observations reported by *Gille et al.* [1987] are used for the upper boundary condition.

The model simulation runs from January 1 to December 31 of the second year. The results presented and discussed in the next section correspond to the second year of the simulation. Calculations performed with a low-resolution version of the model (8 longitudes rather than 72) suggest that a quasi-equilibrium is reached in less than 2 years if emissions and dynamical conditions do not change from one year to another. The model simulations are performed on the NCAR Cray-YMP/8. Approximately 14 hours of computer time on one processor are required for a 2-year integration. The model results are intended to represent the atmosphere during the 1980s rather than a specific year. As indicated earlier, the dynamical fields and the surface emissions reproduce climatological means as opposed to instantaneous values with high variability. The focus in the discussion of the results will therefore be on the global budgets of species, such as O_3, CH_4, OH, CO, and NO_x, which directly govern the oxidation capacity of the atmosphere.

3. Model Results and Discussion

Only selected aspects of global tropospheric chemistry will be considered in the discussion of the model results presented in this section. More detailed studies will be presented in forthcoming papers. Although the model calculates the distribution of 40 species, the discussion will focus mainly on the key tropospheric compounds, namely, methane, carbon monoxide, nitrogen oxides, the hydroxyl radical, and ozone.

3.1. Methane and Other Hydrocarbons

Because of its long lifetime the distribution of methane in the troposphere is nearly homogeneous, and its seasonal change is small. Near the surface, however, significant variations in its concentration are predicted (Figure 8). In June the largest mixing ratios (2 ppmv) are found over northern Asia, where rice paddies and cattle provide a large methane source. The high concentrations calculated over Europe and the eastern United States result mainly from coal mining activities, natural gas leaks, and waste disposal. The maximum value over the western part of the former Soviet Union (> 1.8 ppmv in Ukraine) is related to intense coal mining and the high loss rate associated with natural gas exploitation (assumed to be 10% of the production). The calculated interhemispheric concentration mixing ratio is about 1.06 (Figure 9), in good agreement with the observations [e.g., *Steele et al.*, 1987].

A comparison between the calculated and the observed seasonal variation of methane at several sites is shown in Figure 10. The data are expressed relative to the mixing ratio observed at the south pole (except at the south pole itself where absolute values are given). The agreement between observed and calculated values is generally good, except at Samoa (14°S) where the model slightly underestimates the methane concentration and at Point Barrow (71°N) where the seasonal variation is misrepresented by the model.

As indicated in Table 7, the only significant source of methane is provided by its surface emissions (485 Tg/yr), which are not entirely balanced by its photochemical destruction (397 Tg/yr) in the atmosphere. The surface deposition (8.5 Tg/yr) is small and the net imbalance in the budget leads to a global increase of 79 Tg/yr. The corresponding increase in the mixing ratio (1.7%/yr) is somewhat higher than observed during the 1980s [*Blake and Rowland*, 1986]. This suggests a slight overestimation of the source and/or the chemical lifetime. However, the difference between the observed and the computed trends corresponds to about 40 Tg/yr or less than 10% of the total annual source. Even small source/sink uncertainties lead to large error in the imbalance calculation. The global budget established by the model is consistent (within the error bars) with the recent studies by *Fung et al.* [1991] and *Crutzen.* [1991]. The calculated residence time is 11 years, in good agreement with the recent estimates using methylchloroform (CH_3CCl_3) observations to derive globally averaged OH concentration [*Prinn et al.*, 1992; *IPCC*, 1992].

Because the chemical lifetimes of other hydrocarbons are several orders of magnitude smaller than the lifetime of methane, their atmospheric distribution is characterized by much stronger geographical and temporal variability. The chemical lifetimes of isoprene, monoterpenes, and propylene are so short (a few hours) that average concentrations cannot easily be established from local observations. For these species, comparison of measurements with global models are almost meaningless. As shown in Figure 11, the mixing ratio of isoprene is significant only near the surface in the regions where sources are intense, up to 1 ppbv at the equator. The mixing ratio decreases by about 3 orders of magnitude between the surface and the middle troposphere. The isoprene distribution shows a secondary

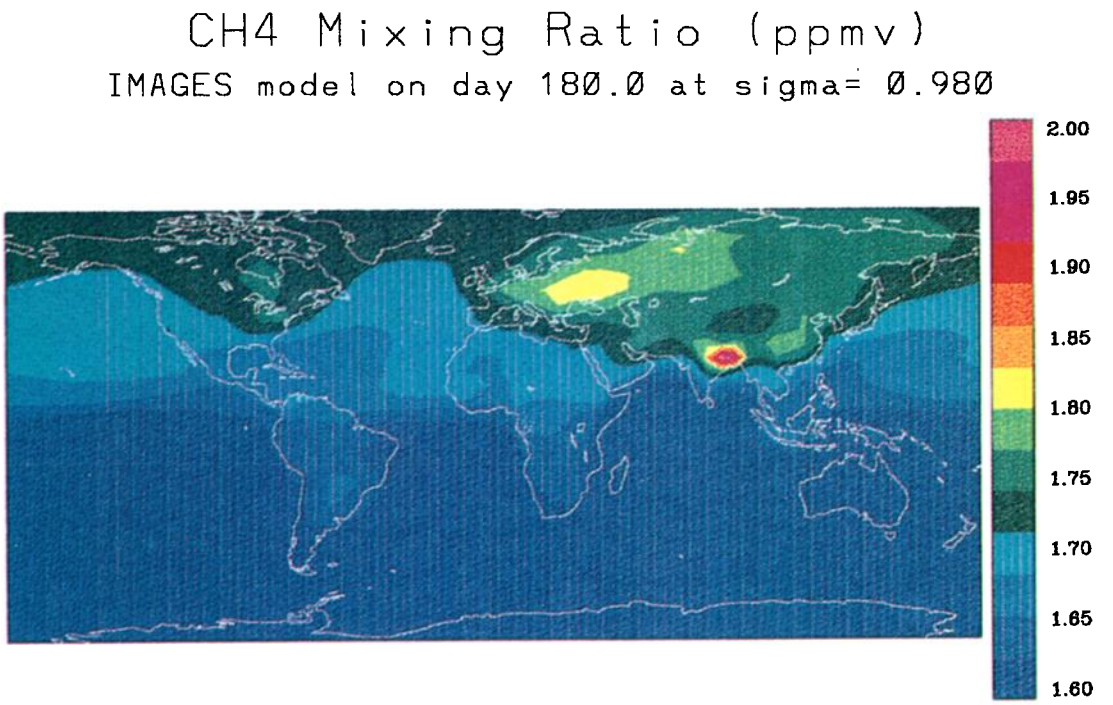

Figure 8. Distribution of the methane mixing ratio (parts per million by volume) in June, at $\sigma = 0.98$ (approximately 140 m above the surface).

maximum in the upper troposphere, due to vertical transport in convective clouds and the lower hydroxyl concentration in the upper troposphere. The predicted maximum in the equatorial upper troposphere is a recurrent feature for most short-lived species that are produced at the surface or in the planetary boundary layer, such as biogenic hydrocarbons and, for example, formaldehyde. In the case of ethane, whose global lifetime is about 3 months, the calculated concentrations are more homogeneous and can be compared with observational data. The zonally averaged distribution of ethane in June is shown in Figure 12. Because of the large anthropogenic contribution to its surface source the largest mixing ratios of ethane are found in the northern high latitudes, with a maximum in winter, when destruction by OH is slow.

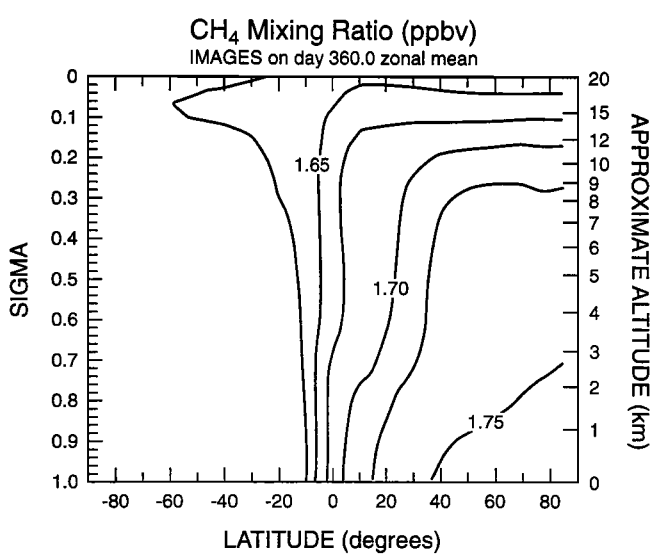

Figure 9. Zonally averaged distribution of the methane mixing ratio (parts per billion by volume) in December.

The calculated mixing ratio of ethane is compared with observations as a function of latitude (Figure 13) and altitude (Figure 14) for specific conditions. The vertical profile as well as the seasonal variation at Moffett Field (Pacific coast in California) are well represented by the model. The latitude profiles are also in good agreement, except that the average mixing ratio in the southern hemisphere is somewhat higher than in the observations. At 5°N over the Atlantic Ocean the model predicts also a pronounced peak which is not found in the measurements. These discrepancies might imply that the OH abundance is too low or that the savanna-burning emissions are too high in the model. This latter conclusion is partly supported by the recent study of *Hao and Ward* [1993]. With a higher combustion efficiency for savanna burning than for other fires, the emissions rates for hydrocarbons and CO should be lower than assumed in this study.

3.2. Carbon Monoxide

The dominant surface emissions of carbon monoxide are the burning of biomass (mostly in tropical regions) and fossil fuels (mostly in industrialized regions). The direct emissions by the biosphere (oceans and continents) represents around 10% of its total production. CO is also a product of the oxidation of methane and other hydrocarbons. CO is a key species in atmospheric chemistry, because its reaction with the hydroxyl is the principal tropospheric sink of OH. The calculated average lifetime of CO is about 2 months. The CO density is largest near the surface sources of the tropics and northern hemisphere and during winter when the destruction rate by the OH radical is small (Figures 15a–15b). In June the mixing ratio is predicted to be about 60–75 ppbv in the southern hemisphere and 80–110 ppbv in the northern midlatitudes. Comparison with the aircraft measurements of the STRATOZ-III mission in June 1984 [*Marenco et al.*, 1989] shows in most cases a good agreement in the southern hemisphere and the tropical regions. For example, the maximum in the equatorial upper troposphere and the relative minimum in the midtroposphere at 20°N are well reproduced by the model. In the northern high latitudes, however, the model

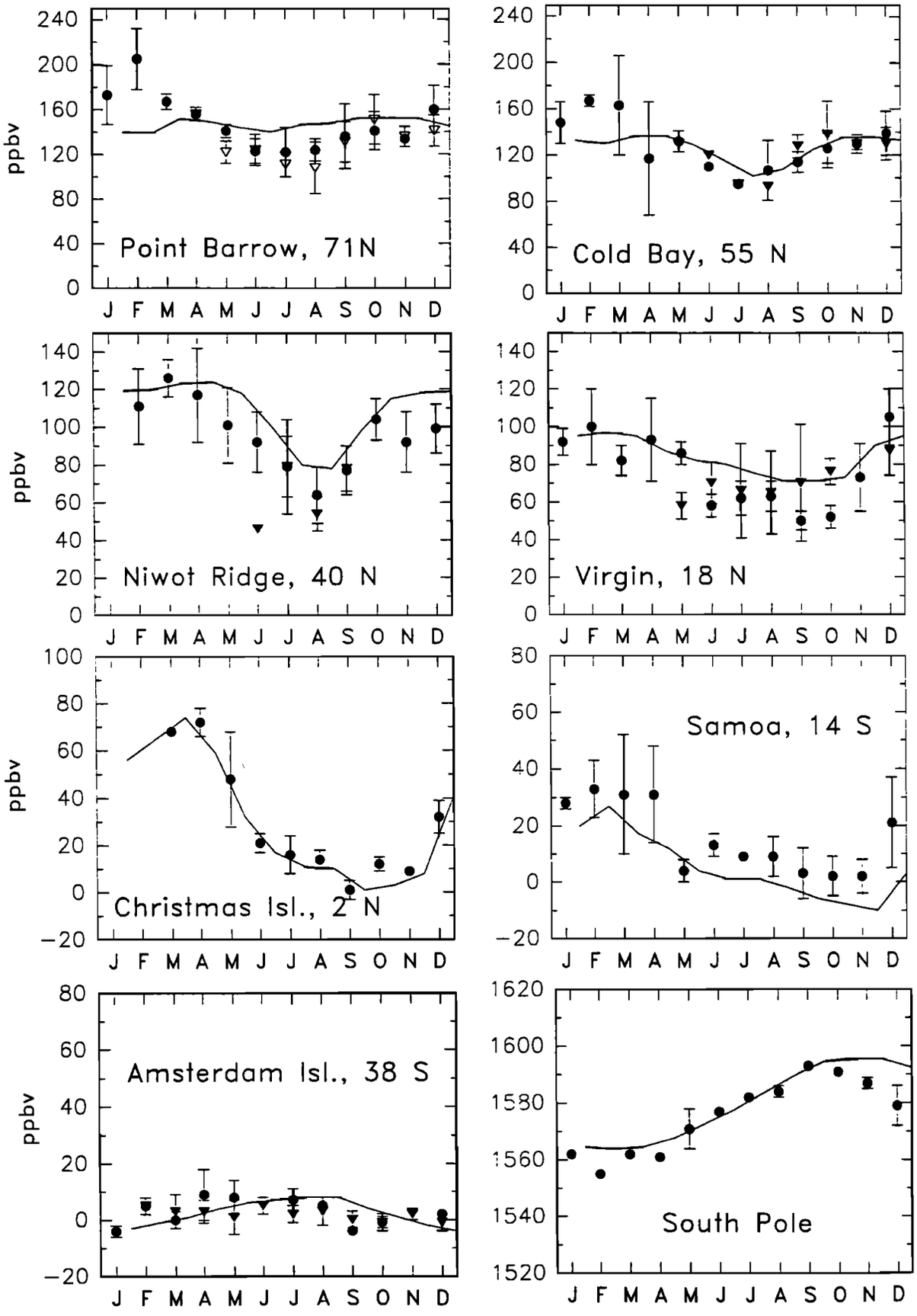

Figure 10. Observed and calculated surface mixing ratio of methane (ppmv) at several sites. The south pole mixing ratio has been subtracted to data at all sites (except south pole). Triangles, 1983 data; circles, 1984 data; solid curve, model. The calculated mixing ratio at south pole has been scaled to the average 1984 data. The data are taken from *Steele et al.* [1987].

Table 7. Annual Budget of CH_4 in the Model Domain, in Teragrams Per Year

Source/Sink Type	Magnitude
Sources	
surface emission	484.6
$C_3H_6 + O_3$	0.3
total	484.9
Sinks	
chemical loss	397.4
dry deposition	8.5
total	405.9
Imbalance	79 (1.7% of the burden)
Burden, Tg	4517
Chemical lifetime	11.4 y
Residence time	11.1 y

underestimates the CO mixing ratio. In December the calculated mixing ratios are of the order of 60–80 ppbv in the southern hemisphere and 100–140 ppbv in the northern hemisphere. The CO concentration decreases rapidly with altitude in the vicinity of the tropopause.

The distribution of the vertically integrated CO density (Figures 16a–16b) reflects the amplitude of the emission sources with their seasonal variations and the effect of intercontinental transport. Biomass burning is highly seasonal and is most intense during the dry season, i.e. broadly, from December to April in the northern hemisphere and from July to October in the southern hemisphere. For example, in June the effect of biomass burning (leading to surface mixing ratios of approximately 350 ppbv in south central Africa) is most pronounced in the southern continental tropics. In December the highest CO abundances are predicted to occur over the northern part of tropical Africa (up to 500 ppbv). Large amounts of CO are found over Europe where the surface mixing ratio reaches 200 ppbv in summer and 300 ppbv in winter; these values are significantly higher than over the eastern United States (150 ppbv). The maps shown in Figures 16a–16b show that substantial amounts of CO are transported from the continents to the oceans. They reproduce a large number of features seen in the measurements made from the space shuttle in October 1984 and reported by *Reichle et al.* [1990].

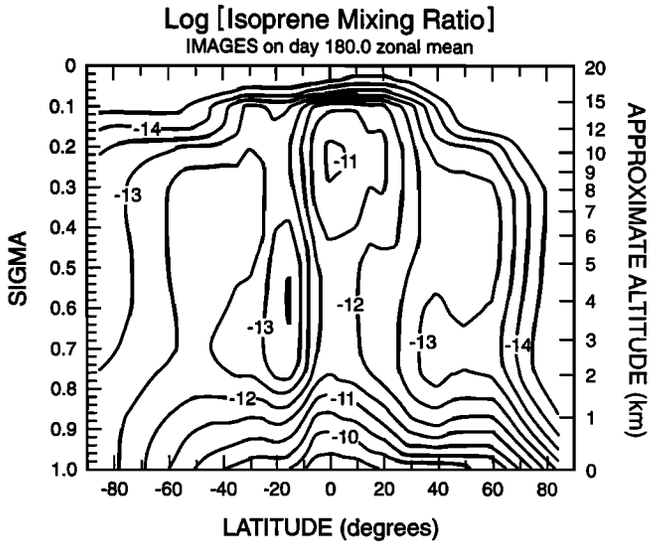

Figure 11. Zonally averaged distribution of the isoprene mixing ratio (expressed in decimal logarithm) in June.

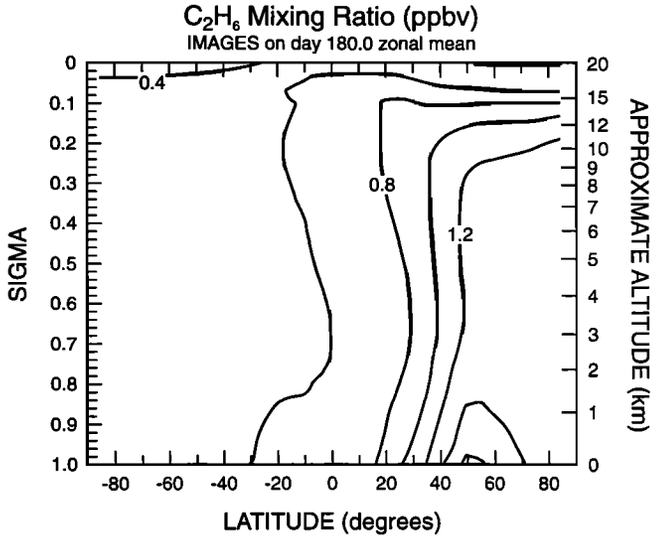

Figure 12. Zonally averaged distribution of the mixing ratio of ethane (C_2H_6) (ppbv) in June.

The calculated mixing ratio of CO is compared in Figure 17 to observations made at selected sites. In general, the model predicts too small a concentration of carbon monoxide at high latitudes in the northern hemisphere. This discrepancy could be explained by an overestimation in OH or an underestimation in the anthropogenic source of CO. The agreement between model and observations is improved at lower latitudes. The observed and predicted peak at Cuiaba (Brazil, 16°S) in July–October is a consequence of intense biomass burning. The comparison for Cape Point suggests that the CO mixing ratio is overpredicted by the model in southern midlatitudes. As in the case of ethane, this might be due to an under prediction of OH and/or an overestimation of the total CO source in the southern hemisphere (880 Tg/yr in the model, including the interhemispheric flux). Biomass burning and hydrocarbon oxidation are the largest contributions to the CO budget in the southern hemisphere (294

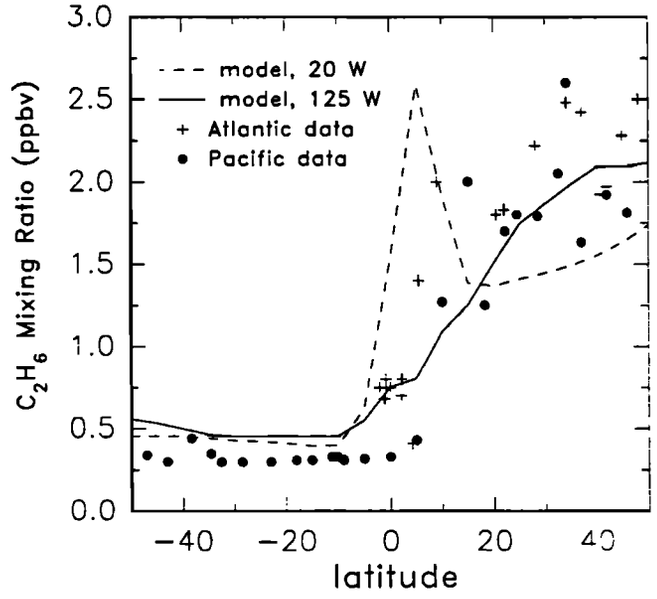

Figure 13. Observed and calculated surface mixing ratio of ethane (ppbv) over the Atlantic (January, data from *Rudolph and Ehhalt* [1981]) and over the Pacific (December, data from *Singh et al.* [1988]).

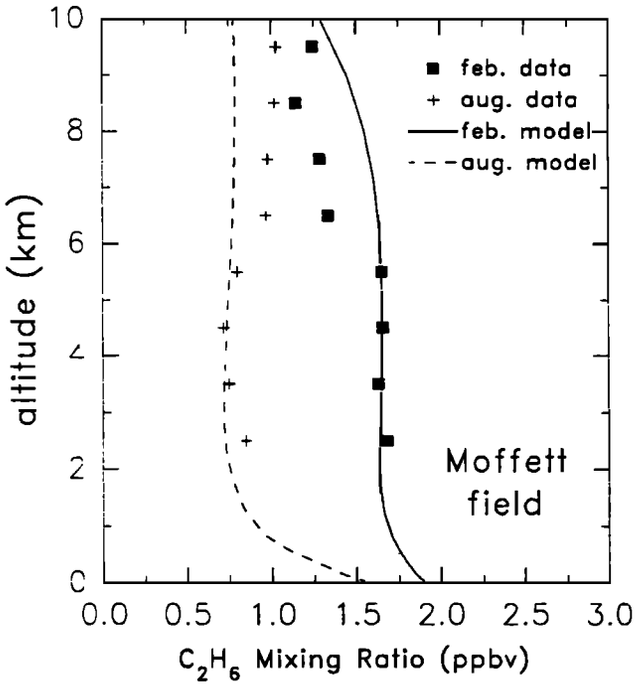

Figure 14. Observed and calculated vertical profile of ethane mixing ratio (ppbv) at Moffett Field (California coast). Data are from *Singh et al.* [1988].

and 355 Tg/yr, respectively). The biomass burning source estimate, however, is subject to large uncertainties. For example, with the CO/CO_2 emission ratios reported in a recent study by *Hao and Ward* [1993] (as opposed to the constant 10% ratio assumed in this study), the biomass burning emissions would be reduced to 207 Tg(CO)/yr in the southern hemisphere (603 Tg(CO)/yr globally). Taking the CO-OH feedback into account, it can be estimated that the CO mixing ratio would be lowered by probably about 15% on an annual basis and by a much larger amount during the dry season. In this case, the surface concentration would be substantially closer to the observations at Cape Point and several other stations, except Cuiaba, which is mostly influenced by savanna burning. Further studies are needed to better constrain the estimates of the biomass burning emissions.

Table 8 presents the global budget of CO derived by the model. The surface CO emissions represent 62% of its total source. The photochemical production due to the degradation of methane and other hydrocarbons accounts for the remainder (38% or 883 Tg CO/yr). This estimate of the photochemical production is somewhat lower than in previous studies [e.g., *Logan et al.*, 1981; *Hough*, 1991]. This is partly due to our higher estimate of the methane chemical lifetime (leading to a smaller production of CO from CH_4 oxidation), our smaller source of biogenic hydrocarbons, and probably a more efficient removal of organic peroxides and other oxygenated hydrocarbons by deposition or aerosol reaction. A large fraction of CO is released or produced in the tropics: 60% of the emissions and 71% of the photochemical production occur between 30°S and 30°N. Destruction by reaction with OH is the major sink (90%) of CO and is also primarily tropical (70%). These numbers agree with previous modeling studies [e.g., *Law and Pyle*, 1993b].

3.3. Nitrogen Compounds

The importance of nitrogen compounds is a consequence of their role in the budget of species like ozone and the OH radical. Odd nitrogen is released in the form of NO, mostly as a result of combustion processes (biomass burning, fossil fuel combustion, lightning) and soil microbial activity. After its emission at the surface NO is rapidly converted by photochemical processes into other forms of nitrogen oxides (NO_2, NO_3, N_2O_5) as well as nitric acid (HNO_3) and organic nitrates, including peroxyacetyl nitrate or PAN. Odd nitrogen is removed from the atmosphere by surface deposition mechanisms. For the sake of illustration we show in Figure 18 the zonally averaged mixing ratio of NO_x (defined as $NO + NO_2 + HNO_4 + NO_3 + 2N_2O_5$) in June and in Figure 19 the global distribution of NO_x near the surface. In both cases a logarithmic scale is used, so that the large spatial variations encountered in the atmosphere can be properly represented.

Figure 18 shows that the mixing ratio of NO_x decreases by approximately 2 orders of magnitude between the lower stratosphere and the middle troposphere. Typical mixing ratios are 10–100 pptv between 1 and 8 km altitude. The average concentration of NO_x at midlatitudes in the free troposphere is at least 5 times larger in the northern hemisphere than in the southern hemisphere. The same comparison for the boundary layer suggests a ratio of 50–100 between the two hemispheres.

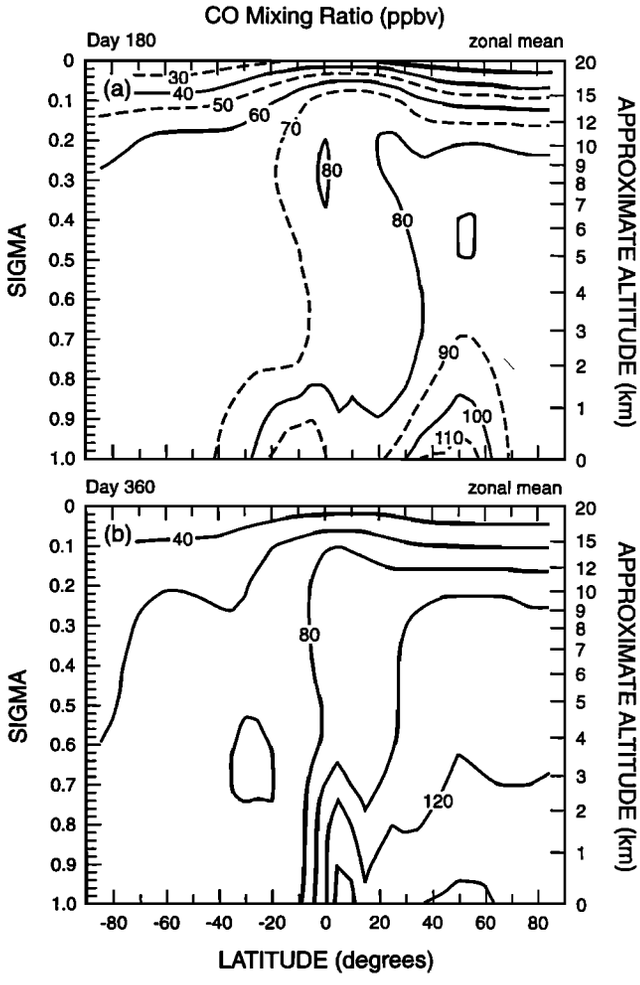

Figure 15. Zonally averaged distribution of the carbon monoxide mixing ratio (ppbv) in (a) June and (b) December.

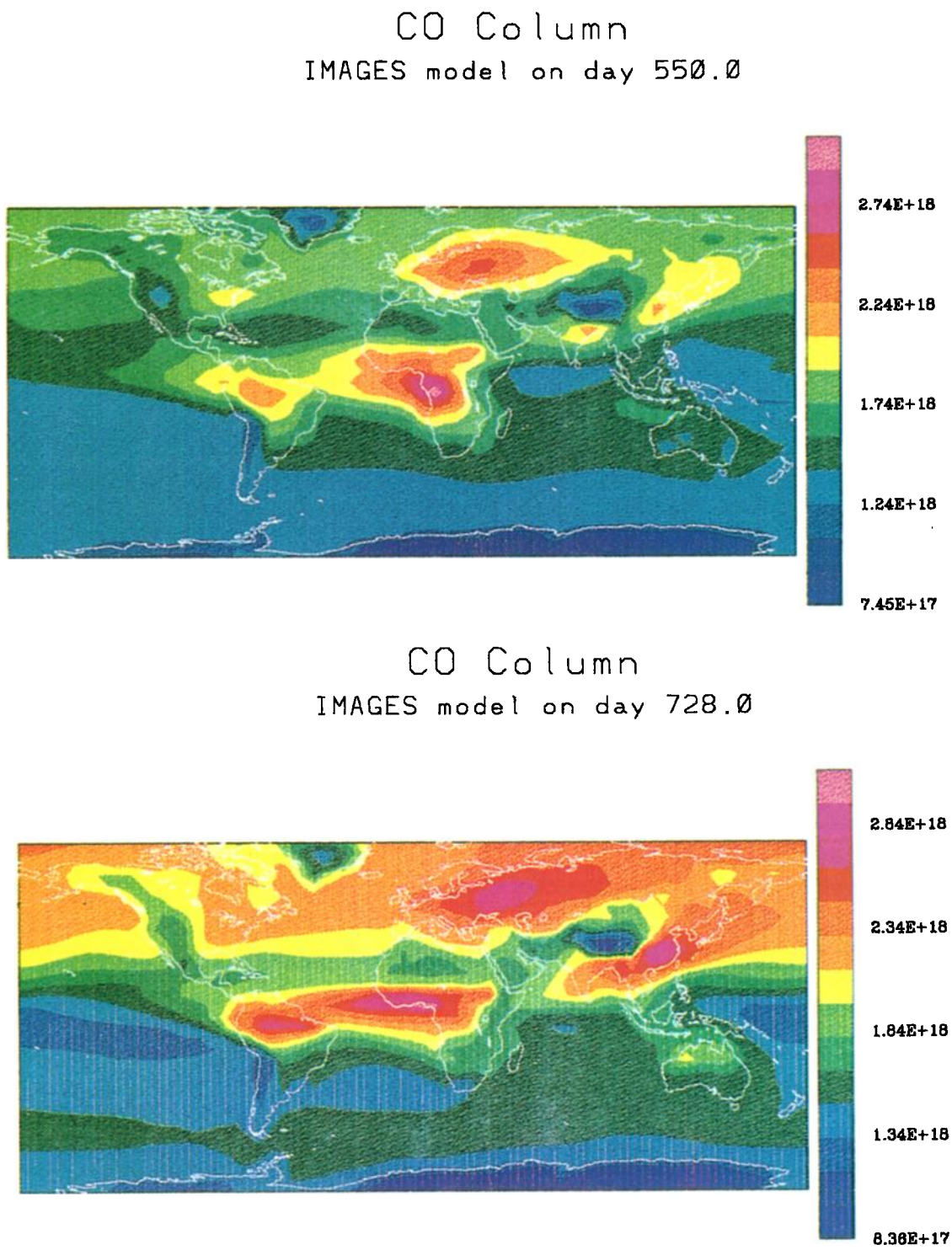

Figure 16. Distribution of the carbon monoxide column abundance (centimeter^{-2}) in (a) June and in (b) December.

The contribution of industrialized regions to the NO_x emissions is responsible for the calculated surface mixing ratio at 50°N, whose zonally averaged mixing ratio reaches 0.5 ppbv in summer and 1 ppbv in winter.

The spatial distribution of the NO_x mixing ratio near the surface (Figure 19) is characterized by variations of several orders of magnitude. Values as high as 1–3 ppbv are calculated over Europe and the eastern United States, while over the equatorial Pacific Ocean, the mixing ratio can drop below 1 pptv. The strong spatial variability in NO_x is a direct consequence of its short chemical lifetime (of the order of 1 day) and its localized emission sources.

Nitric oxide has been measured at numerous locations and for different conditions, so that a comprehensive analysis of the date and their comparison with model calculations cannot be presented in this general paper. To illustrate the performance of the model, we select measurements made during the STRATOZ III campaign (Figure 20) as well as observations made over the

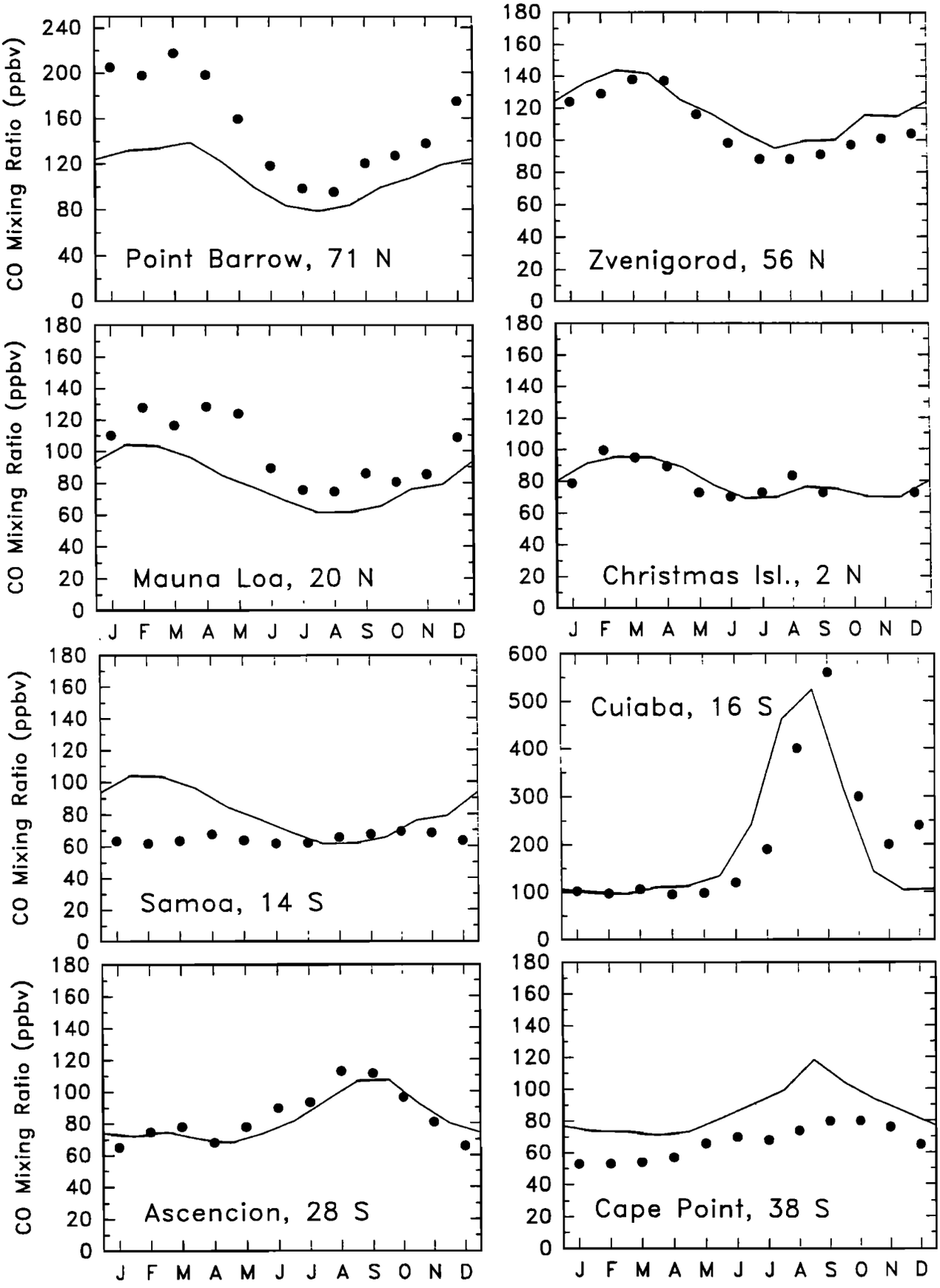

Figure 17. Observed and calculated surface mixing ratio of CO (ppbv) at several sites. The Zvenigorod data [*Dvoryashina et al.*, 1984] are derived from column measurements and compared with the model results at 500 mb. Cuiaba data, *Kirchhoff et al.* [1989]; Cape Point, *Seiler et al.* [1984]; other stations, see reference in the work of *Novelli et al.* [1992].

Table 8. Global Annual Budget of CO, in Teragrams Per Year

Source/Sink Type	Magnitude
Sources	
surface emissions	1428
CH_4 oxidation	543
NMHC oxidation	340
total	2311
Sinks	
chemical loss	2060
dry deposition	254
total	2314
Atmospheric burden, Tg	377
Residence time, days	60

Pacific Ocean (Figure 21) and near Manaus in Amazonia (Figure 22). Only those measurements made for zenith angles representative of daytime averages were selected for comparison. In general, the agreement between model and observations is good. However, although the observations exhibit large variability, the modeled NO concentration is generally too low in the upper troposphere (9–12 km), suggesting perhaps that the transport of NO_x-rich air from the stratosphere is not well represented. The under prediction at low altitudes at Bogota reflects local pollution in the planetary boundary layer. The good agreement found at Manaus (Amazonia) suggests that photochemistry and the soil emissions are well represented in the model.

The comparison of HNO_3 profiles (Figure 23) shows that although the agreement between model and observation is good over the United States, the nitric acid mixing ratio predicted over the southern Pacific Ocean is at least an order of magnitude smaller than the observed values. This discrepancy cannot easily be explained only as a misrepresentation of the HNO_3 sink processes (washout and dry deposition), even if the washout of soluble gases is rather crudely represented in the model. The production of NO by lightning might also be too low, and its specified geographical distribution might be incorrect. The measurements of *Huebert and Lazrus* [1980] might also include other nitrogen compounds, such as organic nitrates, and hence overestimate the real concentration of HNO_3. Good agreement is found (Figure 24) between observed and calculated HNO_3 over a continental (Niwot Ridge) and an oceanic site (Bermuda).

In the case of peroxxyacetyl nitrate (PAN) (Figure 25) the model seems to reproduce correctly the concentrations measured in the free troposphere over Boulder but overestimates significantly the concentrations observed in summer at Moffett Field. It should be stressed, however, that the lifetime and hence the concentration of PAN are extremely sensitive to the ambient temperature, so that the variability in the measurements should be high and the comparison with model values is not straightforward.

The recent Mauna Loa Observatory Photochemical Experiment (MLOPEX II) conducted in Hawaii from September 1991 to August 1992 has provided a year long data set of nitrogen compounds in a relatively pristine environment. Figure 26 compares averaged measurements of HNO_3, NO_x, and PAN made during the four intensives of the campaign with values calculated in the model at two neighboring grid points located at approximately 3 km altitude. The model clearly underestimates the concentrations of NO_x and HNO_3, although the values for PAN, including the seasonal variation are in fairly good agreement with the observation. Thus as in the model simulations of *Levy and Moxim* [1989b] and *Penner et al.* [1991], the level of NO_y predicted by IMAGES in the vicinity of Hawaii is significantly lower than the observed value. In addition, the concentration ratio between HNO_3 and NO_x is approximately a factor 3 lower in the model than in the data. This result should to be contrasted with calculations made by *Liu et al.* [1992] after the MLOPEX I campaign (May 1988). Based on a chemical box model in which heterogeneous removal of soluble species is neglected, the HNO_3/NO_x ratio at steady state was estimated to be of the order of 19, i.e., a factor 5–6 higher than suggested by the observations at the Mauna Loa site (3.4 km altitude; see *Atlas et al.* [1992]). The ratio was reduced when washout processes were included in the 0-dimensional model. A more accurate parameterization of heterogeneous processes in IMAGES could bring the calculated HNO_3/NO_x ratios closer to the observation.

As stated in Table 9, the surface emission of nitrogen oxides, as estimated in the present study, represents 33 Tg/yr, among which 83% occurs in the northern hemisphere (36% in the tropics). The surface emission and the airborne source of NO_x (primarily lightning) total to about 41 Tg N/yr. This source is balanced by dry deposition of NO_2 (4 Tg N/yr) and HNO_3 (10 Tg N/yr), as well as by washout of nitric acid (18 Tg N/yr), and (wet and dry) deposition of organic nitrates (9 Tg N/yr). Wet deposition of nitric acid and organic nitrates over North America accounts for 1.31 and 0.75 Tg(N)/yr, respectively, resulting in a total of 2.06 Tg(N)/yr for nitrate wet deposition over North America, in agreement with the previous estimate of *Logan* [1983]. Nitrate deposition is largest in the eastern United States, with values reaching approximately 20–25 kgN/km^2/month in winter and more than 30 kgN/km^2/month in summer (in southeastern United States), in agreement with the observations (cf. Figures 21–22 in the work of *Penner et al.* [1991]). The maximum value observed in winter over the Great Lakes is not found in the model results. Deposition of organic nitrates (ONIT) is only a small sink of odd nitrogen at midlatitudes during the winter but becomes almost the largest NO_y sink during the summer, when biogenic hydrocarbons are abundant.

3.4. Hydrogen Compounds

The oxidizing capacity of the atmosphere is, to a large extent, governed by the abundance of the hydroxyl radical (OH). The

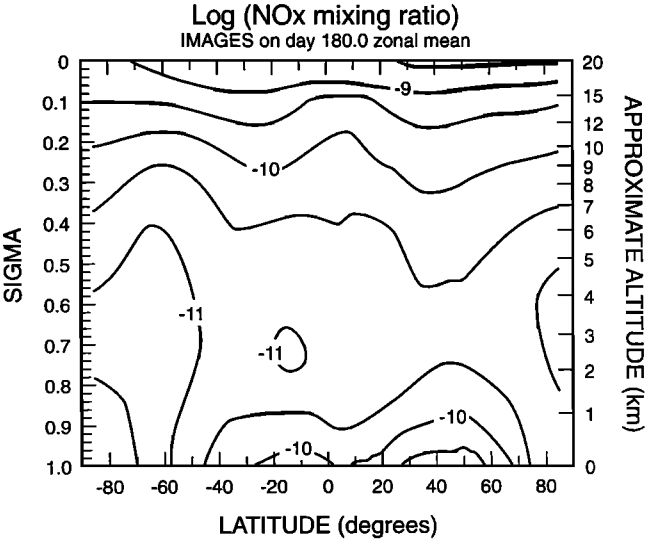

Figure 18. Zonally averaged distribution of the nitrogen oxides mixing ratio (expressed in decimal logarithm) in June.

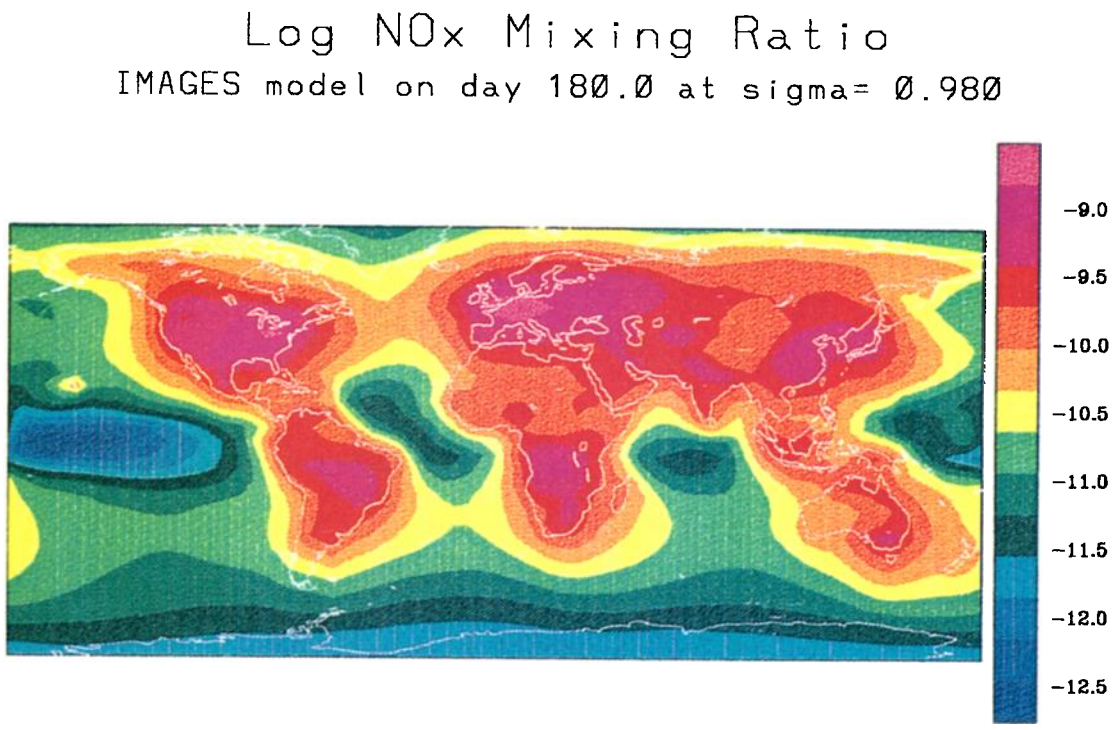

Figure 19. Distribution of the nitrogen oxides mixing ratio (expressed in decimal logarithm) at $\sigma = 0.98$ in June.

concentration of OH is directly linked to that of HO_2 through multiple conversion mechanisms. The density of HO_2 in the troposphere is typically a factor of 100 larger than that of OH. Radicals such as OH and HO_2 are also to strong diurnal variations, because their formation requires the presence of sunlight. OH is most abundant in the lower and midtroposphere, in the latitude bands of maximum solar insolation (Figure 27). The decrease of the OH density with altitude between the boundary layer and the tropopause is primarily related to the water vapor profile. The minimum concentration predicted around the equator in the planetary boundary layer and in the upper troposphere is due to the low O_3 mixing ratio and the abundance of the biogenic NMHC and their oxidation products in these regions. OH increases across the tropopause as CO and NMHC concentrations decrease, and O_3 and NO densities increase. The global chemical lifetimes of long-lived species controlled by OH are found to be in general agreement with other estimations (11 years for CH_4, 6.3 years for CH_3CCl_3).

3.5. Ozone

Tropospheric ozone is photochemically produced in the presence of light, nitrogen oxides, and peroxy radicals (HO_2 and the organic RO_2). The key reactions in this process are the HO_2 + NO (or RO_2 + NO) reaction followed by the photolysis of NO_2. The hydroperoxy radical (HO_2), however, also destroys ozone, so that the concentrations of NO and RO_2 are the primary factors determining photochemical ozone formation. Additional ozone is injected from the stratosphere, mostly at midlatitudes. The sinks of tropospheric ozone are provided by surface deposition and chemical destruction. Figure 28 shows the zonally averaged mixing ratio (logarithmic scale) of ozone as a function of latitude and the vertical coordinate σ. The effect of ozone-rich stratospheric air intrusion in the upper troposphere is clearly seen, with maximum values found at midlatitudes. The comparison of Figure 28 with the vertical component of the wind (not shown) suggests a close relationship between ozone and the dynamics in the middle and upper troposphere. Upward motions in the equatorial region transports ozone-poor air from the lower troposphere to higher altitudes. The lowest mixing ratios (< 15 ppbv) are found in the equatorial boundary layer, where O_x (defined as $O_3 + O + O(^1D)$) is depressed by the deposition of ozone on the tropical forest and the $O(^1D) + H_2O$ reaction. The highest values of tropospheric mixing ratios (in the zonally averaged sense) are found at midlatitudes in the northern hemisphere, where stratospheric intrusion and photochemical formation are most dominant.

Figures 29a–29b show the mixing ratio of ozone near the surface in June and December, respectively. The effect of intense photochemical production over the industrialized regions of the northern hemisphere are clearly seen in June. Mixing ratios of 35–50 ppbv are predicted by the model over the United States and Europe in summer. In winter the largest photochemical sources of ozone are located in the tropics. Wintertime surface ozone at midlatitudes seems to be overpredicted by the model. As noted above, the minimum in ozone concentration along the equator is related to intense surface deposition on the canopy and chemical destruction through the $O(^1D) + H_2O$ reaction. These destruction processes are counteracted in some areas by photochemical production associated with biomass burning during the dry season (southern tropical Africa in June, northern tropical Africa in December). An important feature produced by the model is the relatively high ozone mixing ratios downwind of the source regions, caused by the transport of ozone and its precursors from industrialized regions. In regions remote from pollution sources, such as the tropical Pacific and Indian Oceans, ozone can drop to very low values, sometimes below 5 ppbv.

To validate the ozone concentrations derived by the model, we have first considered ozone measurements made near the ground at several sites. As can be seen in Figure 30, the model

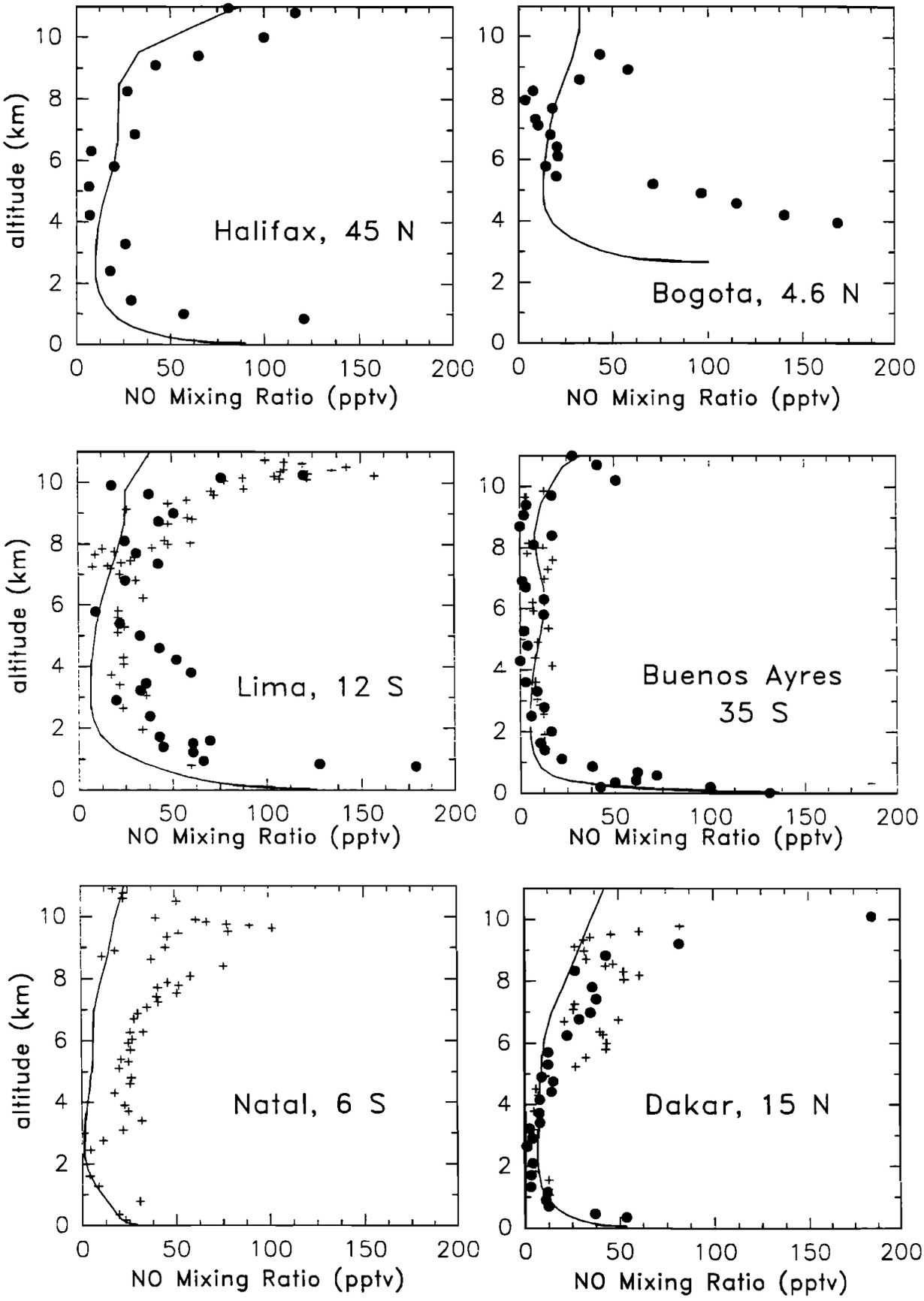

Figure 20. Observed and calculated mixing ratio of NO (pptv) as a function of altitude at several sites. Model results are June daytime averages. The data are from aircraft measurements during the STRATOZ III campaign (June 1984) [*Drummond et al.*, 1988]. Circles, descending flights; pluses, ascending flights.

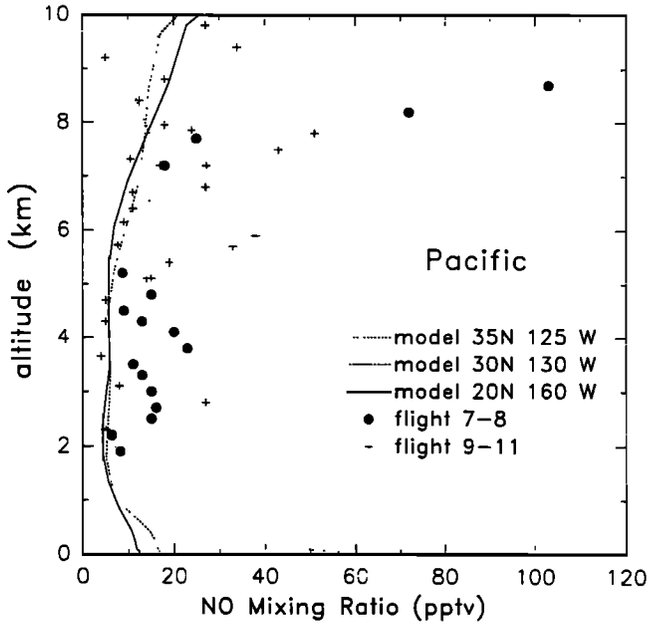

Figure 21. Observed and calculated mixing ratio of NO (pptv) as a function of altitude over the Pacific Ocean in November. Model results are daytime averages for three locations. The data are from the aircraft measurements of *Davis et al.* [1987].

somewhat overestimates the mixing ratio measured in winter at the polluted continental site of Hohenpeissenberg. On the other hand, the calculated O_3 concentrations are too low at Samoa Island, but other surface measurements in the Pacific (see below) provide much lower values than those observed on this particular island. The surface mixing ratio at the south pole is significantly underestimated by the model; as photochemistry is slow in the polar region, this discrepancy must be attributed to transport.

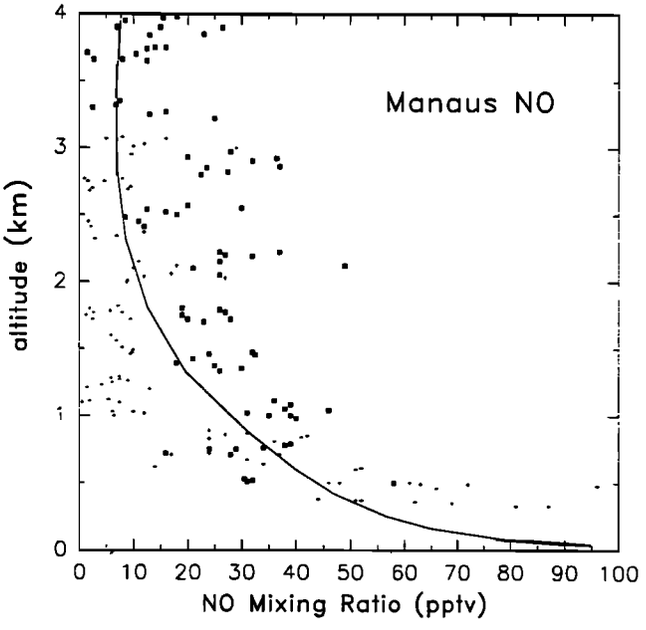

Figure 22. Observed and calculated mixing ratio of NO (pptv) as a function of altitude at Manaus (Amazonia) in June. Model results are daytime averages. The data are taken from *Torres and Buchan* [1988]. Crosses, early morning; squares, later in the day.

Additional comparisons of surface ozone involve data gathered over the Pacific and Indian Oceans (Figure 31) and the Atlantic Ocean (Figure 32), respectively. The very low values (< 10 ppbv) observed in the equatorial Pacific are well reproduced by the model, as well as the equator-midlatitudes gradient. Note that the southern extremity of the Pacific profile of April 1988 corresponds to the Samoa Island. At this location the measured mixing ratio is well below 5 ppbv, while the data taken at the Samoa station in April suggests values of about 10 ppbv. The model predicts about 7 ppbv. The most important

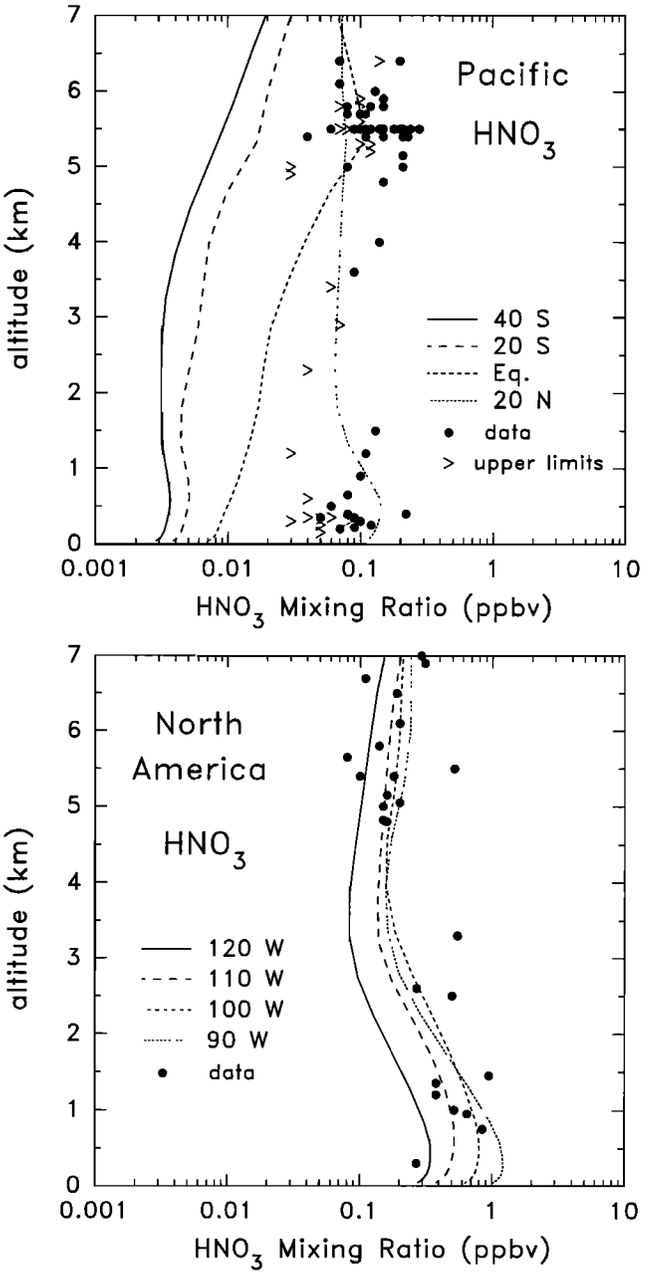

Figure 23. Observed and calculated HNO_3 mixing ratio (ppbv) as a function of altitude over the Pacific Ocean (upper panel) and western North America (lower panel). The data are August–September and May–June measurements from *Huebert and Lazrus* [1980]. The model results (averaged over the same period of time) are shown for September at 125°W (Pacific profiles) and 40°N (North America profiles).

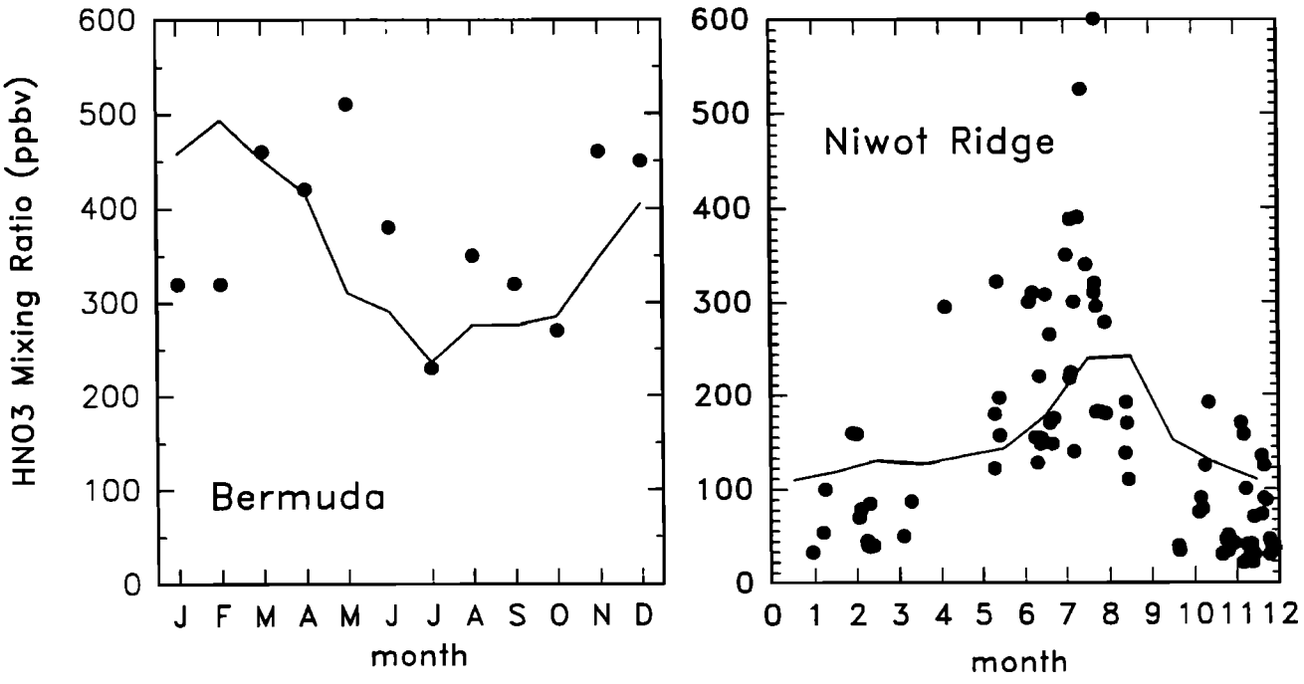

Figure 24. Observed and calculated surface mixing ratio of HNO_3 at Bermuda and Niwot Ridge (Colorado). Bermuda data, reference in *Khasibatla et al.* [1993]; Niwot Ridge data, *Parrish et al.* [1986].

discrepancy between the calculated and the observed meridional distributions of surface ozone in the Atlantic (Figure 32) is found at midlatitudes in winter (in both hemispheres) and, to a lesser extent, in spring, where the model provides concentrations that are larger than the observation. Note the higher values over the Atlantic compared with those reported for the Pacific. The data also show that midlatitude oceanic ozone is lower in summer (around 30 ppbv) than during the spring (40 ppbv), in contrast with the seasonal behavior observed over polluted areas.

Calculated and observed vertical profiles of ozone at several stations are shown in Figures 33–39. Note that the good agreement between model and observation in the uppermost level is a straightforward consequence of the prescribed boundary conditions in the upper levels of the model. The agreement in the

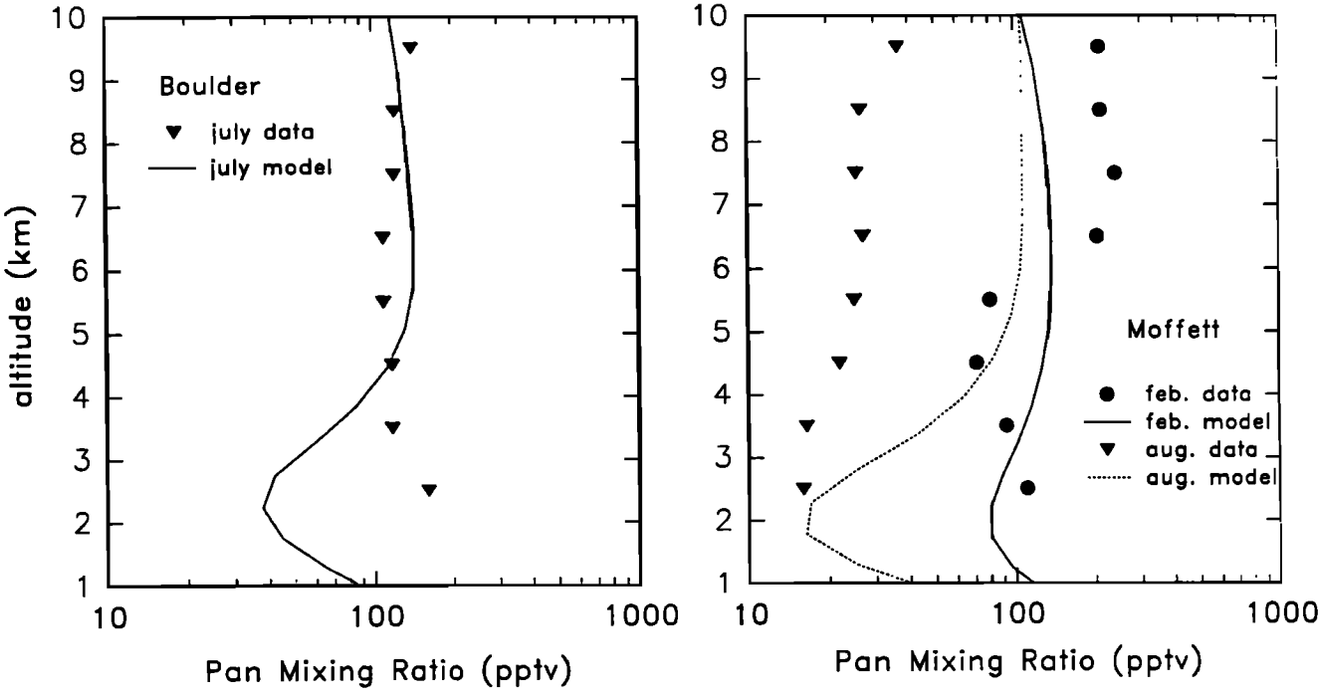

Figure 25. Observed and calculated vertical profile of PAN mixing ratio (pptv) at Boulder (Colorado) and Moffett Field (California coast). The data are taken from *Singh et al.* [1986].

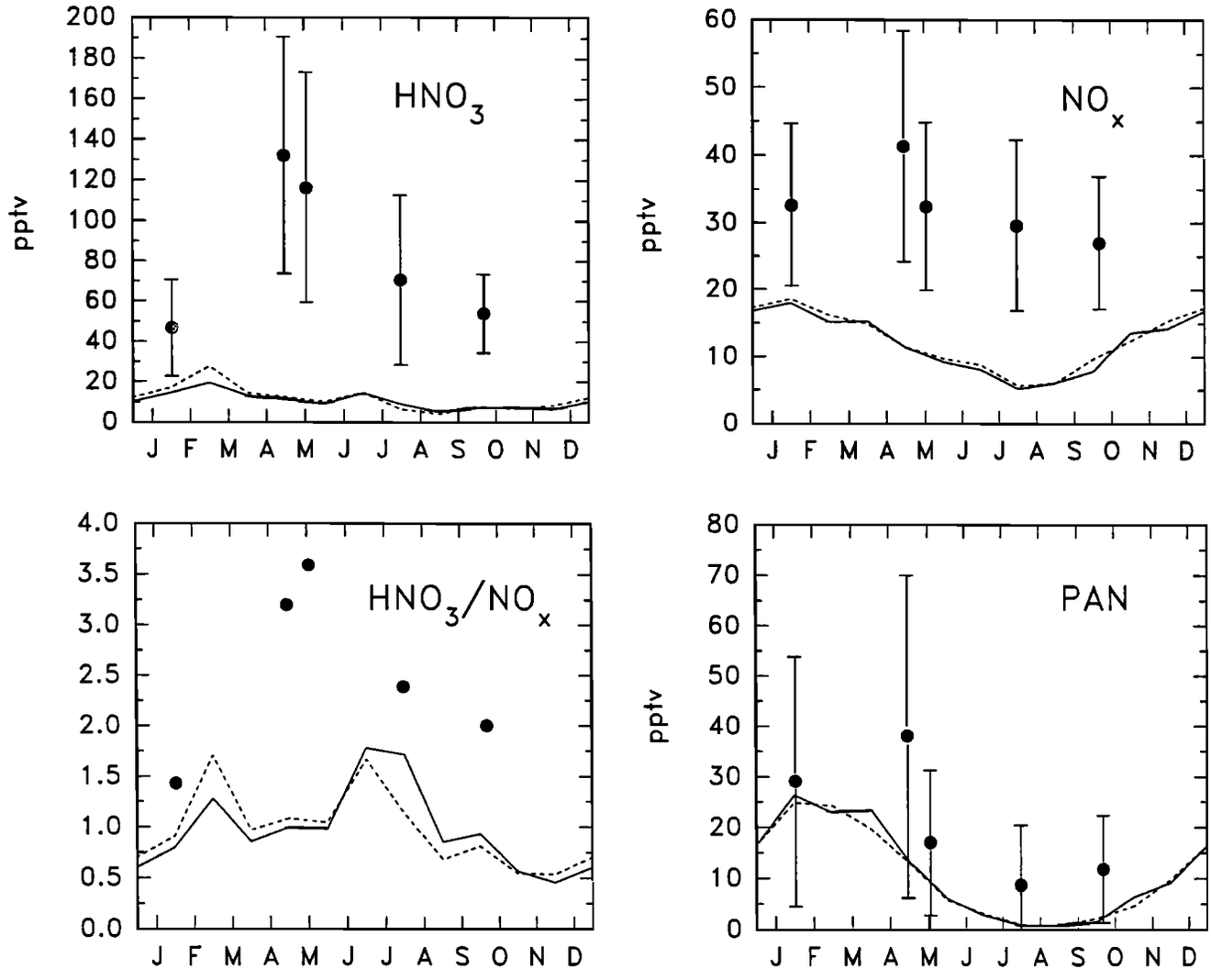

Figure 26. Seasonal evolution of the (a) HNO_3, (b) NO_x, and (d) PAN mixing ratio, as well as of the HNO_3/NO_x concentration ratio (c) at Mauna Loa (Hawaii) measured during MLOPEX II and calculated at 2 grid points of the model closest to the location of the observation site.

Table 9. Annual Budget of NO_t in the Model Domain, in Tg(N)/yr

Source/Sink Type	Magnitude
Sources	
surface emissions	32.9
lightning	8.0
aircraft	0.4
$N_2O + O(^1D)$	0.2
total	41.5
Sinks	
HNO_3 washout	18.0
HNO_3 dry deposition	10.0
ONIT deposition	8.3
NO_x dry deposition	4.1
PAN dry deposition	0.44
HNO_4 washout	0.37
HNO_3 to stratosphere	0.2
total	41.4
Burden, Tg(N)	2
Residence time, days	18

PANs = PAN + MPAN, $NO_t = NO_x + HNO_3 + ONIT + PANs$.

troposphere is generally very good. The model reproduces well the increase in the vertical gradient near the tropopause (at about 300 mbar in the high latitudes profiles, 200 mbar at midlatitudes, and around 100–150 mbar in the tropics). The midlatitude profiles (Boulder, Wallops Island, and New Zealand) show a very good agreement. As noted above, the Samoa mixing ratio is largely underestimated (Figure 36). Calculated ozone at Ducke forest (near Manaus, Amazonia) is slightly too low in the free troposphere in April (wet season), while the August (dry season) profile is similar to the measurements (Figure 37). In both seasons the vertical gradient in the lower troposphere is smaller than observed. At south pole (Figure 39), as indicated earlier, a notable discrepancy is found at low altitudes, where the ozone calculated in the model is significantly underestimated.

The relationship between ozone and NO_y concentrations is often used to diagnose observations made at near the surface [e.g., *Hubler et al.*, 1992a], in the free troposphere [*Hubler et al.*, 1992b], and in the stratosphere [*Proffitt et al.*, 1989; *Kondo et al.*, 1990; *Murphy et al.*, 1993; *Weinheimer et al.*, 1993]. Figure 40 shows a diagram of ozone mixing ratios calculated at each grid point of the model in the free troposphere (525-mbar to 200-mbar layer) of the northern hemisphere in summer as a function of the

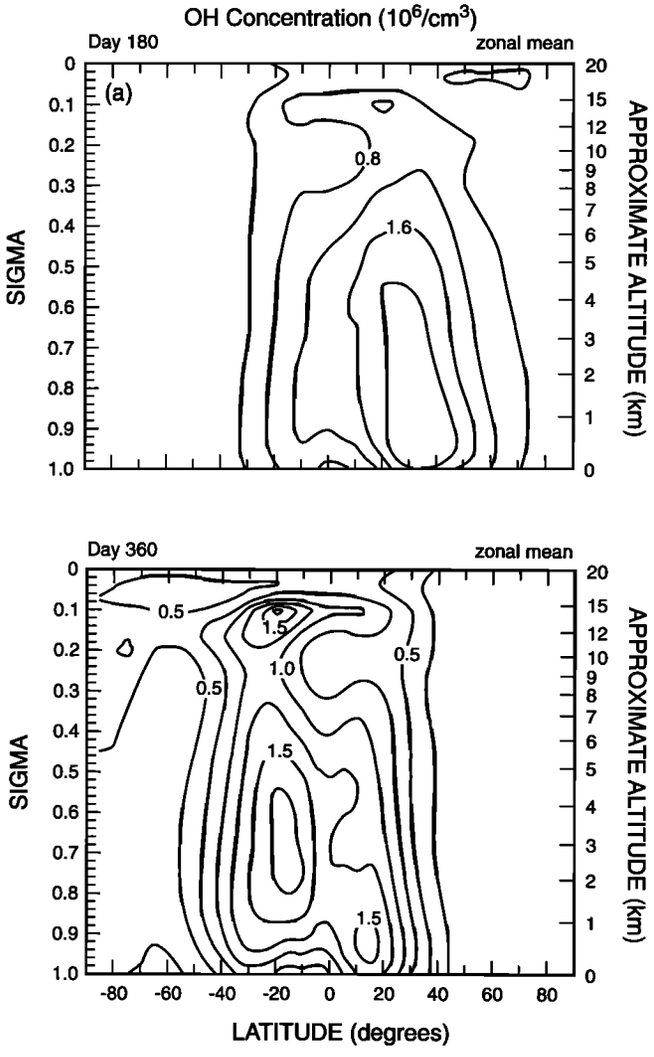

Figure 27. Zonally averaged distribution of the OH number density (10^6 molecule/cm^3) in (a) December and in (b) June.

(NO_y-NO_x) mixing ratio at these grid points. The difference between the NO_y and NO_x concentrations in an air parcel, which represents the abundance of oxidized reservoir components (mostly HNO_3, PAN, and to a lesser extent organic nitrates and particulate nitrates) is a measure of the "photochemical age" of the air parcel. In the free troposphere the concentration of NO_x is generally smaller than that of NO_y, so that a scattergram representing ozone versus NO_y would be very similar. The observed relationship between O_3 and NO_y-NO_x has been used to to derive the net number of ozone molecules produced per molecule of NO_x consumed in active photochemical environments [*Trainer et al.*, 1993; *Chin et al.*,1994]. What is remarkable in the scattergram shown in Figure 40 is that in spite of the large spatial and temporal variations in the sources and sinks of ozone and nitrogen oxides as well as in the different transport processes involved, the correlation is approximately the same over the entire northern hemisphere, implying perhaps the existence for ozone of a "global photochemical relationship" between ozone and NO_y (or of its reservoir components). Another explanation favoring the strong association between ozone and NO_y in the free troposphere is provided by the mixing of stratospheric air with free tropospheric air, but this process is probably negligible in regions where strong convective activity takes place. Note that the NO_y/O_3 concentration ratio derived by the model (at high ozone levels) ranges from approximately 0.006 to 0.016 and is in good agreement with the values reported by *Ridley et al.* [1994] in the free troposphere over New Mexico during the monsoon season (0.004–0.02); it is somewhat higher than the ratios observed by *Kondo et al.* [1990] and *Murphy et al.* [1993] in the lower stratosphere (0.003–0.006). Clear correlations between ozone and carbon monoxide (not shown) are also derived by the model.

It should be emphasized again that IMAGES is intended to provide mean distributions of trace constituents, rather than high-frequency signals. The real atmosphere is affected by rapidly varying meteorological patterns which produce large and rapid fluctuations in the concentration of ozone. The global budget of ozone (Table 10), however, is not expected to be very sensitive to these short-term fluctuations. Based on the model results, the stratospheric injection (550 Tg/yr) of ozone is approximately equal to its net photochemical production (550 Tg/yr). These two processes are balanced by the deposition of ozone at the surface. The global lifetime of tropospheric ozone (averaged over the model domain and calculated without considering null cycles, such as the photodissociation followed by ozone recombination, and the O_3 + NO reaction followed by NO_2 photolysis and ozone recombination) is of the order of 3 months. The geographical regions contributing to a net (vertically integrated) photochemical production or destruction of tropospheric ozone are shown in Figure 41 for the month of July. Overall, ozone is produced photochemically over the continents, especially in regions where combustion of fossil fuel or biomass is large, and is transported over the oceans where a weak photochemical destruction takes place.

It is now widely believed that the abundance of ozone in the troposphere has changed dramatically since the industrial revolution. To test this hypothesis, IMAGES has been run in a configuration where all anthropogenic sources have been ignored and the contribution of biomass burning reduced by a factor of 3

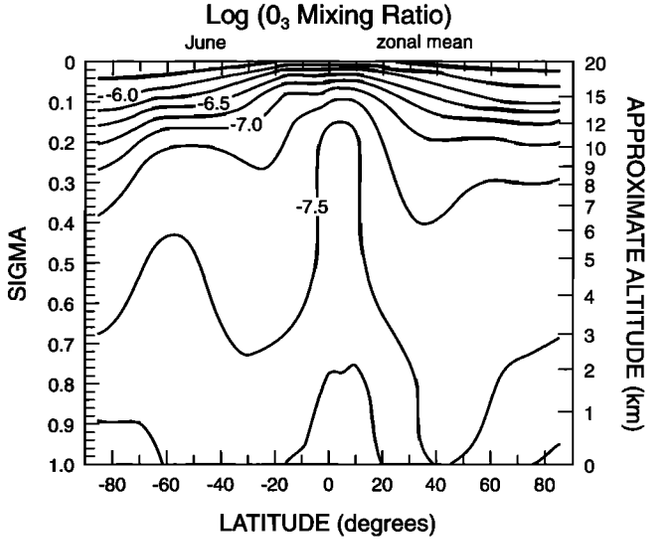

Figure 28. Zonally averaged distribution of the ozone mixing ratio (expressed in decimal logarithm) in June.

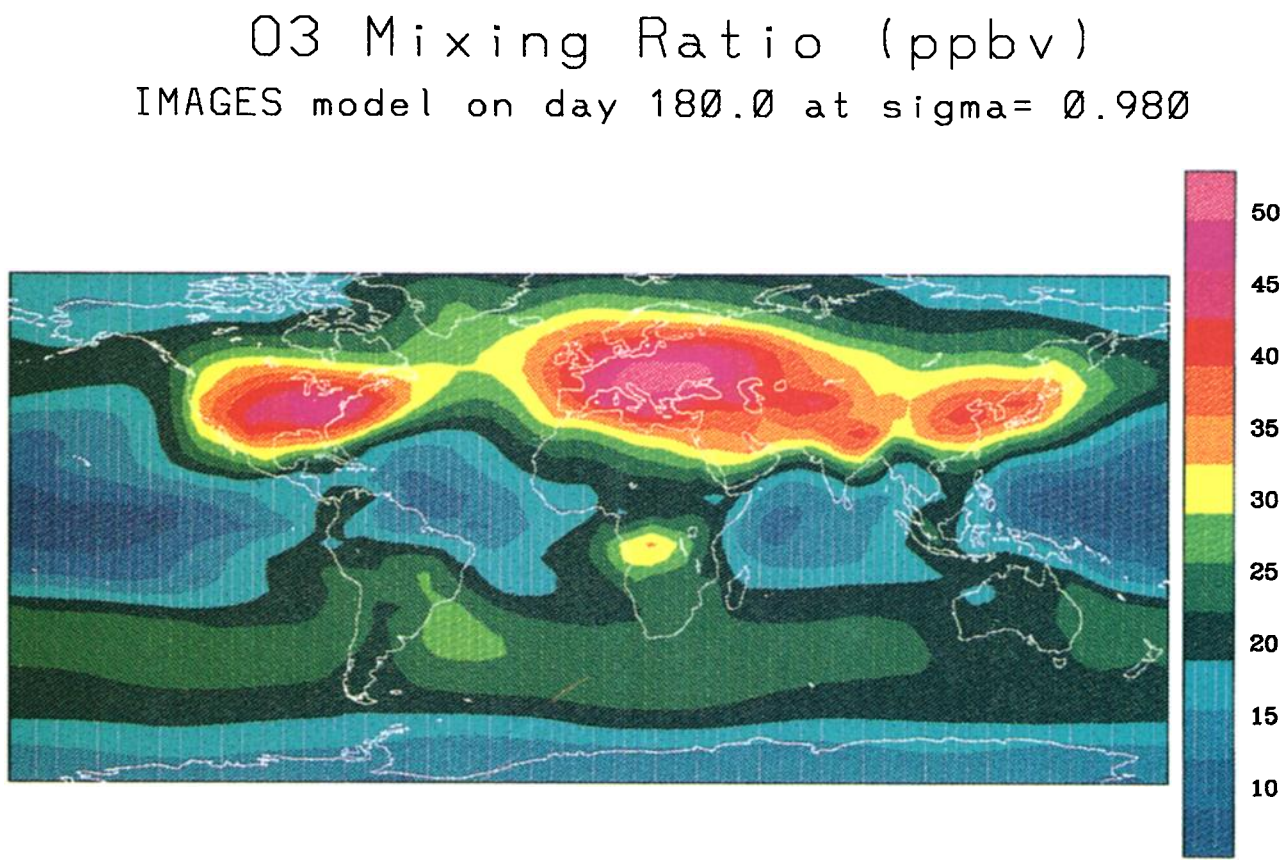

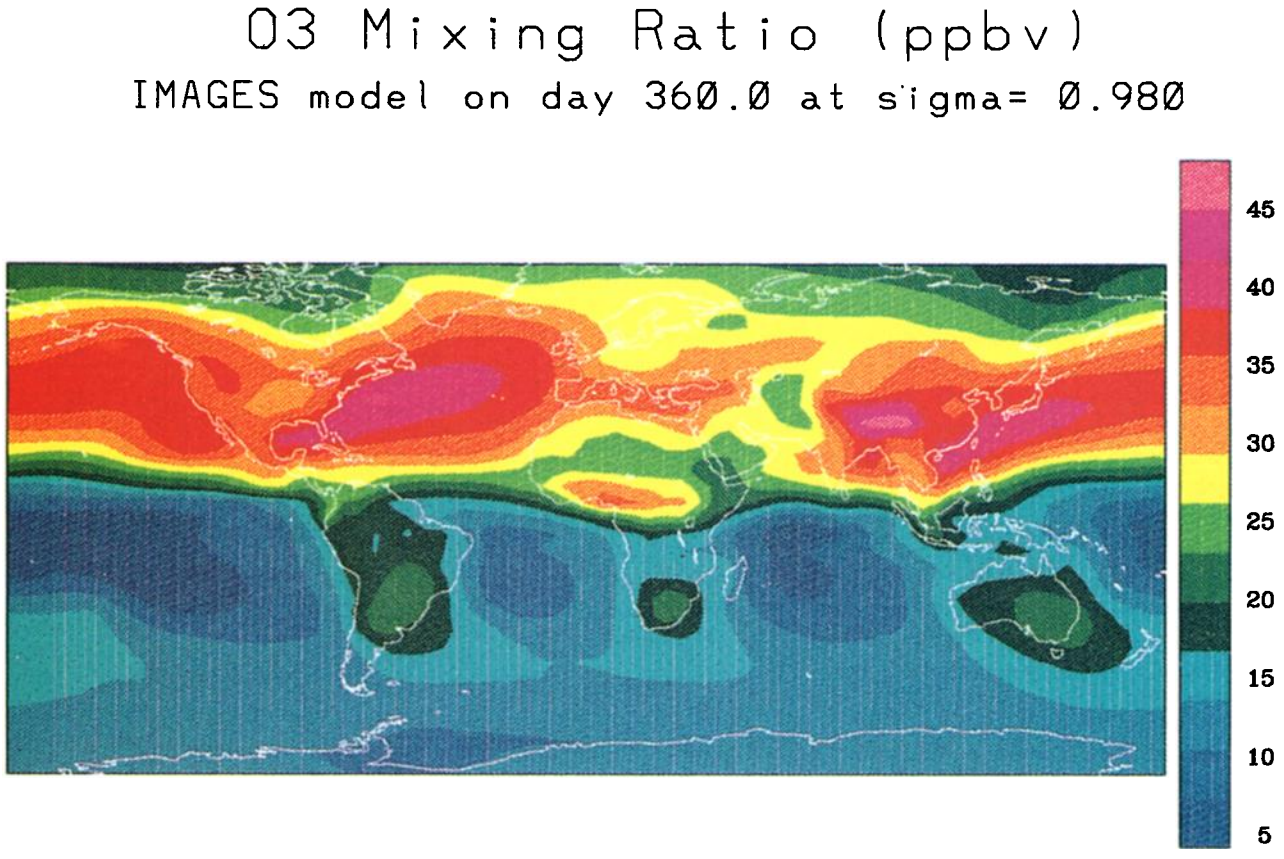

Figure 29. Distribution of the ozone mixing ratio (ppbv) at $\sigma = 0.98$ in (a) June and (b) in December.

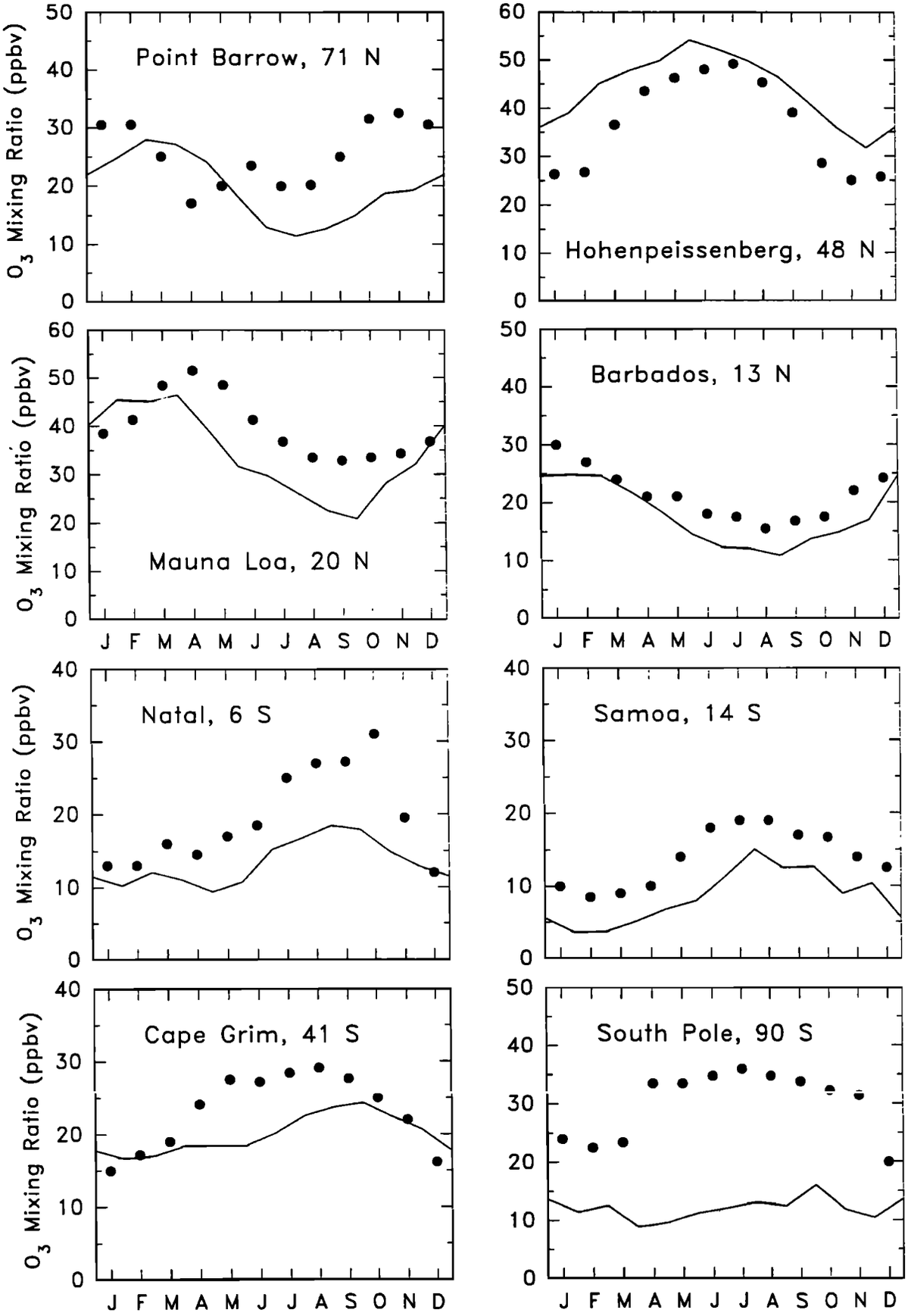

Figure 30. Observed and calculated surface O_3 mixing ratio (ppbv) at several sites. Point Barrow (Alaska), Mauna Loa (Hawaii), Samoa, south pole: data from *Oltmans and Komhyr* [1986]; Hohenpeissenberg (Germany): *Low et al.* [1990]; Barbados: *Oltmans and Levy* [1992]; Cape Grim (Tasmania): Galbally from *Logan and Kirchhoff* [1986].

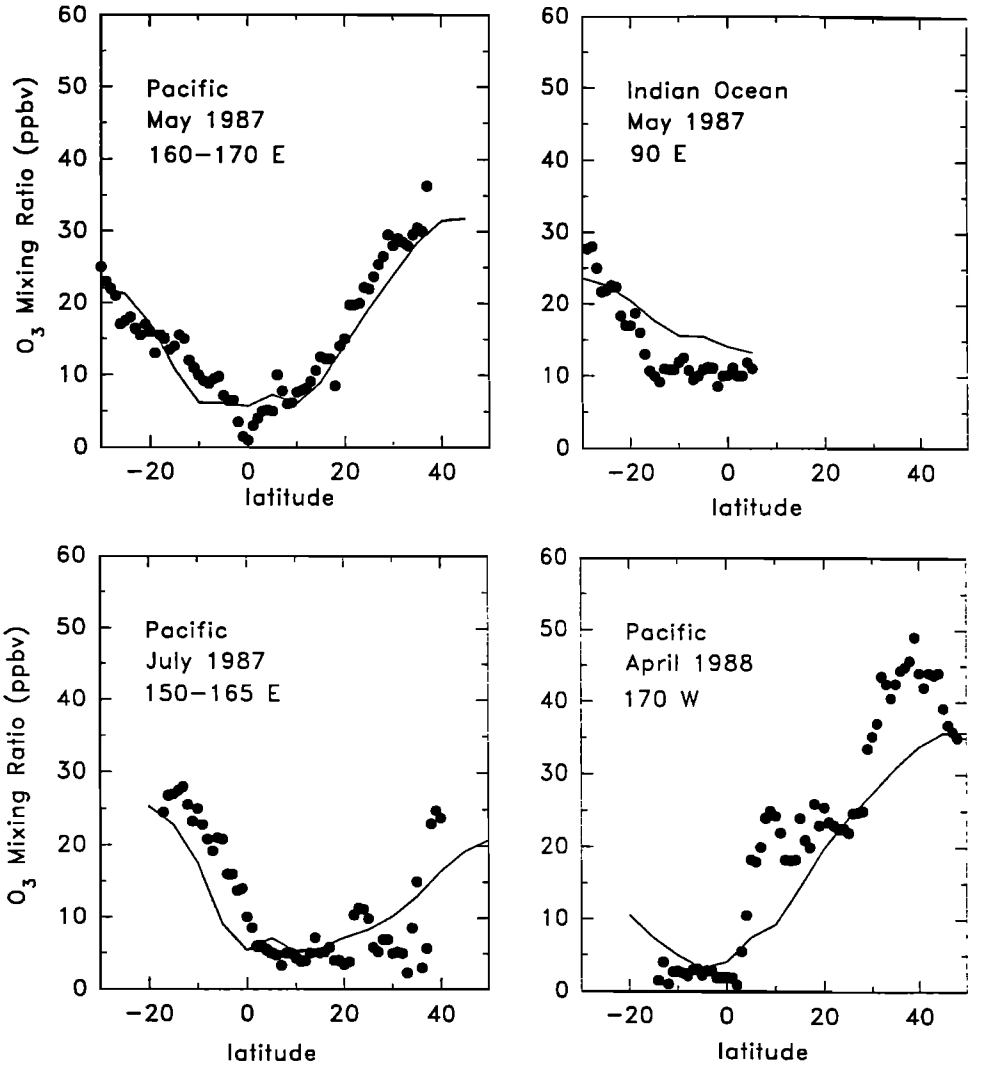

Figure 31. Observed and calculated surface mixing ratio of O_3 (ppbv) over the Pacific and Indian Oceans. The data are from cruise measurements during the Soviet American gases and aerosols (SAGA) and radiatively important trace species (RITS) campaigns [*Johnson et al.*, 1990].

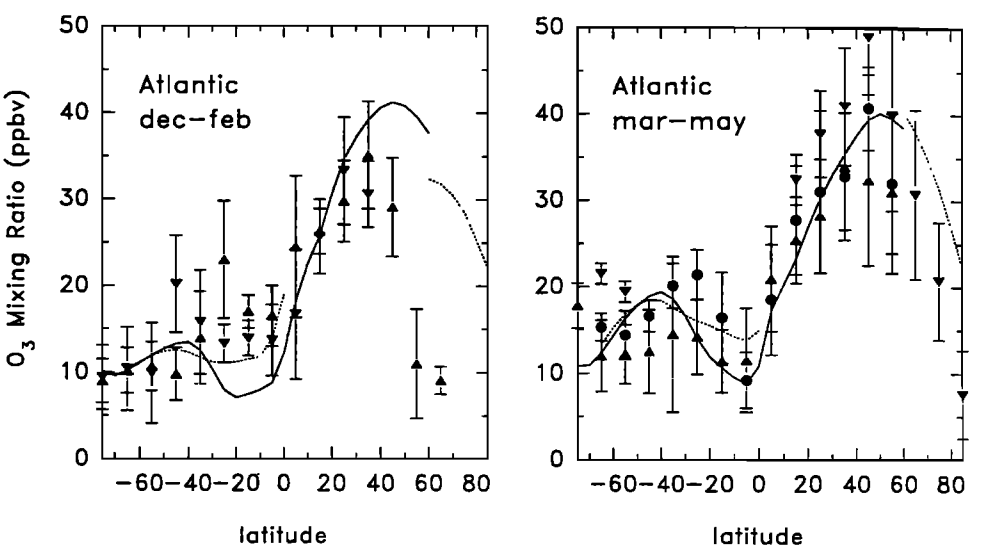

Figure 32. Observed and calculated surface mixing ratio of O_3 (ppbv) over the Atlantic Ocean. Solid line, model results at 25°W; dotted line, model results at 5°E. The data are averaged cruise measurements from *Winkler* [1988].

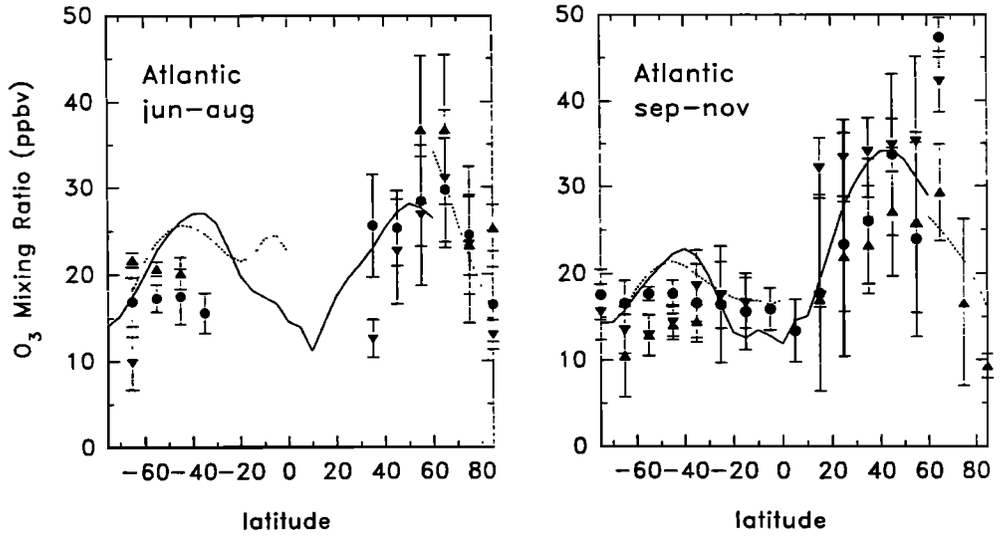

Figure 32. (continued)

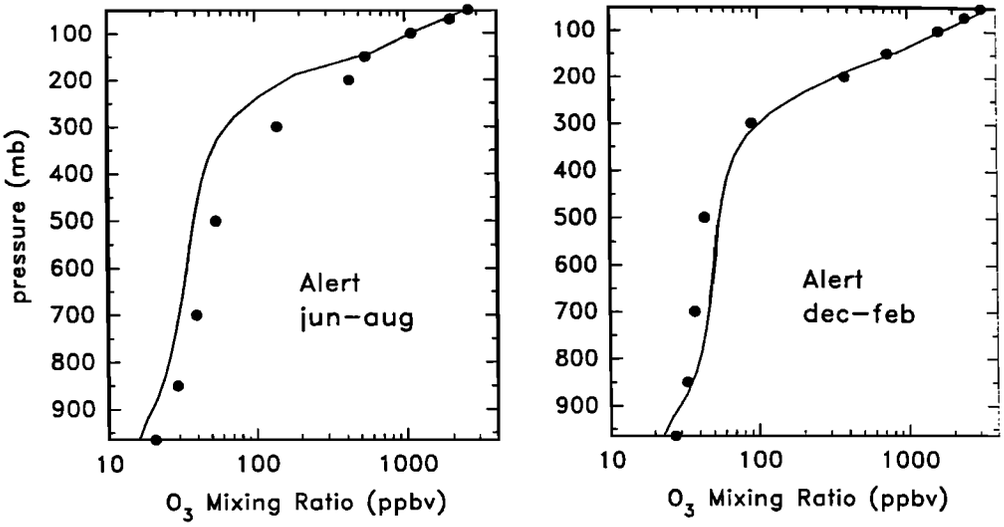

Figure 33. Observed and calculated vertical profiles of O_3 mixing ratio (ppbv) at Alert (Canada) for summer and winter. The data are from *Komhyr et al.* [1992].

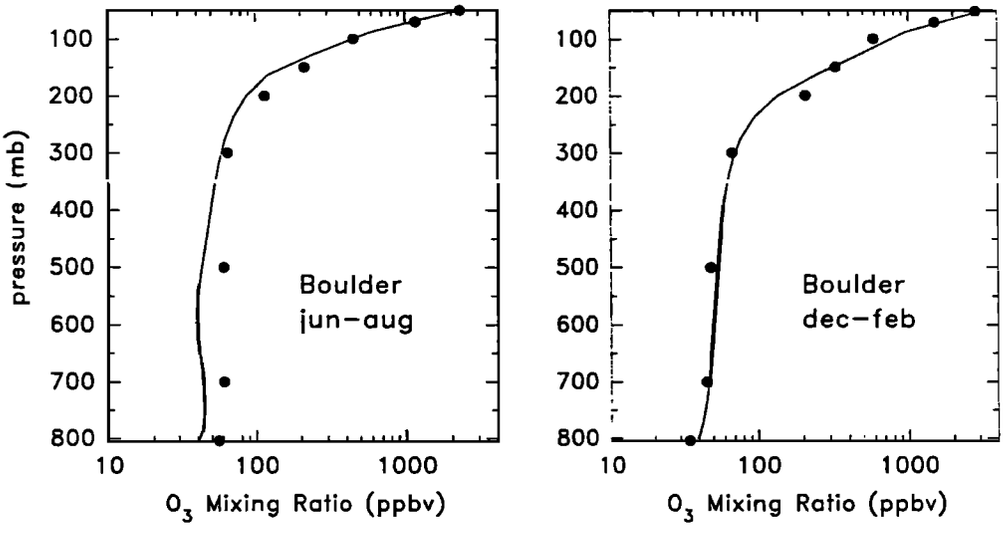

Figure 34. Observed and calculated vertical profiles of O_3 mixing ratio (ppbv) at Boulder (Colorado) for summer and winter. The data are from *Komhyr et al.* [1992].

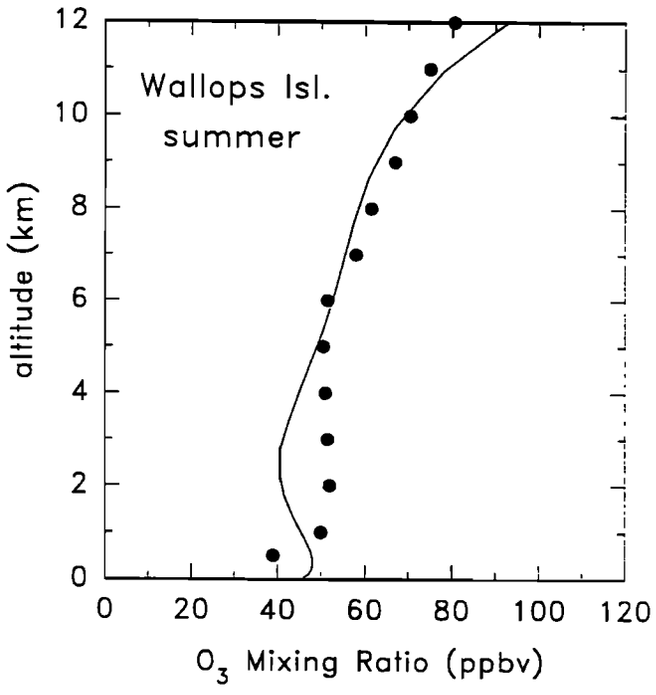

Figure 35. Observed and calculated vertical profile of O_3 mixing ratio (ppbv) at Wallops Island (Virginia) in summer (June–August). The data are from *Chatfield and Harrison* [1977].

in order to represent a smaller population density in tropical regions. The biogenic emissions, the dynamical variables, and the boundary conditions for O_3 were assumed to be identical to their present-day values. The averaged preindustrial surface mixing ratio of methane (650 ppbv) and nitrous oxide (285 ppbv) are taken from ice core measurements [*Stauffer et al.*, 1985; *Khalil and Rasmussen*, 1989]. The calculated concentrations of NO_x, CO, and hydrocarbons over continents are significantly reduced. The nitrogen oxides surface mixing ratio over continental areas was lower by a factor 5 on global average and by 1–2 orders of magnitude at midlatitudes. The atmospheric burden of CO is found to be 3 times lower than its present value. CO was more abundant in tropical regions (40–60 ppbv) than in the midlatitudes (30–40 ppbv), because the biogenic sources of CO (microbial production, oxidation of hydrocarbons) are mostly concentrated in the tropics. The resulting changes in the ozone abundance are substantial and most pronounced in the northern hemisphere, mostly during the summer. As shown by Figures 42a–42b, the change in the zonally averaged ozone concentration (referred to preindustrial conditions) reaches more than 100% in summer northern hemisphere. The predicted surface ozone changes over western Europe (a factor of 3 in summer) are consistent with the evolution of observed surface ozone concentrations in Europe since the end of the 19th century [*Volz and Kley*, 1988]. The seasonal cycle was less pronounced than it is today, because the NO_x levels were too low to allow a significant photochemical production of ozone during summer. The averaged surface ozone changes over the continents (a factor of 2) imply a mean increase rate of about 1%/yr since the beginning of the industrial revolution. The oxidation capacity of the atmosphere, however, was less affected by industrialization. The photochemical lifetime of CH_4 and CO were about 10 and 5% lower than their present values. These small changes result from two compensating effects: the increase of OH (compared to present) in tropical regions, due to the lower CO and CH_4

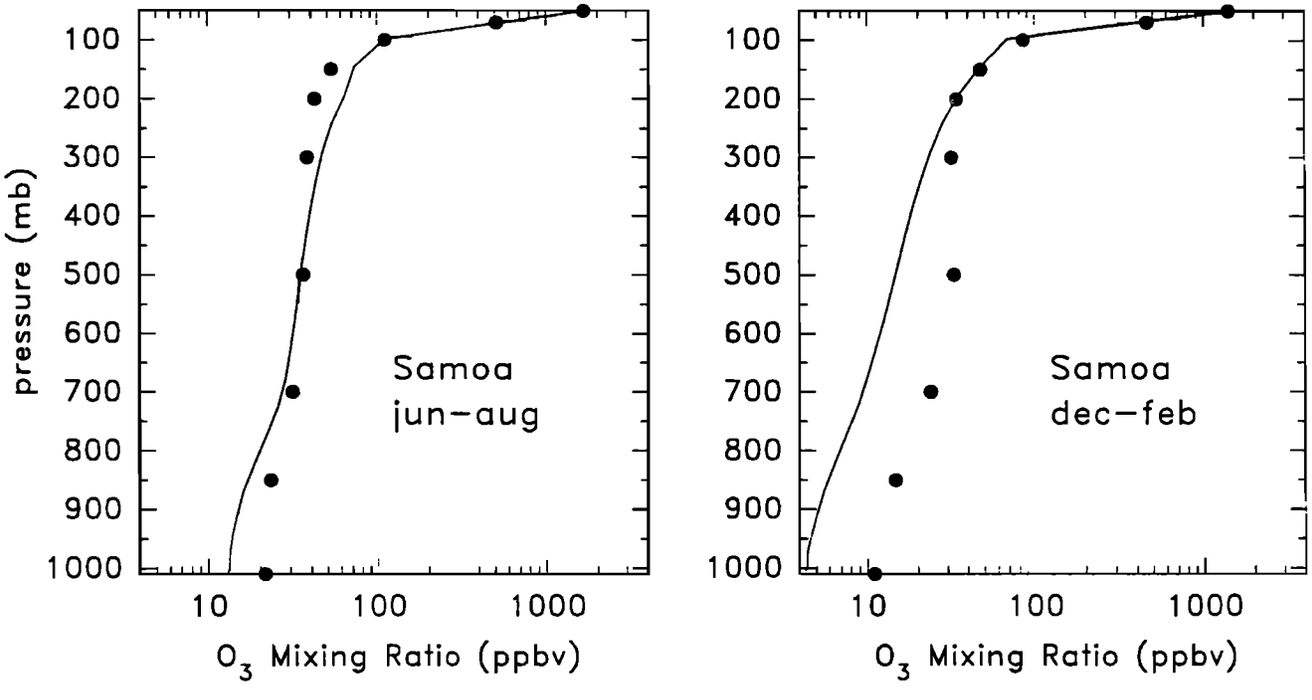

Figure 36. Observed and calculated vertical profiles of O_3 mixing ratio (ppbv) at Samoa Island for winter and summer. The data are from *Komhyr et al.* [1992].

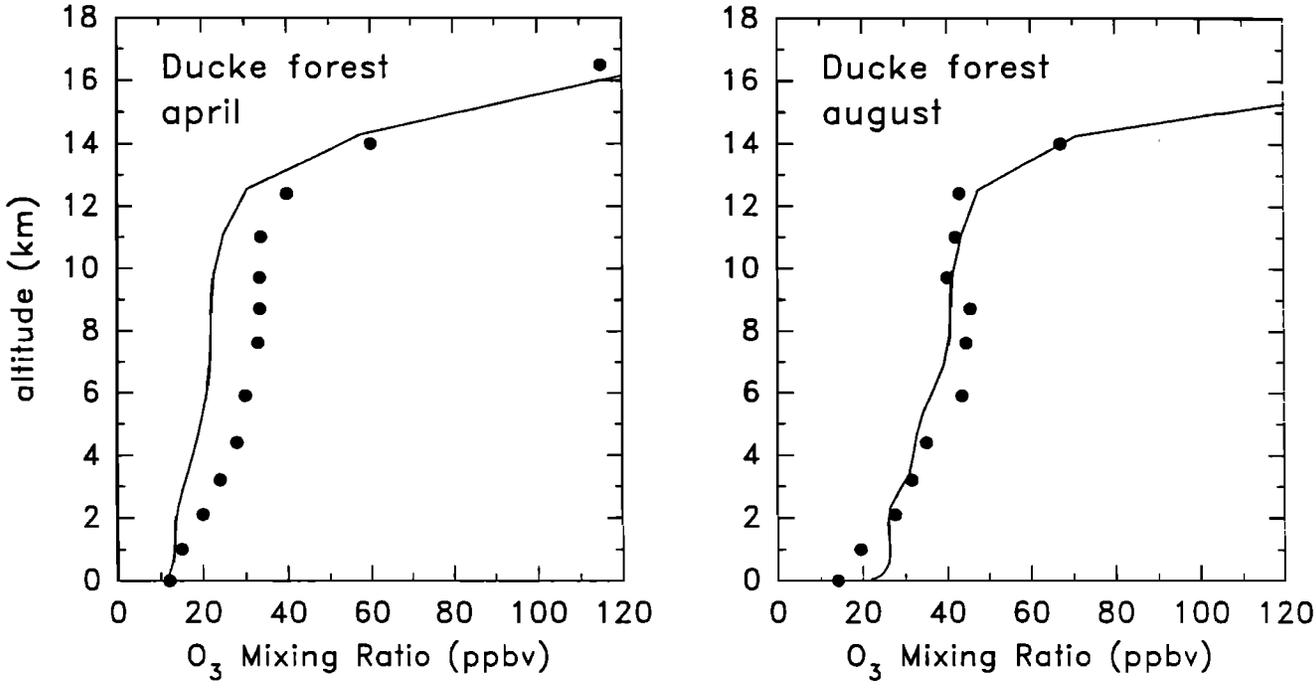

Figure 37. Observed and calculated vertical profiles of O_3 mixing ratio (ppbv) at Ducke forest (Amazonia, Brazil) in April (wet season) and August (dry season). The data are from *Kirchhoff et al.* [1990].

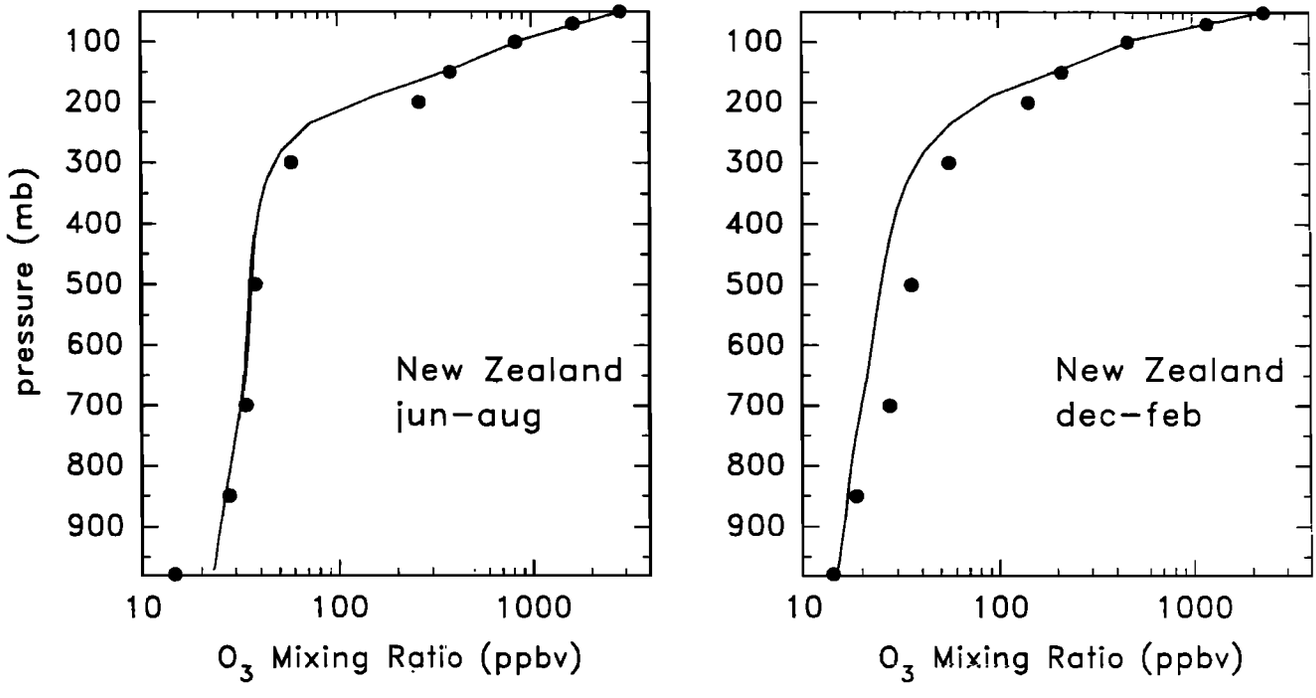

Figure 38. Observed and calculated vertical profiles of O_3 mixing ratio (ppbv) at Lauder (New Zealand) for winter and summer. The data are from *Komhyr et al.* [1992].

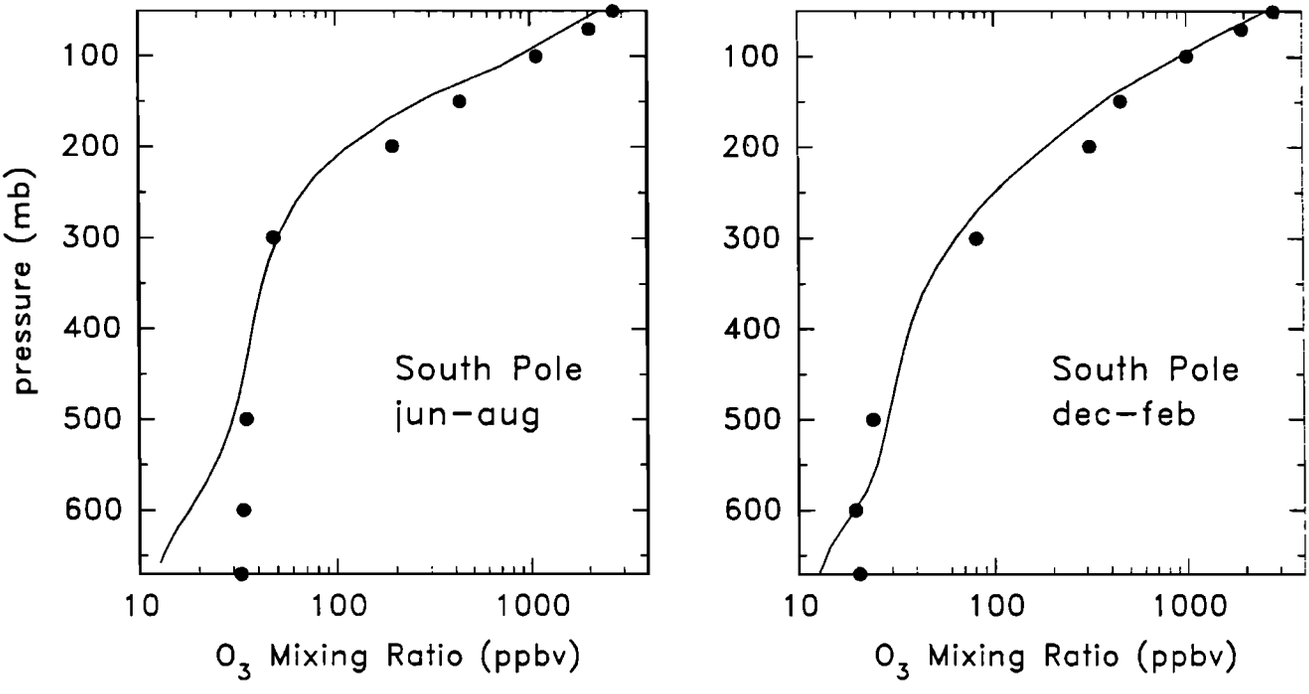

Figure 39. Observed and calculated vertical profiles of O_3 mixing ratio (ppbv) at south pole for winter and summer. The data are from *Komhyr et al.* [1992].

concentrations, and the decrease of OH at midlatitudes, where NO_x and O_3 changes were most pronounced. These results are consistent with other studies [e.g., *Pinto and Khalil*, 1991; *Hough and Derwent*, 1990; *Crutzen and Zimmermann*, 1991].

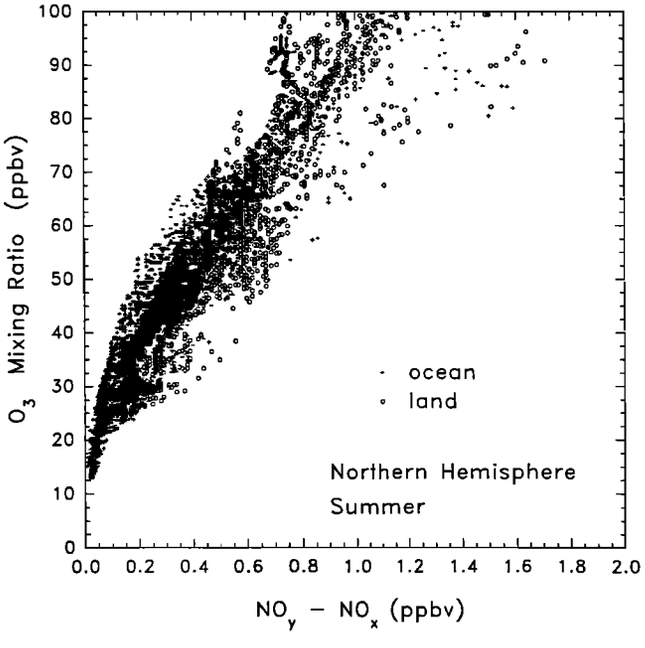

Figure 40. Mixing ratio of ozone (ppbv) calculated by the intermediate model of global evolution of species (IMAGES) and represented as a function of the difference between the NO_y and NO_x mixing ratios (ppbv). This scatter diagram includes the values derived in summer at all grid points located between 525 and 200 mbar in the northern hemisphere over the ocean and the continents.

4. Conclusions

We have presented a new three-dimensional chemical transport model which has been developed to study the global distributions and budget of trace constituents in the troposphere. From the transport point of view, the model is "intermediate" between highly parameterized approaches such as those used in one-dimensional models and fully explicit representations such as those provided by tracer models coupled to general circulation models (GCM). IMAGES provides a mathematical tool which requires a factor of 10 less computer resources than three-dimensional chemistry models coupled to GCMs because it has been designed to be integrated with long time steps, while accounting for the diurnal variation in solar insolation. Validation of the transport of long-lived species suggests that in spite of the simplifications introduced and the assumptions made, the overall representation of advective and convective exchanges

Table 10. Annual Budget of O_3 in the Model Domain, in Teragrams Per Year

Source/Sink Type	Magnitude
Sources	
photochemistry[a]	4550
from above domain	550
total	5100
Sinks	
photochemistry[a]	4000
dry deposition	1100
total	5100
Residence time[a], days	102

[a]Excluding null photochemical cycles, such as, e.g., the loss of ozone by O_3 + NO followed by photolysis of NO_2 and O_3 reformation.

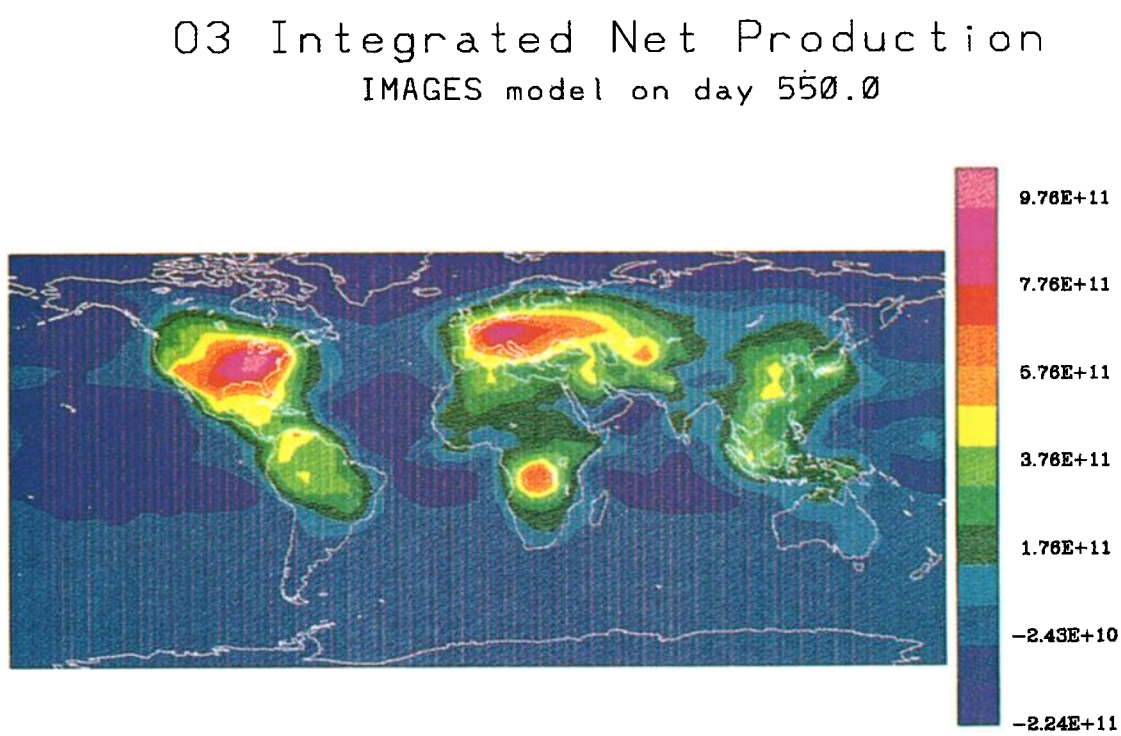

Figure 41. Vertically integrated net photochemical production of ozone calculated in July (cm^{-2} s^{-1}). Ozone is photochemically produced mostly over continental regions where combustion is intense and destroyed over the oceans.

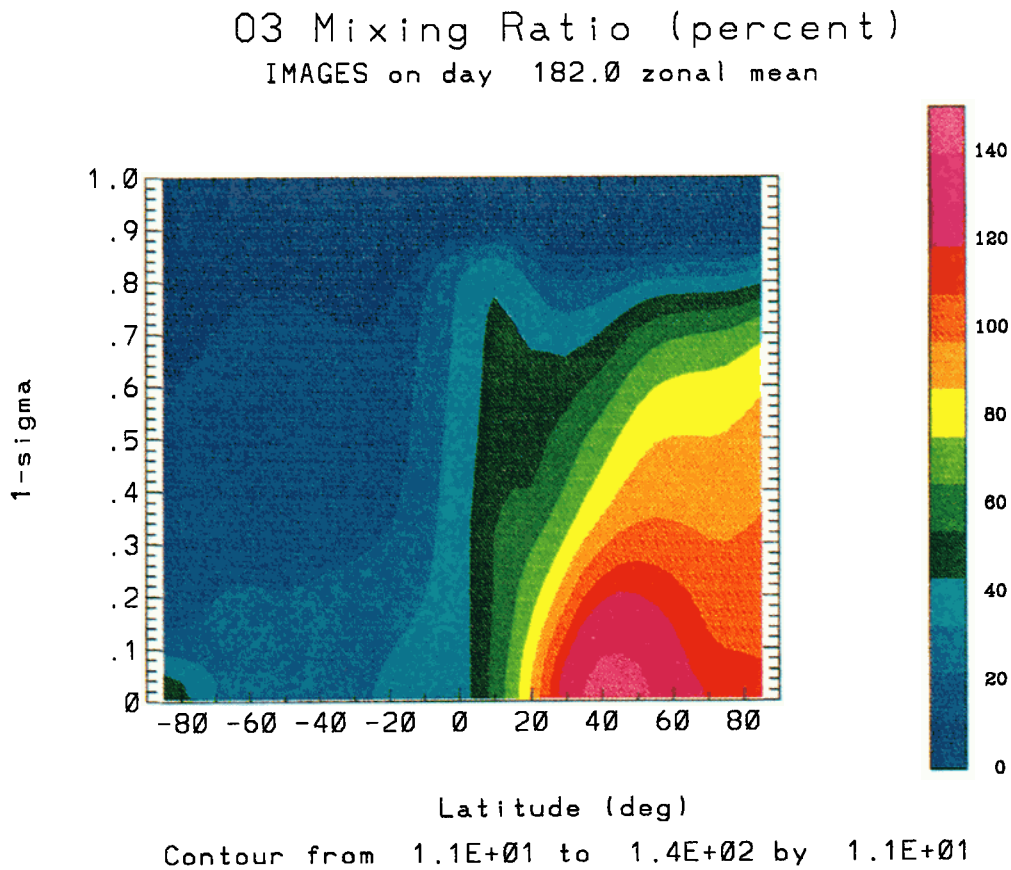

Figure 42. Percentage change between the calculated preindustrial and contemporary ozone mixing ratio (a) in June and (b) in December. The reference in these figures is the pre-industrial situation.

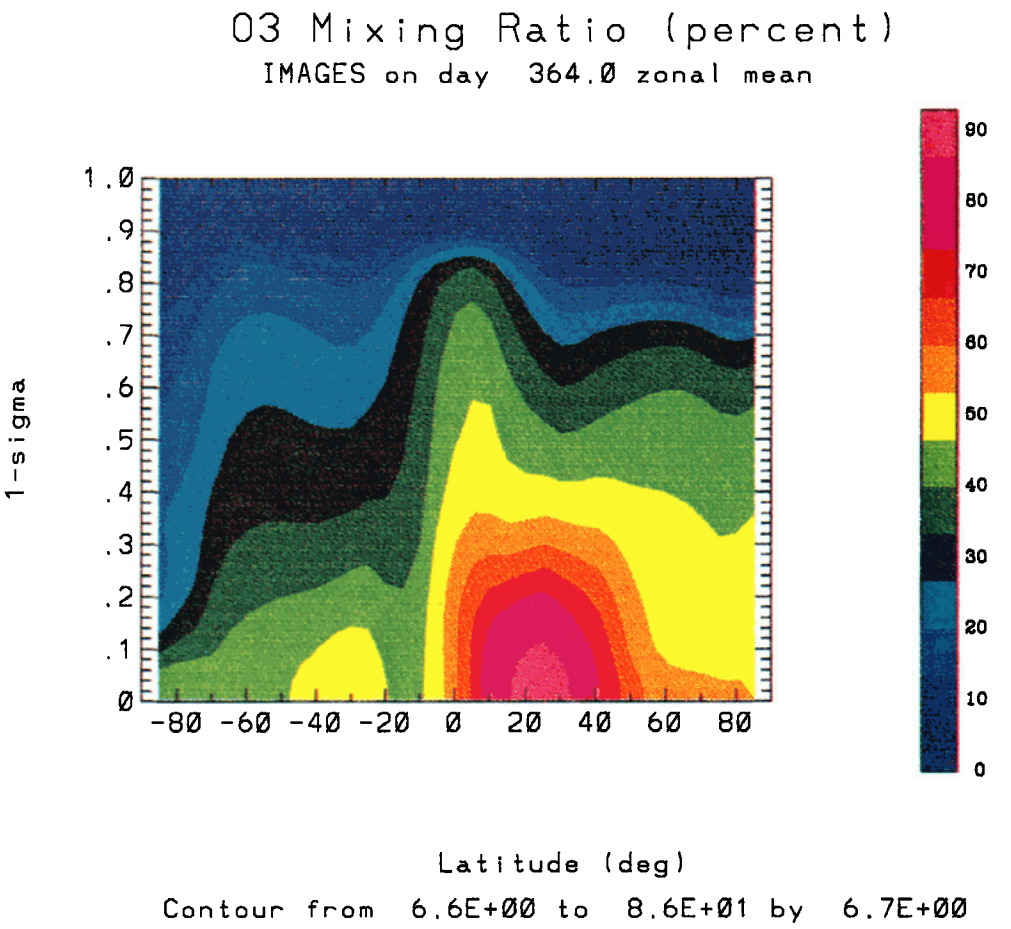

Figure 42. (continued)

represented by the model is satisfactory on the global scale. One of the advantages in the design of IMAGES is that with a relatively elaborated chemical scheme and a detailed representation of mass exchanges between the atmosphere and the surface (emissions, deposition), sensitivity studies can be performed without prohibitive computer costs. A simulation over 1 year requires approximately 7 hours of computer time on one processor on the NCAR Cray YMP-8. Although the model does not produce the high frequencies found in the observed time series of tracer concentrations, it provides climatological evolutions and spatial distributions which are generally in good agreement with available observations. Existing discrepancies will have to be addressed in subsequent studies which will focus on more specific aspects of tropospheric chemistry and transport. The model would benefit from a better representation of boundary layer exchanges and perhaps from a "plume model" to account for the nonlinear effects in chemistry associated with subgrid processes [*Sillman et al.*, 1990a, b]. In spite of these limitations of the model, IMAGES provides a framework constrained by climatological data (temperature, winds, cloudiness, precipitation, lightning frequency, surface sources), in which the three-dimensional distribution of 40 species can be simulated at relatively high spatial resolution, and the different components of the budget of these gases (emissions, chemical production and destruction, advective, convective and subscale transport, wet and dry deposition, exchanges with the stratosphere) can be quantified.

Acknowledgments. We wish to thank Sasha Madronich for making the NCAR Master Mechanism available to us, and Cheryl Craig, Claire Granier, Brian Ridley, and Stacy Walters for fruitful discussions and programming advice. One of us (JFM) was Research Assistant of the Belgian National Fund for Scientific Research (F.N.R.S.). This work was partly supported by the Belgian Service de la Programmation de la Politique Scientifique (S.P.P.S.), and by the Gas Research Institute. The National Center for Atmospheric Research is sponsored by the National Science Foundation.

References

Aselmann, I., and P. J. Crutzen, Global distribution of natural freshwater wetlands and rice paddies, their net primary productivity, seasonality and possible methane emissions, *J. Atmos. Chem.*, *8*, 307–358, 1989.

Atkinson, R., Kinetics and mechanisms of the gas-phase reactions of the hydroxyl radical with organic compounds under atmospheric conditions, *Chem. Rev.*, *85*, 69–201, 1985.

Atkinson, R., A. M. Winer, and J. N. Pitts Jr., Estimation of nighttime N_2O_5 concentrations from ambient NO_2 and NO_3 radical concentrations and the role of N_2O_5 in night-time chemistry, *Atmos. Environ.*, *20*, 331–339, 1986.

Atkinson, R., D. L. Baulch, R. A. Cox, R. F. Hampson Jr., J. A. Kerr, and J. Troe, Evaluated kinetic and photochemical data for atmospheric chemistry: Supplement III, *J. Phys. Chem. Ref. Data*, *18*, 881–1097, 1989.

Atlas, E. L., B. A. Ridley, G. Hubler, J. G. Walega, M. A. Caroll, D. D. Montzka, B. J. Huebert, R. B. Norton, F. E. Grahek, and S. Schauffer, Partitioning and budget of NO_y species during the Mauna Loa

Observatory Photochemistry Experiment, *J. Geophys. Res.*, *97*, 10,449–10,462,1992.

Baulch, D. L., R. A. Cox, R. F. Hampson Jr., J. A. Kerr, J. Troe, and R. T. Watson, Evaluated kinetic and photochemical data for atmospheric chemistry: Supplement II, *J. Phys. Chem. Ref. Data*, *13*, 1259–1380, 1984.

Blake, D. R., and F. S. Rowland, World-wide increase in tropospheric methane, 1978–1983, *J. Atmos. Chem.*, *4*, 43–62, 1986.

Bonsang, B., M. Kanakidou, G. Lambert, and P. Monfray, The marine source of C_2-C_5 aliphatic hydrocarbons, *J. Atmos. Chem.*, *6*, 3–20, 1988.

Bonsang, B., D. Martin, G. Lambert, M. Kanakidou, J. C. Le Roulley, and G. Sennequier, Vertical distribution of nonmethane hydrocarbons in the remote marine boundary layer, *J. Geophys. Res.*, *96*, 7313–7324, 1991.

Borucki, W. J., and W. L. Chameides, Lightning: Estimates of the rates of energy dissipation and nitrogen fixation, *Rev. Geophys.*, *22*, 363–372, 1984.

Brasseur, G. P., M. H. Hitchman, S. Walters, M. Dymek, E. Falise, and M. Pirre, An interactive chemical-dynamical radiative two-dimensional model of the middle atmosphere, *J. Geophys. Res.*, *95*, 5639–5655, 1990.

Brost, R. A., and R. B. Chatfield, Transport of radon in a three-dimensional, subhemispheric model, *J. Geophys. Res.*, *94*, 5095–5119, 1989.

Brost, R. A., J. Feichter, and M. Heimann, Three-dimensional simulation of ^{7}Be in a global climate model, *J. Geophys. Res.*, *96*, 22,423–22,445, 1991.

Calvert, J. G., and S. Madronich, Theoretical study of the initial products of the atmospheric oxidation of hydrocarbons, *J. Geophys. Res.*, *92*, 2211–2220, 1987.

Cantrell, C. A., W. R. Stockwell, L. G. Anderson, K. L. Busarow, D. Perner, A. Schmeltekopf, J. G. Calvert, and H. S. Johnston, Kinetic study of the NO_3-CH_2O reaction and its possible role in nighttime tropospheric chemistry, *J. Phys. Chem.*, *89*, 139–146, 1985.

Carmichael, G. R., L. K. Peters, and T. Kitada, A second-generation model for regional scale transport/chemistry/deposition, *Atmos. Environ.*, *20*, 173–188, 1986.

Carter, W. P. L., A detailed mechanism for the gas-phase atmospheric reactions of organic compounds, *Atmos. Environ.*, *24*, 481–518, 1990.

Carter, W. P. L., F. W. Lurmann, R. Atkinson, and A. C. Lloyd, Development and testing of a surrogate species chemical reaction mechanism, vol. I, *NTIS PB 86-212 404/AS*, Natl. Tech. Inf. Serv., Springfield, Va., 1986.

Chameides, W. L., The photochemistry of a remote marine stratiform cloud, *J. Geophys. Res.*, *89*, 4739–4755, 1984.

Chameides, W. L., and R. J. Cicerone, Effects of non-methane hydrocarbons in the atmosphere, *J. Geophys. Res.*, *83*, 947–952, 1978.

Chameides, W. L., D. H. Stedman, R. R. Dickerson, D. W. Rush, and R. J. Cicerone, NO_x production in lightning, *J. Atmos. Sci.*, *34*, 143–149, 1977.

Chang, J. S., R. A. Brost, I. S. A. Isaksen, S. Madronich, P. Middleton, W. R. Stockwell, and C. J. Walcek, A three-dimensional Eulerian acid deposition model: Physical concepts and formulation, *J. Geophys. Res.*, *92*, 14,681–14,700, 1987.

Charlson, R. J., D. S. Covert, T. V. Larson, and A. P. Waggoner, Chemical properties of tropospheric sulfur aerosols, *Atmos. Environ.*, *12*, 39–53, 1978.

Chatfield, R. B., and P. J. Crutzen, Sulfur dioxide in remote oceanic air: Cloud transport of reactive precursors, *J. Geophys. Res.*, *89*, 7111–7132, 1984.

Chatfield, R. B., and H. Harrison, Tropospheric ozone, 2, Variations along a meridional band, *J. Geophys. Res.*, *82*, 5969–5976, 1977.

Chin, M., D. J. Jacob, J. W. Munger, D. D. Parrish, B. G. Doddridge, Relationship of ozone and carbon monoxide over North America, *J. Geophys. Res.*, *99*, 14,565–14,573, 1994.

Cicerone, R. J., and R. S. Oremland, Biogeochemical aspects of atmospheric methane, *Global Biogeochem. Cycles*, *2*, 299–327, 1988.

Costen, R. C., G. M. Tennille, and J. S. Levine, Cloud pumping in a one-dimensional model, *J. Geophys. Res.*, *93*, 15,941–15,954, 1988.

Coulson, K. L., and D. W. Reynolds, The spectral reflectance of natural surfaces, *J. App. Meteorol.*, *10*, 1285–1295, 1971.

Crutzen, P. J., Methane's sinks and sources, *Nature*, *350*, 380–381, 1991.

Crutzen, P. J., and L. T. Gidel, A two-dimensional model of the atmosphere, 2, The tropospheric budgets of the anthropogenic chlorocarbons CO, CH_4, CH_3Cl, and the effects of various NO_x sources on tropospheric ozone, *J. Geophys. Res.*, *88*, 6641–6661, 1983.

Crutzen, P. J., and P. H. Zimmerman, The changing photochemistry of the troposphere, *Tellus*, *43*, 136–151, 1991.

Davis, D. D., J. D. Bradshaw, M. O. Rodgers, S. T. Sandholm, and S. KeSheng, Free tropospheric and boundary layer measurements of NO over the central and eastern North Pacific Ocean, *J. Geophys. Res.*, *92*, 2049–2070, 1987.

Demerjian, K. L., K. L. Schere, and J. T. Peterson, Theoretical estimates of actinic (spherically averaged) flux and photolytic rate constants of atmospheric species in the lower troposphere, *Adv. Environ. Sci. Technol.*, *10*, 369–459, 1980.

De More, W. B., S. P. Sander, R. F. Hampson, M. J. Kurylo, D. M. Golden, C. J. Howard, A. R. Ravishankara, C. E. Kolb, and M. J. Molina, Chemical kinetics and photochemical data for use in stratospheric modeling, in Evaluation 10, *JPL Publ. 92-20*, 1992.

Dentener, F. J., and P. J. Crutzen, Reaction of N_2O_5 on tropospheric aerosols: Impact on the global distributions of NO_x, O_3, and OH, *J. Geophys. Res.*, *98*, 7149–7163, 1993.

Dlugokencky, E. J., and C. J. Howard, Studies of NO_3 radical reactions with some atmospheric organic compounds at low pressure, *J. Phys. Chem.*, *93*, 1091–1096, 1989.

Donahue, N. M., and R. G. Prinn, Nonmethane hydrocarbon chemistry in the remote marine boundary layer, *J. Geophys. Res.*, *95*, 18,387–18,411, 1990.

Drummond, J. W., D. H. Ehhalt, and A. Volz, Measurements of nitric oxide between 67°N and 60°S latitude obtained during STRATOZ III, *J. Geophys. Res.*, *93*, 15,831–15,849, 1988.

Dvoryashina, E. V., V. I. Dianov-Klokov, and L. N. Yurganov, On the carbon monoxide atmospheric abundance variations for 1970–1982, *Izv. Russ. Acad. Sci. Atmos. Oceanic Phys., Engl. Transl.*, *20*, 40–47, 1984.

Ehhalt, D. H., and J. Rudolph, On the importance of light hydrocarbons in multiphase atmospheric systems, *Ber. Kernforschungsanlage Jülich, JÜL-1942*, pp. 1–43, 1984.

Ehhalt, D. H., F. Rohrer, and A. Wahner, Sources and distribution of NO_x in the upper troposphere at northern midlatitudes, *J. Geophys. Res.*, *97*, 3725–3738, 1992.

Erickson, D. J., Ocean to atmosphere carbon monoxide flux: Global inventory and climate implications, *Global Biogeochem. Cycles.*, *3*, 305–314, 1989.

Erickson, D. J., J. J. Walton, S. J. Ghan, and J. E. Penner, Three-dimensional modeling of the global atmospheric sulfur cycle: A first step, *Atmos. Environ.*, *25*(A), 2513–2520, 1991.

Feichter, J., and P. J. Crutzen, Parameterization of vertical tracer transport due to deep cumulus convection in a global transport model and its evaluation with ^{222}Radon measurements, *Tellus*, *42*(B), 100–117, 1990.

Feichter, J., R. A. Brost, and M. Heimann, Three-dimensional modeling of the concentration and deposition of ^{210}Pb aerosols, *J. Geophys. Res.*, *96*, 22,447–22,460, 1991.

Fishman, J., C. E. Watson, J. C. Larsen, and J. A. Logan, Distribution of tropospheric ozone from satellite data, *J. Geophys. Res.*, *95*, 3599–3617, 1990.

Food and Agriculture Organization (FAO), *Production Yearbook*, vol. 40, Rome, 1987.

Fung, I., K. Prentice, E. Matthews, J. Lerner, and G. Russel, Three-dimensional tracer model study of atmospheric CO_2: Response to seasonal exchanges with the terrestrial biosphere, *J. Geophys. Res.*, *88*, 1281–1294, 1983.

Fung, I., J. John, J. Lerner, E. Matthews, M. J. Prather, L. P. Steele, and P. J. Fraser, Global budgets of atmospheric methane: Results from a three-dimensional global model synthesis, *J. Geophys. Res.*, *96*, 13,033–13,065, 1991.

Galbally, I. E., The emissions of nitrogen to the remote atmosphere, in *Biogeochemical Cycling of Sulfur and Nitrogen in the Remote Atmosphere*, edited by J. N. Galloway et al., D. Reidel, Norwell, Mass., 1985.

Garcia, R. R., F. Stordal, S. Solomon, and J. F. Kiehl, A new numerical model of the middle atmosphere, 1, Dynamics and transport of tropospheric source gases, *J. Geophys. Res., 97*, 12,967–12,991, 1992.

Georgi, F., and W. L. Chameides, Rainout lifetimes of highly soluble aerosols and gases from simulations with a general circulation model, *J. Geophys. Res., 91*, 14,367–14,376, 1986.

Gery, M. W., G. Z. Whitten, J. P. Killus, and M. C. Dodge, A photochemical kinetics mechanism for urban and regional scale computer modeling, *J. Geophys. Res., 94*, 12,925–12,956, 1989.

Gidel, L. T., Cumulus cloud transport of transient tracers, *J. Geophys. Res., 88*, 6587–6599, 1983.

Gille, J. C., P. L. Bailey, and C. A. Craig, Proposed reference model for nitric acid, *Adv. Space Res., 7*, 925–935, 1987.

Giguere, P. A., and A. W. Olmos, Sur le spectre ultraviolet de l'acide peracétique et l'hydrolyse des peracétates, *Can. J. Chem., 34*, 689–691, 1956.

Greenberg, J. P., P. R. Zimmerman, L. Heidt, and W. Pollock, Hydrocarbon and carbon monoxide emissions from biomass burning in Brazil, *J. Geophys. Res., 89*, 1350–1354, 1984.

Hall, I. W., R. P. Wayne, R. A. Cox, M. E. Jenkin, and G. D. Hayman, Kinetics of the reaction of NO_3 with HO_2, *J. Phys. Chem., 92*, 5049–5054, 1988.

Hao, W. M., and D. E. Ward, Methane production from global biomass burning, *J. Geophys. Res., 98*, 20,657–20,661, 1993.

Hao, W. M., M. H. Liu, and P. J. Crutzen, Estimates of annual and regional releases of CO_2 and other trace gases to the atmosphere from fires in the tropics, based on the FAO statistics for the period 1975–1980, in *Fire in the Tropical Biota*, edited by J. G. Goldammer, pp. 440–462, Springer-Verlag, New York, 1990.

Hao, W. M., D. Scharffe, J. M. Lobert, and P. J. Crutzen, Emissions of nitrous oxide from the burning of biomass in an experimental system, *Geophys. Res. Lett., 18*, 999–1002, 1991.

Hatakeyama, S., K. Izumi, T. Fukuyama, and H. Akimoto, Reactions of ozone with α-pinene and β-pinene in air: Yields of gaseous and particulate products, *J. Geophys. Res., 94*, 13,013–13,024, 1989.

Hatakeyama, S., I. Katsuyuki, T. Fukuyama, H. Akimoto, and N. Washida, Reactions of OH with α-pinene and β-pinene in air: Estimate of global CO production from the atmospheric oxidation of terpenes, *J. Geophys. Res., 96*, 947–958, 1991.

Heikes, B. G., and A. M. Thompson, Effects of heterogeneous processes on NO_3, HONO, and HNO_3 chemistry in the troposphere, *J. Geophys. Res., 88*, 10,883–10,895, 1983.

Hesstvedt, E., Ø. Hov, and I. S. A. Isaksen, Quasi-steady state approximation in air pollution modeling: Comparison of two numerical schemes for oxidant prediction, *Int. J. Chem. Kinet., 10*, 971–944, 1978.

Hicks, B. B., and P. S. Liss, Transfer of SO_2 and other reactive gases across the sea-air interface, *Tellus, 28*, 348–354, 1976.

Hough, A. M., The development of a two-dimensional tropospheric model, 1, The model transport, *Atmos. Environ., 23*, 1235–1261, 1989.

Hough, A. M., Development of a two-dimensional global tropospheric model: Model chemistry, *J. Geophys. Res., 96*, 7325–7362, 1991.

Hough, A. M., and R. G. Derwent, Changes in the global concentration of tropospheric ozone due to human activities, *Nature, 344*, 645–648, 1990.

Hubler, G., D. W. Fahey, B. A. Ridley, G. L. Gregory, and F. C. Fehsenfeld, Airborne measurements of total reactive odd nitrogen (NO_y), *J. Geophys. Res., 97*, 9833–9850, 1992a.

Hubler, G., et al., Total reactive oxidized nitrogen (NO_y) in the remote Pacific troposphere and the correlation with O_3 and CO: Mauna Loa Observatory Photochemical Experiment 1988, *J. Geophys. Res., 97*, 10,427–10,447, 1992b.

Huebert, B. J., and A. L. Lazrus, Tropospheric gas-phase and particulate nitrate measurements, *J. Geophys. Res., 85*, 7322–7328, 1980.

Intergovernmental Panel for Climate Change (IPCC), *Climate change 1992*, edited by J. T. Houghton, B. A. Callender, and S. K. Varney, Cambridge University Press, New York, 1992.

Isaksen, I. S. A., and Ø. Hov, Calculations of trends in the tropospheric concentrations of O_3, OH, CO, CH_4, and NO_x, *Tellus, 39*(B), 271–285, 1987.

Isaksen, I. S. A., Ø. Hov, S. A. Penkett, and A. Semb, Model analysis of the measured concentrations of organic gases in the Norwegian Arctic, *J. Atmos. Chem., 3*, 3–27, 1985.

Jacob, D. J., The chemistry of OH in remote clouds and its role in the production of formic acid and peroxymonosulfate, *J. Geophys. Res., 91*, 9807–9826, 1986.

Jacob, D. J., and M. J. Prather, Radon-222 as a test of convective transport in a general circulation model, *Tellus, 42*(B), 118–134, 1990.

Jacob, D. J., and S. C. Wofsy, Photochemistry of biogenic emissions over the Amazon forest, *J. Geophys. Res., 93*, 1477–1486, 1988.

Jacob, D. J., and S. C. Wofsy, Budgets of reactive nitrogen, hydrocarbons, and ozone over the Amazon forest during the wet season, *J. Geophys. Res., 95*, 16,737–16,754, 1990.

Jacob, D. J., M. J. Prather, S. C. Wofsy, and M. B. Mc Elroy, Atmospheric distribution of ^{85}Kr simulated with a general circulation model, *J. Geophys. Res., 92*, 6614–6626, 1987.

Johnson, J. E., R. H. Gammon, J. Larsen, T. S. Bates, S. J. Oltmans, and J. C. Farmer, Ozone in the marine boundary layer over the Pacific and Indian Oceans: Latitudinal gradients and diurnal cycles, *J. Geophys. Res., 95*, 11,847–11,856, 1990.

Johnston, H. S., C. A. Cantrell, and J. G. Calvert, Unimolecular decomposition of NO_3 to form NO and O_2 and a review of N_2O_5/NO_3 kinetics, *J. Geophys. Res., 91*, 5159–5172, 1986.

Joseph, J. H., W. J. Wiscombe, and J. A. Weiman, The delta-Eddington approximation for radiative flux transfer, *J. Atmos. Sci., 33*, 2452–2458, 1976.

Kasting, J. F., and H. B. Singh, Nonmethane hydrocarbons in the troposphere: Impact on odd hydrogen and odd nitrogen chemistry, *J. Geophys. Res., 91*, 13,239–13,256, 1986.

Khalil, M. A. K., and R. A. Rasmussen, Climate-induced feedbacks for the global cycles of methane and nitrous oxide, *Tellus, 41*(B), 554–559, 1989.

Khalil, M. A. K., R. A. Rasmussen, J. R. J. French, and J. A. Holt, The influence of termites on atmospheric trace gases: CH_4, CO_2, $CHCl_3$, CO, H_2, and light hydrocarbons, *J. Geophys. Res., 95*, 3619–3634, 1990.

Kirchhoff, V. W. J. H., I. M. O. da Silva, and E. V. Browell, Ozone measurements in Amazonia: Dry season versus wet season, *J. Geophys. Res., 95*, 16,913–16,926, 1990.

Kirchhoff, V. W. J. H., A. W. Setzer, and M. C. Pereira, Biomass burning in Amazonia: Seasonal effects on atmospheric O_3 and CO, *Geophys. Res. Lett., 16*, 469–472, 1989.

Ko, K. W., H. R. Schneider, R.-L. Shia, D. K. Weisenstein, and N.-D. Sze, A two-dimensional model with coupled dynamics, radiation, and photochemistry, 1, Simulation of the middle atmosphere, *J. Geophys. Res., 98*, 20,429–20,440, 1993.

Komhyr, W. D., S. J. Oltmans, J. A. Lathrop, J. B. Kerr, and W. A. Matthews, The latitudinal distribution of ozone to 35 km altitude from ECC ozonesonde observations, 1982–1990, paper presented at the *Quadreinnal Ozone Symposium, Int. Assoc. of Meteorol. and Atmos. Phys.*, Charlottesville, Va., 1992.

Kondo, Y. P., P. Aimedieu, W. A. Matthews, W. R. Sheldon, and J. R. Benbrook, A midlatitude balloonborne observation of total odd nitrogen, *Geophys. Res. Lett., 17*, 73–76, 1990.

Kondratyev, K. Y., *Radiation in the Atmosphere*, Academic, San Diego, Calif., 1969.

Kondratyev, K. Y., et al., The shortwave albedo and the surface emissivity, in *Land Surface Processes in Atmospheric Circulation Models*, edited by P. Eagleson, pp. 463–514, 1982.

Kurzeja, R. J., The diurnal variation of minor constituents in the stratosphere and its effect on the ozone concentrations, *J. Atmos. Sci., 32*, 899, 1975.

Langner, J., and H. Rodhe, A global three-dimensional model of the tropospheric sulfur cycle, *J. Atmos. Chem., 13*, 225–263, 1991.

Law, K. S., and J. A. Pyle, Modeling trace gases in the troposphere, 1, Ozone and odd nitrogen, *J. Geophys. Res., 98*, 18,377–18,400, 1993a.

Law, K. S., and J. A. Pyle, Modeling trace gases in the troposphere, 2, CH_4 and CO, *J. Geophys. Res., 98*, 18,401–18,412, 1993b.

Levy, H., II, and W. J. Moxim, Simulated global distribution and deposition of reactive nitrogen emitted by fossil fuel combustion, *Tellus, 41*(B), 256–271, 1989a.

Levy, H., II, and W. J. Moxim, Influence of long-range transport of combustion emissions on the chemical variability of the background atmosphere, *Nature, 338*, 326–328, 1989b.

Levy, H., II, J. D. Mahlman, and W. J. Moxim, Tropospheric N_2O variability, *J. Geophys. Res., 87*, 3061–3080, 1982.

Levy, H., II, J. D. Mahlman, W. J. Moxim, and S. C. Liu, Tropospheric ozone: The role of transport, *J. Geophys. Res., 90*, 3753–3772, 1985.

Liaw, Y. P., D. L. Sisterson, and N. L. Miller, Comparison of field, laboratory, and theoretical estimates of global nitrogen fixation by lightning, *J. Geophys. Res., 95*, 22,489–22,494, 1990.

Lieth, H., Modeling the primary productivity of the world, in *Primary Productivity of the Biosphere*, edited by H. Lieth, and R. H. Whittaker, pp. 237–263, Springer-Verlag, New York, 1975.

Lin, W., M. Trainer, and S. C. Liu, On the nonlinearity of the tropospheric ozone production, *J. Geophys. Res.*, 93, 15,879–15,888, 1988.

Liu, S. C., and M. Trainer, Responses of the tropospheric ozone and odd hydrogen radicals to column ozone change, *J. Atmos. Chem., 6*, 221–233, 1988.

Liu, S. C., J. R. McAffee, and R. J. Cicerone, Radon 222 and tropospheric vertical transport, *J. Geophys. Res., 89*, 7291–7297, 1984.

Liu, S. C., et al., A study of the photochemistry and ozone budget during the Mauna Loa Observatory Photochemistry Experiment, *J. Geophys. Res., 97*, 10,463–10,471, 1992.

Logan, J. A., Nitrogen oxides in the troposphere: Global and regional budgets, *J. Geophys. Res., 88*, 10,785–10,807, 1983.

Logan, J. A., and V. W. J. H. Kirchhoff, Seasonal variations of tropospheric ozone at Natal, *J. Geophys. Res., 91*, 7875–7881, 1986.

Logan, J. A., M. J. Prather, S. C. Wofsy, and M. B. McElroy, Tropospheric chemistry: A global perspective, *J. Geophys. Res., 86*, 7210–7254, 1981.

Louis, J.-F., A two-dimensional model of the atmosphere, Ph.D. thesis, 150 pp., Univ. of Colo., Boulder, 1974.

Low, P. S., T. D. Davies, P.M. Kelley, and G. Farmer, Trends in surface ozone at Hohenpeissenberg and Arkona, *J. Geophys. Res., 95*, 22,441–22,453, 1990.

Luecken, D. J., C. M. Berkowitz, and R. C. Easter, Use of a three-dimensional cloud-chemistry model to study the transatlantic transport of soluble sulfur species, *J. Geophys. Res., 96*, 22,477–22,490, 1991.

Lurmann, F. W., A. C. Lloyd, and R. Atkinson, A chemical mechanism for use in long-range transport/acid deposition computer modeling, *J. Geophys. Res., 91*, 10,905–10,936, 1986.

Madronich, S., Photodissociation in the atmosphere, 1, Actinic flux and the effects of ground reflections and clouds, *J. Geophys. Res., 92*, 9740–9752, 1987.

Madronich, S., and J. G. Calvert, The NCAR Master Mechanism of the gas phase chemistry—Version 2.0, *NCAR Tech. Note, NCAR/TN-333+STR*, 1989.

Madronich, S., and J. G. Calvert, Permutation reactions of organic peroxy radicals in the troposphere, *J. Geophys. Res., 95*, 5697–5715, 1990.

Mahlman, J. D., and W. J. Moxim, Tracer simulation using a global general circulation model: Results from a midlatitude instantaneous source experiment, *J. Atmos. Sci., 35*, 1340–1374, 1978.

Marenco, A., M. Macaigne, and S. Prieur, Meridional and vertical CO and CH_4 distributions in the background troposphere (70°N–60°S; 0–12 km altitude) from scientific aircraft measurements during the STRATOZ III experiment (June 1984), *Atmos. Environ., 23*, 185–200, 1989.

McKeen, S. A., E.-Y. Hsie, and S. C. Liu, A study of the dependence of rural ozone on ozone precursors in the eastern United States, *J. Geophys. Res., 96*, 15,377–15,394, 1991a.

McKeen, S. A., E.-Y. Hsie, M. Trainer, R. Tallamraju, and S. C. Liu, A regional model study of the ozone budget in the eastern United States, *J. Geophys. Res., 96*, 10,809–10,845, 1991b.

McPeters, D. F. Heath, and P. K. Bhartia, Average ozone profiles for 1979 from the Nimbus 7 SBUV instrument, *J. Geophys. Res., 89*, 5199–5214, 1984.

Middleton, P., W. R. Stockwell, and W. P. Carter, Aggregation and analysis of volatile organic compound emissions for regional modeling, *Atmos. Environ., 24*, 1107–1133, 1990.

Moortgat, G. K., B. Veyret, and R. Lesclaux, Absorption spectrum and kinetics of reactions of the acetylperoxy radical, *J. Phys. Chem., 93*, 2362–2368, 1989a.

Moortgat, G. K., B. Veyret, and R. Lesclaux, Kinetics of the reaction of HO_2 with $CH_3C(O)O_2$ in the temperature range 253–368 K, *Chem. Phys. Lett., 160*, 443–447, 1989b.

Mozurkewich, M., and J. G. Calvert, Reaction probability of N_2O_5 on aqueous aerosols, *J. Geophys. Res., 93*, 15,889–15,896, 1988.

Müller, J.-F., Geographical distribution and seasonal variation of surface emissions and deposition velocities of atmospheric trace gases, *J. Geophys. Res., 97*, 3787–3804, 1992.

Müller, J.-F., Modélisation tri-dimensionnelle globale de la chimie et du transport des gaz en trace dans la troposphère, Ph.D. thesis, Belgian Inst. for Space Aeron., Brussels, 1993.

Murgatroyd, R. J., Estimation from geostrophic trajectories of horizontal diffusivity in the mid-latitude troposphere and lower stratosphere, *Q. J. R. Meteorol. Soc., 95*, 40–62, 1969.

Neue Welt Atlas, Kartographisches Institut Bertelsmann, Reises und Verkehrsverlag GmbH Berlin-Götersloh-Stuttgart, Germany, 1977.

Nicolet, M., R. R. Meier, and D. E. Anderson Jr., Radiation field in the troposphere and stratosphere, II, Numerical analysis, *Planet. Space Sci., 30*, 935–983, 1982.

Novelli, P. C., P. Steele, and P. P. Tans, Mixing ratios of carbon monoxide in the tropsphere, *J. Geophys. Res., 97*, 20,731–20,750, 1992.

Olson, J. S., J. A. Watts, and L. J. Allison, Carbon in live vegetation of major world ecosystems, *DOE/NBB Rep. TR004*, Dep. of Energy, Oak Ridge Natl. Lab., Oak Ridge, Tenn., 1983.

Olson, J. S., J. A. Watts, and L. J. Allison, Major world ecosystem complexes ranked by carbon in live vegetation, A data base, *ORNL-5862*, 164 pp., Oak Ridge National Laboratory, Oak Ridge, Tenn., 1985.

Oltmans, S. J., and W. D. Komhyr, Surface ozone distributions and variations from 1973 to 1984 measurements at the NOAA geophysical monitoring for climatic change baseline observatories, *J. Geophys. Res., 91*, 5229–5236, 1986.

Oltmans, S. J., and H. Levy II, Seasonal cycle of surface ozone over the western North Atlantic, *Nature, 358*, 392–394, 1992.

Organization for Economic Cooperation and Development (OECD), in *Environmental Data, Compendium 1989*, Paris, 1989.

Parrish, D. D., R. B. Norton, M. J. Bollinger, S. C. Liu, P. C. Murphy, D. L. Albritton, and F. C. Fehsenfeld, Measurements of HNO_3 and NO_3^- particulates at a rural site in the Colorado mountains, *J. Geophys. Res., 91*, 5379–5393, 1986.

Pasquill, F., Limitations and prospects in the estimation of dispersion of pollution on a regional scale, *Adv. Geophys., 18*(B), 1–13, 1974.

Paulson, S. E., and J. H. Seinfeld, Development and evaluation of a photooxidation mechanism for isoprene, *J. Geophys. Res., 97*, 20,703–20,715, 1992.

Penner, J. E., C. S. Atherton, J. Dignon, S. J. Ghan, J. J. Walton, and S. Hameed, Tropospheric nitrogen: A three-dimensional study of sources, distribution, and deposition, *J. Geophys. Res., 96*, 959–990, 1991.

Pham, M., Modélisation du cycle des composés soufrés atmosphériques,

Processus physico-chimiques et bilans à l'échelle globale, Ph. D. thesis, Univ. Paris VI, Paris, 1993.

Phillips, N. A., A coordinate system having some special advantages for numerical forecasting, *J. Meteorol., 14*, 184–185, 1957.

Pinto, J. P., and M. A. K. Khalil, The stability of tropospheric OH during ice ages, inter-glacial epochs and modern times, *Tellus, 43*(B), 347–352, 1991.

Platt, U. F., A. M. Winer, H. W. Biermann, R. Atkinson, and J. N. Pitts Jr., Measurements of nitrate radical concentrations in continental air, *Environ. Sci. Technol., 18*, 365–369, 1984.

Plum, C. N., E. Sanhueza, R. Atkinson, W. P. L Carter, and J. N. Pitts Jr., OH radical rate constants and photolysis rates of α-dicarbonyls, *Environ. Sci. Technol., 17*, 479–484, 1983.

Prather, M. J., M. B. McElroy, S. C. Wofsy, G. Russel, and D. Rind, Chemistry of the global troposphere: Fluorocarbons as tracers of air motion, *J. Geophys. Res., 92*, 6579–6613, 1987.

Prinn, R., et al., Global average concentration and trend for hydroxyl radicals deduced from ALE/GAGE trichloroethane (methylchloroform) data for 1978–1990, *J. Geophys. Res., 97*, 2445–2461, 1992.

Proffitt, M. H., et al., High latitude ozone loss outside the Antarctic ozone hole, *Nature, 342*, 233–237, 1989.

Reichle, H. G., V. S. Connors, J. A. Holland, R. T. Sherrill, H. A. Wallio, J. C. Casas, E. P. Condon, B. B. Gormsen, and W. Seiler, The distribution of middle troposheric carbon monoxide during early October 1984, *J. Geophys. Res., 95*, 9845–9856, 1990.

Ritchie, H., Eliminating the interpolation associated with the semi-Lagrangian scheme, *Mon. Weather Rev., 114*, 135–146, 1986.

Roberts, J. M., The atmospheric chemistry of organic nitrates, *Atmos. Environ., 24*, 243–287, 1990.

Rossow, W. B., and R. A. Schiffer, ISCCP cloud data products, *Bull. Am. Meteorol. Soc., 72*, 2–20, 1991.

Rossow, W. B., L. C. Garder, P. J. Lu, and A. W. Walker, International Satellite Cloud Climatology Project (ISCCP), Documentation on cloud data, *WMO/TD-266*, 78 pp., World Meteorol. Organization, Geneva, 1987.

Rudolph, J., and D. H. Ehhalt, Measurements of C_2-C_5 hydrocarbons over the North Atlantic, *J. Geophys. Res., 86*, 11,959–11,964, 1981.

Sander, S. P., M. Peterson, R. T. Watson, and R. Patrick, Kinetic studies of the HO_2 + HO_2 and DO_2 + DO_2 reactions at 298 K, *J. Phys. Chem., 86*, 1236–1240, 1982.

Seiler, W., H. Giehl, E. G. Brunke, and E. Halliday, The seasonality of CO abundance in the Southern Hemisphere, *Tellus, 36*(B), 219–231, 1984.

Shea, D. J., Climatological atlas: 1950–1979, *NCAR Tech. Note, NCAR/TN-269+STR*, 1986.

Sillman, S., J. A. Logan, and S. C. Wofsy, A regional scale model for ozone in the United States with subgrid representation of urban and power plant plumes, *J. Geophys. Res., 95*, 5731–5748, 1990a.

Sillman, S., J. A. Logan, and S. C. Wofsy, The sensitivity of ozone to nitrogen oxides and hydrocarbons in regional ozone episodes, *J. Geophys. Res., 95*, 1837–1851, 1990b.

Singh, H. B., L. J. Salas, and W. Viezee, Global distribution of peroxyacetyl nitrate, *Nature, 321*, 588–591, 1986.

Singh, H. B., W. Viezee, and L. J. Salas, Measurements of selected C_2-C_5 hydrocarbons in the tropopshere: Latitudinal, vertical and temporal variations, *J. Geophys. Res., 93*, 15,861–15,878, 1988.

Smolarkiewicz, P. K., and G. A. Grell, A class of monotone interpolation schemes, *J. Comput. Phys., 101*, 431–440, 1991.

Smolarkiewicz, P. K., and P. J. Rash, Monotone advection on the sphere: An Eulerian versus semi-Lagrangian approach, *J. Atmos. Sci., 48*, 793–810, 1991.

Spivakovsky, C. M., R. Yevich, J. A. Logan, S. C. Wofsy, M. B. McElroy, and M. J. Prather, Tropospheric OH in a three-dimensional chemical tracer model: An assessment based on observations of CH_3CCl_3, *J. Geophys. Res., 95*, 18,441–18,471, 1990.

Stauffer, B., G. Fisher, A. Neftel, and H. Oeschger, Increase of atmospheric methane recorded in Antarctic ice cores, *Science, 229*, 1386–1388, 1985.

Steele, L. P., P. J. Frazer, R. A. Rasmussen, M. A. K. Khalil, T. J. Conway, A. J. Crawford, R. H. Gammon, K. A. Masarie, and K. W. Thoning, The global distribution of methane in the troposphere, *J. Atmos. Chem., 5*, 125–171, 1987.

Stockwell, W. R., A homogeneous gas phase mechanism for use in a regional acid deposition model, *Atmos. Environ., 20*, 1615–1632, 1986.

Tans, P. P., I. Y. Fung, T. Takahashi, Observational constraints on the global atmospheric CO_2 budget, *Science, 247*, 1431–1438, 1990.

Taylor, J. A., G. P. Brasseur, P. R. Zimmerman, and R. J. Cicerone, A study of the sources and sinks of methane and methyl chloroform using a global three-dimensionalimensional Lagrangian tropospheric tracer transport model, *J. Geophys. Res., 96*, 3013–3044, 1991.

Thompson, A. M., and R. J. Cicerone, Clouds and wet removal as causes of variability in the trace-gas composition of the marine troposphere, *J. Geophys. Res., 89*, 8811–8826, 1982.

Torres, A. L., and H. Buchan, Tropospheric nitric oxide measurements over the Amazon Basin, *J. Geophys. Res., 93*, 1396–1406, 1988.

Trainer, M., et al., Correlation of ozone with NO_y in photochemically aged air, *J. Geophys. Res., 98*, 2917–2925, 1993.

Tremback, C. J., J. Powell, W. R. Cotton, and R. A. Pielke, The forward-in-time upstream advection scheme: Extension to higher orders, *Mon. Weather Rev., 115*, 540–555, 1987.

Trenberth, K. E., and J. G. Olson, Intercomparison of NMC and ECMWF global analyses, *NCAR Tech. Note, NCAR/TN-229+STR*, 1988a.

Trenberth, K. E., and J. G. Olson, ECMWF Global Analyses 1979–1986: Circulation statistics and data evaluation, *NCAR Tech. Note, NCAR/TN-300+STR*, 1988b.

Turco, R. P., and R. C. Whitten, A note on the averaging of aeronomical models, *J. Atmos. Terr. Phys., 40*, 13–20, 1978.

Turman, B. N., and B. C. Edgar, Global lightning distributions at dawn and dusk, *J. Geophys. Res., 87*, 1191–1206, 1982.

United Nations (UN), *Energy Statistics Yearbook*, New York, 1986.

United Nations (UN), *Industrial Statistics Yearbook*, vol. I and II, New York, 1988.

Volz, A., and D. Kley, Evaluation of the Montsouris series of ozone measurements made in the nineteenth century, *Nature, 332*, 240–242, 1988.

Warneck, P., *Chemistry of the Natural Atmosphere*, Int. Geophys. Ser., vol. 41, pp. 37–45, Academic, San Diego, Calif., 1987.

Warren, S. G., C. J. Hahn, J. London, R. M. Chervin, and R. L. Jenne, Global distributions of total cloud cover and cloud type amounts over land, *NCAR Tech. Note, NCAR/TN-273+STR*, 1986.

Warren, S. G., C. J. Hahn, J. London, R. M. Chervin, and R. L. Jenne, Global distributions of total cloud cover and cloud type amounts over the ocean, *NCAR Tech. Note, NCAR/TN+STR*, 1987.

Weinheimer, A. J., J. G. Walega, B. R. Ridley, G. W. Sachse, B. E. Anderson, and J. E. Collins Jr., Stratospheric NO_y measurements on the NASA DC-8 during AASE II, *Geophys. Res. Lett., 20*, 2563-2566, 1993.

Weiss, W., A. Sittkus, H. Stockburger, and H. Sartorius, Large-scale atmospheric mixing derived from meridional profiles of krypton 85, *J. Geophys. Res., 88*, 8574–8578, 1983.

Winkler, P., Surface ozone over the Atlantic Ocean, *J. Atmos. Chem., 7*, 73–91, 1988.

World Meteorological Organization (WMO), Atmospheric ozone 1985-Assessment of our understanding of the processes controlling its distribution and change, *WMO Rep. 16*, Global Ozone Res. Monit. Proj., Geneva, 1986.

Zalesak, S. T., Fully multidimensional flux-corrected transport algorithms for fluids, *J. Comput. Phys., 31*, 335-362, 1979.

Zhang, S.-H., M. Shaw, J. H. Seinfeld, and R. C. Flagan, Photochemical aerosol formation from α- and β-pinene, *J. Geophys. Res., 97*, 20,717–20,729, 1992.

Zimmermann, P. H., MOGUNTIA: A handy global tracer model, in *Proceedings of the Sixteenth NATO/CCMS International Technical Meeting on Air Pollution Modeling and Its Application,* edited by H. van Dop, pp. 593–608, Plenum, New York, 1988.

Zimmermann, P. H., J. Feichter, H. K. Rath, P. J. Crutzen, and W. Weiss, A global three-dimensional source-receptor model investigation using ^{85}Kr, *Atmos. Environ., 23*, 25–35, 1989.

G. Brasseur, Atmospheric Chemistry Division, NCAR, P. O. Box 3000, Boulder, CO 80307.

J.-F. Müller, Belgian Institute for Space Aeronomy, 3 avenue Circulaire, 1180 Brussels, Belgium.

(Received April 13, 1994; revised November 11, 1994; accepted November 13, 1994.)